NORTHWESTERN UNIVERSITY

Strategies to Control the Redox Activity of Quantum Dots through their Surface Chemistry

A DISSERTATION

SUBMITTED TO THE GRADUATE SCHOOL

IN PARTIAL FULFILLMENT OF THE REQUIREMENTS

for the degree

DOCTOR OF PHILOSOPHY

Field of Chemistry

By

Kaitlyn Ann Perez

EVANSTON, ILLINOIS

June 2020

Abstract

Strategies to Control the Redox Activity of Quantum Dots through their Surface Chemistry

Kaitlyn Ann Perez

This dissertation describes the study of photoinduced charge transfer between QDs and molecular acceptors as a probe of the defects within ligand shells of QDs and as means to photocatalyze redox reactions. For charge transfer reactions to occur between QDs and molecules in bulk solution, the molecules must interact with the inorganic core of QDs, either by transiently colliding with or being chemically associated with the surface. Thus, this surface of QDs, which includes their ligand layer, acts an interface between the inorganic core of QDs and bulk solution. Defects within their ligand shell enable freely diffusing molecular photooxidants to corrode QDs. This research explores the mechanisms by which a series of alkythiolate ligands with varying degrees of fluorination imparts protection upon three sizes of PbS QDs from oxidation by duroquinone. The most-highly fluorinated alkythiolate ligands are most effective at passivating the surfaces of PbS QDs due to the steric bulk of their fluorinated segments; these ligands are more protective for the largest QDs than the smaller sizes because the defects present in the ligand shells of QDs are size-dependent. While the ligand shell of QDs can be instrumental in inhibiting detrimental interactions, their surface chemistry can also be exploited to enhance desirable reactivity. This research explores the kinetics and scope of the reductive photodeprotection of sulfonyl protected phenols by copper indium sulfide QDs. The rate of deprotection for a substrate that contains a known QD-binding group is significantly enhanced due to the formation of a donor-

acceptor complex. The research described in this dissertation furthers the understanding of the relationship between the surface chemistry of QDs and their reactivity.

Acknowledgments

A PhD is not a solo endeavor, and I am extremely grateful for the support and guidance I have received from my mentors, colleagues, friends, and family during my PhD.

First, I would like to thank my advisor, Professor Emily Weiss, who has dedicated much time and effort to my growth as a scientist. Through our many meetings and interactions over the past five years, I have learned how to ask more interesting questions, approach and overcome research obstacles, and more effectively communicate as a writer and presenter. I never once doubted Emily's investment in my work, and for that, I am especially grateful.

As a young graduate student, I was very fortunate to have the support of many mentors in the Weiss lab that selflessly shared their time and knowledge with me, in particular Dr. David Weinberg, Dr. Kedy Edme, Dr. Mohamad Kodaimati, and Dr. Shichen Lian. My research has been enriched by discussions with many members of the Weiss labs that brought a fresh perspective and new ideas to my work. I am also very lucky to have had the camaraderie and support of my labmates, especially my cohort: Dr. Kevin McClelland, Jack Olding, James Schwabacher, Dr. Dana Westmoreland, and Zhengyi Zhang, during my five years of graduate school.

The journey of a PhD can be very challenging at times. I am grateful for the student groups and staff that strive to improve the experience of graduate students, especially my fellow Phi Lambda Upsilon board members.

I would not have survived this process without the support of my friends, in particular Becky Sponenburg and James Schwabacher, that infused these past five years with laughter, many welcome distractions, and memories that I will forever cherish.

I am eternally grateful for my family, especially my parents, who have supported me through every stage of my life and always encouraged me to follow my dreams. From a young age, they both demonstrated the importance of hard work and determination, and without those, I would not have completed this degree.

Lastly, I would like to thank my husband, Louis, for his unconditional support and love. Over the years, he has spent hours enthusiastically discussing my research and providing feedback on my writing and presentations. I am most grateful that he always tries to make my days a little easier, in any way possible.

Table of Contents

List of Figures

List of Tables

List of Schemes

Chapter 1. Introduction

1.1 Chapter Summary

This chapter introduces the importance of the surface chemistry of colloidal quantum dots (QDs) on their functional properties, including their redox activity and catalytic efficiency. First, we define QDs and explain the tools used to characterize their inorganic surfaces and ligand shells. We then discuss the mechanisms by which electrons and holes are transferred from QDs to molecular acceptors. The field of QD photocatalysis is reviewed in brief, highlighting the importance of the surface chemistry and ligand shells of QDs on their performance in photocatalytic applications. This chapter concludes with an outline of the topics discussed in this dissertation.

1.2 Introduction to QDs and their Surface Chemistry

Quantum dots (QDs) are semiconductor nanocrystals with size-tunable optoelectronic properties.[1] They exhibit high quantum yields[2-3] and extinction coefficients[4], which makes them attractive candidates for sensing,[5-6] photocatalysis,[7] and solar-cell applications.[8] Due to their small radius, a large fraction of their ions resides on their surfaces. In order to balance the charge of their surfaces and minimize their surface energies, QDs are covered with ligand molecules. These ligands largely dictate the properties of QDs.[9-13] Thus, before QDs reach their potential in sensing, photocatalysis, and solar-cell applications, a complete understanding of their surface chemistry is imperative.

The ligand layer of QDs acts as a semi-permeable barrier between the inorganic core of QDs and bulk solution.[14] Unlike well-ordered self-assembled monolayers (SAMs) of molecules on the surface of planar substrates (*e.g.* Au or Ag),[15] the ligand molecules on the surface of nanoparticles are more disordered due to the curvature of the substrate, which minimizes intermolecular

interactions between adjacent molecules.[16-17] Furthermore, SAMs on the surface of QDs are more disordered than those on metal nanoparticles due the heterogeneity of their surfaces. This heterogeneity arises from (1) cation-enrichment of QD surfaces due to the synthetic procedures used to make them[18] and (2) the different ions present on the surface facets in QDs (*e.g.* for PbS QDs, the <001> facet contains both Pb^{2+} and S^{2-} ions, while the <111> facet contains only Pb^{2+} ions).[19] While the structure of the inorganic surface of QDs is difficult to directly probe, X-ray photoelectron spectroscopy and vibrational sum frequency generation spectroscopy have been used in concert to identify that disorder in the octylphosphonate ligand shell of CdSe QDs increases with decreasing particle size.[20] For QDs with radii larger than 2.4 nm, the disorder of the ligand layer primarily arises from disorder in the chemical environment of Cd^{2+} ions on the QDs surface. For smaller QDs (radii less than 2.4 nm), the disorder stems from the radius of curvature of the QD and small size of each facet. A significant consequence of the chemical heterogeneity of the inorganic surface of the QDs is that ligands bind to their surfaces through multiple binding modes with varied bond strengths.[21-22]

The chemical properties of the ligands on the surface of QDs affects the solubility, stability, and reactivity of QDs.[23] After synthesis, QDs are typically coated with long, aliphatic ligand molecules that render them soluble in nonpolar solvents. These long ligands are crucial for the synthesis of monodisperse populations of QDs,[24-25] and they preserve their colloidal stability. However, the long ligands limit the reactivity of the QDs by preventing other species in solution from interacting with the inorganic core of the QDs, which is undesirable for many applications.[26] Ligand exchange procedures have been developed to strip the native ligands off the surface of QDs and to replace them with ligands with desirable functionalities, *e.g.* omniphobicity,[27] solubility in

water,[28-29] and enhanced reactivity.[26, 30] The surface chemistry of QDs can therefore be widely tuned due to the large library of ligand molecules.

To characterize and quantify the ligands on the surface of QDs, nuclear magnetic resonance (NMR) spectroscopy and vibrational spectroscopy have been heavily relied upon.[31-33] While vibrational spectroscopy provides information about the binding modes of ligands and the chemical identity of ligands if they contain characteristic vibrational frequencies, it is challenging to quantify the number of ligands present with this technique alone.[32] NMR spectroscopy of QDs provides more detailed insight into the ligand shell, including: the number of ligands present, the strength of the QD surface-ligand bond, and the organization of ligands in mixed monolayers on the QD surface.[32] One-dimensional NMR experiments are useful for quantifying the ligands on the surface of the QD and identifying their binding strength. When a molecule is tethered to the surface of a QD, the transverse relaxation (T_2) of its nuclei is accelerated, which results in broader linewidths for those nuclei.[32] For strongly coupled ligands, *e.g.* thiolates, the NMR peaks of nuclei proximate to the QDs surface broaden such that they are indistinguishable from the baseline. For ligands that participate in dynamic exchange on-and-off the QD surface in the NMR timescale, on the order of seconds, *e.g.* carboxylates, the NMR peaks of the nuclei are broadened but clearly distinguishable. The NMR peaks nuclei of ligands that exchange on-and-off the QD surface faster than the NMR timescale, *e.g.* amines, appear sharp. The binding strength of a ligand greatly impacts the level of passivation and protection it imparts on the inorganic core of a QD, which affects the reactivity and stability of the QD.[34] More complicated NMR pulse sequences can be used to probe the morphology of the ligand shells of nanoparticles that contain multiple components.[35] Patchy, striped, and Janus ligand shells have been identified using Nuclear

Överhauser Effect Spectroscopy (NOESY); the morphology of a mixed ligand layer is dictated by the intermolecular interactions between the component molecules. The morphology of a ligand level affects its wetting, and in biological environments, its cell membrane penetration.[36] With analytical tools, it is possible to characterize the molecules that comprise the ligand shells of QDs.

1.3 Charge Transfer Between Quantum Dots and Molecular Acceptors

When a QD is photoexcited, an electron-hole pair (*i.e.* an exciton) is created. This excited-state QD can relax to its ground state through a variety of radiative and non-radiative processes, including charge transfer to a molecular acceptor if its lowest unoccupied molecular orbital (LUMO) or highest occupied molecular orbital (HOMO) resides within the bandgap of the QD. For a redox acceptor that is statically bound to the inorganic surface of a QD, the rate of charge transfer can be largely described using Marcus theory.[37] When QDs have sufficiently long excited-state lifetimes (*e.g.* ~ 2 μs lifetime of PbS QDs), charge transfer can occur between QDs and freely diffusing molecular acceptors if an acceptor collides with the inorganic surface of a QD before the QD relaxes to its ground state. For a molecular acceptor to reach the inorganic surface of a QD, it must first diffuse through the ligand shell of the QD; this occurs through defects in the ligand layer, which are affected by the chemical properties of the ligands.[38]

The yield of collisionally-gated electron transfer between PbS QDs and quinones, a class of electron acceptors, is dependent upon the size of quinone molecule,[39] the reaction temperature,[38] the binding strength of the ligands on the surface of the QD,[34, 38] and intermolecular interactions between the quinone and ligand molecules.[27] For PbS QDs with an oleate ligand shell, less than one percent of collisions between benzoquinone and QDs result in an electron transfer event.[37] Increasing the steric bulk of benzoquinone by adding substituents decreases the yield of electron

transfer between PbS QDs and the acceptor because larger defects in the ligand shell are required for these molecules to collide with the surface of the QD.[39] Upon increasing temperature, the ligand shell becomes more permeable to benzoquinone due to conformational changes of the oleate ligands and the temperature-dependent dynamic equilibrium of the oleate ligands between bound and free states.[38] This temperature dependent permeability can be eliminated by exchanging the oleate ligands for rigid, tightly binding methylthiolate. Additionally, the protectiveness of the thiolate ligands can be further improved by introducing fluorine atoms into the alkyl-chain of thiolates due to the oleophobicity and steric-bulk of fluorinated molecules.[27] Together, these results demonstrate that collisional quenching between a molecular acceptor and QDs is a sensitive probe for the structure of the QD's ligand shell.

Charge transfer from a QD can be monitored using ground-state or time-resolved spectroscopies. The photoluminescence of a QD is quenched when charge transfer occurs because the charge transfer event prevents radiative recombination.[40] The kinetics of charge transfer can be measured *via* time-correlated single photon counting or transient absorption spectroscopy.[37, 41] By monitoring the decay of excited-state QDs to their ground state with and without molecular acceptors, the rate constant for charge transfer can be measured. Additionally, if the radical of the molecular acceptor has a distinguishable spectral feature in the visible or UV spectrum, the kinetics of charge transfer can be monitored by observing the growth of the radical signal.[42] If a charge transfer event to a molecular acceptor results in an irreversible chemical reaction, charge transfer can be indirectly monitored through the appearance of reaction product. Pioneering work to understand charge transfer between QD and molecular acceptors was crucial for the use of QDs as photoredox catalysts.[43]

1.4 Quantum Dots as Photocatalysts

Photocatalysis is an attractive method for driving chemical transformations because light, the energy input for these reactions, is readily available, easily controlled, and waste-free.[44] The eminent catalysts in this field are Ir and Ru complexes, most of which have peak absorption below 450 nm.[45] Driving a photocatalytic reaction with visible or near-infrared light is advantageous because it avoids directly photoexciting the substrate or product molecules, which limits side reactions.[44-45] By controlling the chemical composition and the size of QDs, QDs can be prepared to exhibit absorption throughout the visible and into the near-infrared spectrum.[18, 46-47] Additionally, due to the quantum-confinement of excitons, CdS QDs exhibit excited-state oxidation potentials up to +1.9 V vs SCE,[48] and $CuInS_2$ QDs exhibit reduction potentials up to -2.4 V vs SCE.[49] In CdSe QDs, the triplet-like excitonic "dark" states are essentially isoenergetic (<20 meV) with their optically active "bright states", rendering them powerful triplet-sensitizers for chemical transformations.[50] These properties of QDs, all of which arise due to the quantum confinement of their excitons, rival that of state-of-the-art photocatalysts.

Photocatalytic systems consist of (1) a photosensitizer, the component of the system that absorbs lights, and (2) a catalyst, the component of the system that drives the reaction. In early demonstrations of QD-mediated photocatalysis, the QDs served as the photosensitizer and transferred either electrons or holes to a co-catalyst, which performed the desired transformation. This approach of driving photochemical reactions with QD photosensitizers has been demonstrated for CO_2 reduction with iron porphyrins[49] and nickel cyclam catalysts,[51] hydrogen evolution with iron bis(benzenedithiolate)[52] and a Ni–dihydrolipoic acid complex,[53] and C-C coupling with a palladium catalyst,[54] among others. QDs can also serve as solo-photocatalysts, acting as both the

light absorber and the catalyst. QDs have been shown to directly photocatalyze C-C bond formation[30, 55-57] and other multi-electron reactions.[48]

1.5 Effects of Surface Chemistry on QD Photocatalysis

Although ligands play a critical role in determining the stability, solubility, and reactivity of QDs, their impact on the optoelectronic properties of QDs is minor compared to the ligands on metal-complexes. Using ligand exchange procedures, the surface chemistry of QDs can be modified to enhance the affinity of substrates to the catalysts. By replacing the native oleate ligands on the surface of CdS QDs for octlyphosphonate ligands, Zhang *et.al.* demonstrated that the rate of a C–C coupling reaction between 1-phenylpyrrolidine (PhPyr) and phenyl *trans*-styryl sulfone is increased.[30] Additionally, substrates or co-catalysts can bind directly to QD surface, which increases the probability of charge transfer or energy transfer from the photoexcited QD before it relaxes to its excited state. Keuhnal *et al.* showed that yield of CO from CO_2 reduction by a Ni(cyclam) catalyst anchored to the surface of a ZnSe QD was three-times greater than by a freely diffusing Ni(cyclam) catalyst.[51] The surface chemistry of QDs offers a powerful route to controlling their photocatalytic performance.

The surface chemistry of QDs can also be tuned to mimic the hierarchical organization of biological catalysts, *e.g.* photosystem II, in which multiple photosensitizers funnel energy or electrons to a single photocatalyst. If QDs are coated with ligands containing charged tails that protrude into bulk solution, their electrostatic interactions can be exploited to produce desirable assemblies with other catalysts or QDs. These electrostatic assemblies have been shown to outperform their non-assembled analogs. When electrostatic assemblies of negatively-charged $CuInS_2$ QD sensitizers and positively-charged iron tetraphenylporphyrin catalysts were used for

CO_2 reduction, the QD sensitization efficiency was a factor of 11 larger than that between uncharged QDs and iron tetraphenylporphyrin catalysts.[58] Kodaimati *et al.* demonstrated that electrostatic assemblies of CdSe QD aggregates, where excitons are funneled through energy transfer from sensitizer QDs to catalyst QDs, can be tuned to increase the internal quantum efficiency of H_2 reduction.[59] The chemical functionality of the ligands on the surface of QDs can significantly impact the reactivity in these systems.

Due to their large surface areas, QDs can serve as scaffolds to stabilize reaction intermediates for multi-electron transformations and to template the organization of reactant molecules. When CdS QDs were used to photocatalyze the six-electron, six-proton reduction of nitrobenzene to aniline, each QD was only photoexcited every 7.1 ms, thus the high-energy intermediates must have persisted for at least 7.1 ms for this reaction to proceed.[48] Jensen *et al*. hypothesized that the surface of the QDs stabilized these intermediates. Recently, CdSe QDs photocatalyzed regio- and diastereoselective intermolecular [2+2] cycloadditions by pre-organizing the reactant molecules on the QD surface through weakly-binding carboxylate acid moieties on the reactants.[57] While the surface of QD catalysts can interact with molecules in solution, these interactions should be transient in nature, either through association with a weakly-binding functional group (*e.g.* carboxylate) or through diffusion-mediated collisions, because if molecules permanently bind to the QD surface they will block catalytic sites and "poison" the catalyst. The surface chemistry of QDs largely dictates how these materials interact with their environment, and thus is an integral part in understanding their reactivity and performance in catalysis and beyond.

1.6 Dissertation Outline

The work in this dissertation is focused on the redox activity of QDs as (1) a probe for the size-dependent structural defects in ligand shells of PbS QDs and (2) a photoreduction catalyst for the deprotection of sulfonyl protected phenols.

In chapter 2, we discuss the mechanisms by which introducing a small fraction of tightly binding fluorinated thiolate ligands into the native oleate ligand layer of PbS QDs protect the QDs from a molecular photo-oxidant, duroquinone. Through a systematic study with three sizes of PbS QDs (R=1.4 nm, 1.5 nm, and 1.6 nm) with equivalent loadings of fluorinated dodecanthiolate ligands that contain 0 – 10 fluorinated carbons, we determined the protectiveness of the fluorinated ligands originate from (1) the strong bond between the surface Pb^{2+} ions and the thiolate anchoring group and (2) the steric bulk and oleophobicity of the fluorinated ligands. The fluorinated ligands are more effective at patching the smaller defects in the ligand layer of 1.6 nm QDs than the larger defects in 1.4 nm and 1.5 nm QDs; the types of defects present in the ligand layer of QDs are a consequence of their synthesis.

Chapter 3 describes the photocatalytic reductive deprotection of phenyl aryl sulfonates by visible-light absorbing $CuInS_2$/ZnS QDs. The rate of deprotection for a series of phenyl aryl sulfonates increases with decreasing electrochemical potential for the electron transfers required for liberation of phenol. Interestingly, the rate of QD-catalyzed deprotection of a substrate that contains a carboxylic acid, a known QD-binding group, is accelerated by more than a factor of ten than what is expected from the electrochemical potential required for the transformation; this result highlights the impact of surface chemistry on the catalytic performance of QDs. The orthogonality and the functional group tolerance of this deprotection protection are also explored.

In chapter 4, we summarize the major findings of this research and discuss potential future directions.

Chapter 2. Mechanisms of Defect Passivation by Fluorinated Alkylthiolates on PbS Quantum Dots

Adapted From: **Perez, K.A.**, Lian, S., Kodaimati, M.S., He, C., Weiss, E. A. *J. Phys. Chem. C.* **2018**, *122*, 13911–13919.

2.1 Chapter Summary

Defects in the organic ligand layer on the surfaces of colloidal quantum dots (QDs) provide pathways for corrosive molecules to penetrate to the QD core. This chapter describes the decrease in the permeability of the ligand shells of colloidal near-infrared-emitting PbS QDs to the molecular photo-oxidant, duroquinone (Me_4BQ), upon substituting a small fraction of their oleate ligands with either 1-dodecanthiolate (DDT) or progressively fluorinated DDT analogues (with between 1 and 10 fluorinated carbons), as measured by the yield of collisionally gated photoinduced electron transfer from the QD to Me_4BQ. The permeabilities of mixed-monolayer ligand shells of oleate and 8-16% (by surface area) DDT are 35-41% lower than those of the pure oleate monolayers. Increasing the number of fluorinated carbons in the thiolate ligands from 0 to 10 results in an additional 40-66% decrease in the permeability of the ligand shell; as few as 0.05% of collisions between the largest QDs and Me_4BQ result in electron transfer. The thiolate exchange, and fluorination of the thiolate ligands, more effectively protect the largest QDs than the smallest QDs, primarily due to the size-dependence of the types of defects in the native oleate monolayers.

2.2 Ligand Shells of QDs act as Semi-Permeable Membranes that Gate Interactions Between Inorganic Core of QD and Bulk Solution

The ligand shells of quasi-spherical colloidal semiconductor quantum dots (QDs) are semi-permeable barriers between bulk solution and the inorganic core of the particle,[14, 60] and thereby control the solubility,[61-62] biocompatibility,[63-64] and catalytic activity of the QDs.[30] Organic adlayers on QDs are not as ordered as self-assembled monolayers (SAMs) on planar metal or semiconductor substrates, or even as ordered as the adlayers on metal nanoparticles.[20] For planar SAMs, the chemical structure of the component molecules and the degree of epitaxy of the

molecular lattice with the lattice of the underlying substrate are the main determinants of density and ordering;[65-66] defects are a perturbation to their intermolecular structure.[15, 43] The ligand shells of smaller metal nanoparticles (MNPs) are more disordered and defective than the ligand shells of larger MNPs because the cone angle that each ligand explores increases with increasing curvature of the MNP surface.[16-17] The arrangement of organic molecules within QD adlayers is influenced by the radius of curvature of the particle, but also by the substantial chemical and structural disorder of the underlying substrate, which varies based on the final cation-to-anion ratio and degree of faceting of the particle, and the charges and relative binding strengths of the surfactants used in the synthesis (these characteristics are interdependent).[17, 20] Furthermore, the best surfactants for nucleation and growth of monodisperse, highly emissive QDs are typically molecules that have a variety of binding modes with a range of binding affinities, including populations that are in fast exchange on and off the QD surface.[67] Use of QDs coated in these labile "native" ligands for applications in complex chemical environments, like chemical or biological sensing or tagging, introduces additional transient defects,[34, 38] namely pinholes or bare spots in the monolayer that exist during the off-time of the ligands. These defects leave the QDs vulnerable to adsorption of ions and small molecules and subsequent corrosion, especially mediated by photo-redox processes, since most QD applications involve photoexciting them at energies at or above their bandgaps.[68-69]

Omniphobic fluorinated ligands are widely used to create oxidation-resistant, antifouling,[70] and superhydrophobic[71-72] coatings and are therefore appealing as protective layers for nanoparticles. Fluorinated ligands are however time-consuming to synthesize, and sparingly soluble in any solvent except expensive, fluorinated solvents and supercritical carbon dioxide

(even if they are not perfluorinated);[73-74] thus, for widely applicable, robust QDs, it is advantageous to only use fluorinated ligands as minority components of the QD's monolayer, and to use ligands with as few fluorinated carbons as possible.

This chapter illuminates some of the complex characteristics of a QD's ligand shell that allow it to inhibit the approach of molecules to the inorganic core of the QD, and any redox processes that might result from subsequent adsorption or collision.[22, 75-76] We describe the mechanisms by which integration of small surface densities of alkylthiolate and partially fluorinated alkylthiolate ligands (with between one and ten fluorinated carbons) into the native oleate ligand shells of PbS QDs dramatically reduces the number of defects within these adlayers, as measured by a decrease in their permeability to a molecular photo-oxidant, 2,3,5,6-tetramethyl-1,4-benzoquinone (Me_4BQ), by up to 84%. Our previous study of the permeability of a mixed oleate-perfluorinated decanethiolate ligand shell used two different sizes of molecular photo-oxidants to demonstrate that both size-exclusion and oleophobicity play a role in the protective properties of a partially fluorinated ligand shell.[27] Here, we show that the effectiveness of the thiolate passivation strategy – and the dependence of the protectiveness of the fluorinated thiolates on the degree of fluorination – depends on the size of the QDs; specifically, larger QDs are easier to protect than smaller QDs. This size-dependence does not, however, appear to originate from the decrease in radius of curvature – and therefore increased "splaying" of ligands – with decreasing QD size. In fact, our nuclear magnetic resonance (NMR) and elemental analyses show that there is a *higher* density of ligands at all points within the ligand shells of the smaller PbS QDs (R = 1.4 nm and 1.5 nm) than the largest (R = 1.6 nm) PbS QDs, due to a higher degree of Pb^{2+} enrichment of their surfaces. The fact that the ligand shells of smaller QDs are more permeable *despite* their higher total ligand

density indicates that one must also examine the nature of the defects within the monolayer that allow permeation of a molecule, and how effectively these defects can be "healed" by ligand exchange. In the case we consider, although excess Pb^{2+} on the surfaces of the QDs leads to a higher overall ligand density, our data suggest that it also supports the formation of weakly bound $Pb(oleate)_2$ "Z-type" ligands that constitute defect sites within the adlayer. These defects are larger and therefore less effectively filled by the fluorinated alkylthiolates than are the pinhole-type defects in the adlayers of larger QDs.

2.3 The Chemistry of the Ligand Exchange, and the Compositions of Mixed Monolayers on QD Surfaces.

We synthesized a series of PbS quantum dots with average radii of 1.4, 1.5, and 1.6 nm using adapted literature procedures,[77] and then used ligand exchange to prepare QDs with mixed monolayers of oleate and dodecanethiolate (OA/DDT) or oleate and one of the fluorinated dodecanethiolates: 12,12,12-Trifluorododecane-1-thiolate (F1DDT), 9,9,10,10,11,11,12,12,12-Nonafluorododecane-1-thiolate (F4DDT), 1H,1H,2H,2H,3H,3H,4H,4H-Perfluorododecaneanthiolate (F8DDT), or 1H,1H,2H,2H-Perfluorododecanethiolate (F10DDT), **Figure 2.1**. Details of these procedures and optical spectra (**Figure 2.4**) and TEM images (with size histograms) of the QDs (Figures **2.5-2.6**) are in section 2.6.

We purchased DDT from Sigma-Aldrich and F1DDT and F4DDT from Synquest Laboratories and used them as-received. We synthesized F8DDT and F10DDT according to a literature procedure, see section 2.6.[78]

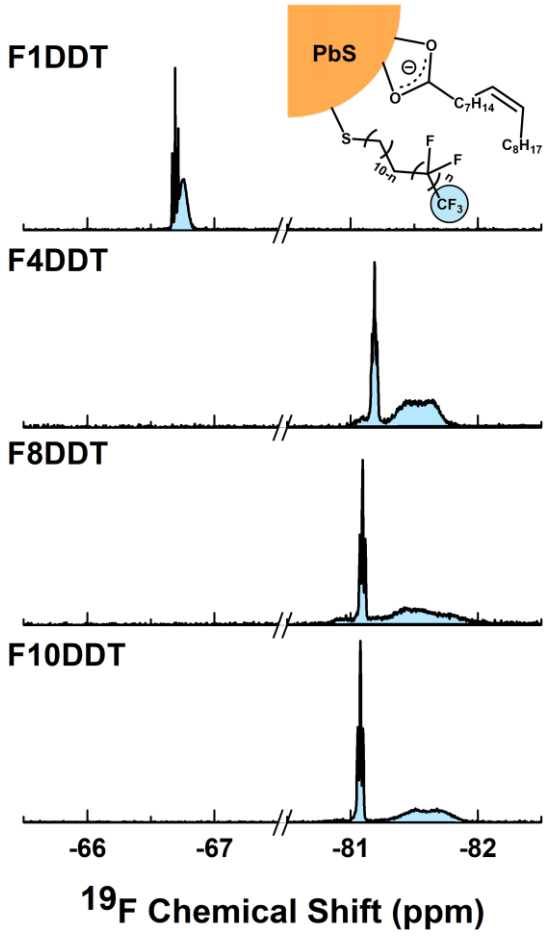

Figure 2.1. ^{19}F NMR spectra for PbS QDs (R = 1.6 nm) with monolayers of OA/F1DDT, OA/F4DDT, OA/F8DDT, and OA/F10DDT. The broad feature corresponds to thiolate ligands that are primarily bound to a QD surface and the sharp features correspond to thiolate ligands that are primarily free in solution. *Inset*: A schematic diagram of a PbS QD and one of each type of ligand in the mixed monolayer of oleate (OA) and fluorinated dodecanethiolate, where n = 0, 3, 7, or 9.

To quantify the compositions of the ligand shells of the QDs after the ligand exchange, we used well-established NMR procedures, see the section 2.6 for details.[27, 33] Solution phase NMR spectroscopy is well-suited for this type of measurement because (i) NMR and optical measurements are collected on the same solution-phase sample, (ii) NMR clearly distinguishes

between molecular species that contain the same elements, and (iii) linewidths of NMR signals differentiate molecules that are bound to the surface of the QD from those that are free in solution, and provides information about their binding constants.[33, 79]

Tables **2.1**-**2.3** summarize the NMR-derived compositions of the mixed monolayers of each size of QD. We counted the number of OA molecules that remain bound to the surface of the QD and the number that are displaced by the added thiol molecules by integrating the olefinic proton signals (5.7 ppm) in the ^{1}H NMR spectrum of the QDs, Tables **2.1**-**2.3**, columns 3 and 4. The proton signals from bound and free DDT are inseparable from the signals from aliphatic protons of OA, but we know, from previous work,[27] that all DDT either binds to the QDs or degrades to one product, didodecyl disulfide. We therefore counted the number of bound DDT per QD by subtracting the concentration of the disulfide, measured from the integrated intensity of its ^{1}H NMR signals, from the amount of DDT added, Tables **2.1**-**2.3**, column 5, row 2. We counted the number of bound F1DDT, F4DDT, F8DDT, and F10DDT directly, by integrating the signals from their terminal $–CF_3$ groups within the ^{19}F NMR spectra of the QDs, **Figure 2.1** and **Tables 2.1**-**2.3**, column 5, rows 3-6. The broad signals in the ^{19}F NMR spectra correspond to nuclei in ligands that are primarily bound to the surface of QD, while the sharp signals correspond to nuclei from ligands that are primarily free in solution.

Based on the estimated surface areas of the QDs and the total number of bound ligands of each type per QD, the mixed monolayer ligand shells are 10±2% thiolate and 90±3% OA (for the 1.4-nm QDs), 8.1±0.7% thiolate and 92±2% OA (for the 1.5-nm QDs), and 14±1% thiolate and 86±3% OA (for the 1.6-nm QDs). These compositions apply to all thiolates (DDT and all

Table 2.1. Composition of the Mixed Oleate/Thiolate Monolayers on 1.4 nm PbS QDs.

Thiol	Equiv. thiol added per QD	Bound OA/QD	Displaced OA/QD	Bound thiolate/ QD	# thiolate/ nm^{2a}	# OA/ nm^{2a}	# Total ligands (OA + thiolate) /nm^{2a}
none	0	240 ± 70[b]	0	0	0	10 ± 3	10 ± 3
DDT	17	115 ± 8	41 ± 2	17	0.73 ± 0.09	4.9 ± 0.7	5.7 ± 0.7
F1DDT	18	179 ± 3	50 ± 10	15 ± 3	0.7 ± 0.2	7.7 ± 0.9	8.3 ± 0.9
F4DDT	19	160 ± 10	53 ± 4	16 ± 1	0.7 ± 0.1	6.9 ± 0.9	7.6 ± 0.9
F8DDT	19	145 ± 5	40 ± 10	16 ± 2	0.7 ± 0.1	6.3 ± 0.8	7.0 ± 0.8
F10DDT	22	176 ± 6	60 ± 10	16 ± 2	0.7 ± 0.1	7.6 ± 0.9	8.3 ± 0.9

[a]Defined as the number of bound thiolate, OA, or total ligands (the sum of OA and thiolates) per unit surface area, where the surface area is 23 ± 3 nm^2 as estimated from the radius of the QD determined from absorption spectra and the linewidth of the PL spectra. [b]The large error is probably a result of a large population of weakly bound oleate ligands (in the form of Pb-oleate complexes or clusters) that are separated from the QDs to varying degrees during purification.

Table 2.2. Composition of the Mixed Oleate/Thiolate Monolayers on 1.5 nm PbS QDs.

Thiol	Equiv. thiol added per QD	Bound OA/QD	Displaced OA/QD	Bound thiolate/ QD	# thiolate/ nm^{2a}	# OA/ nm^{2a}	# Total ligands (OA + thiolate) /nm^{2a}
none	0	270 ± 10	0	0	0	10 ± 1	10 ± 1
DDT	20	205 ± 7	79 ± 7	19 ± 2	0.7 ± 0.1	7.4 ± 0.9	8.0 ± 0.9
F1DDT	22	227 ± 8	66 ± 3	18.8 ± 0.4	0.67 ± 0.08	8 ± 1	9 ± 1
F4DDT	22	224 ± 5	60 ± 10	17 ± 1	0.62 ± 0.09	8 ± 1	9 ± 1
F8DDT	24	191 ± 4	57 ± 1	18.7 ± 0.4	0.67 ± 0.08	6.9 ± 0.8	7.5 ± 0.8
F10DDT	25	191 ± 4	63 ± 4	18 ± 1	0.65 ± 0.09	6.9 ± 0.8	7.5 ± 0.8

[a]Defined as the number of bound thiolate, OA, or total ligands (the sum of OA and thiolates) per unit surface area, where the surface area is 28 ± 3 nm^2 as estimated from the radius of the QD determined from absorption spectra and the linewidth of the PL spectra.

Table 2.3. Composition of the Mixed Oleate/Thiolate Monolayers on 1.6 nm PbS QDs.

Thiol	Equiv. thiol added per QD	Bound OA/QD	Displaced OA/QD	Bound thiolate/ QD	# thiolate/ nm^{2a}	# OA/ nm^{2a}	# Total ligands (OA + thiolate) /nm^{2a}
none	0	230 ± 20	0	0	0	7 ± 1	7 ± 1
DDT	40	141 ± 6	50 ± 10	26 ± 3	0.8 ± 0.1	4.4 ± 0.6	5.2 ± 0.6
F1DDT	36	178 ± 10	64 ± 9	26 ± 1	0.8 ± 0.1	5.5 ± 0.8	6.3 ± 0.8
F4DDT	42	170 ± 10	32 ± 5	26 ± 2	0.8 ± 0.1	5.3 ± 0.7	6.1 ± 0.7
F8DDT	50	150 ± 10	56 ± 2	27 ± 3	0.8 ± 0.1	4.7 ± 0.7	5.5 ± 0.7
F10DDT	40	160 ± 10	53 ± 5	27 ± 4	0.8 ± 0.2	5.0 ± 0.7	5.8 ± 0.7

[a]Defined as the number of bound thiolate, OA, or total ligands (the sum of OA and thiolates) per unit surface area, where the surface area is 32 ± 4 nm^2 as estimated from the radius of the QD determined from absorption spectra and the linewidth of the PL spectra.

fluorinated DDTs); therefore, for a given size of QD, the density of thiolates remains constant regardless of the degree of fluorination.

There is a substantial literature on organization of fluorinated ligands on nanoparticles.[36, 73, 80-82] Perhaps most relevant to our system is the investigation of Şologan *et al.* into mixed monolayers of fluorinated and hydrogenated alkylthiolates.[80] At coverages of fluorinated ligands similar to ours (10-20% of the monolayer), they observed either stripe-like domains or small patches of fluorinated ligands (depending on the length of the hydrogenated ligand).[80] Those results were however collected on monolayers where all ligands had straight-chain carbon backbones. Şologan did not observe *any* phase segregation in mixtures of *branched* hydrogenated thiolates and straight-chain fluorinated thiolates because the branched ligands disrupt the formation of crystalline domains. We believe this latter result is most analogous to our work because our hydrogenated ligand, and the majority component of our monolayers, is oleate, which is kinked and forms more disordered monolayers than *trans*-extended ligands. Without long-range intermolecular order in 85-92% of our monolayers (the % occupied by the oleate ligands), there is no driving force for reorganization of the fluorinated ligands into patches or stripes. Instead, we suspect (but have not proven) that the mixed ligand layer is in a kinetically trapped structure, where the thiolate ligands irreversibly bind to the most accessible sites on the surface of QD.

Previous work and our current NMR data allow us to determine the probable chemistry of ligand exchange from OA to thiolates.[83-84] Most OA species are in fast exchange on and off the surface of the QD,[21, 85] but some species spend a higher fraction of time bound than do others. The binding affinity of OA to the QD surface depends on its protonation state, and on the type of Pb^{2+} and facet to which it binds.[86] Oleic acid binds weakly as a neutral acid and more strongly as

negatively charged oleate, in either bridging or chelating mode.[21, 87] OA bound to a Pb^{2+} that is incorporated into the PbS lattice of the QD typically must be displaced by incoming protonated species (another carboxylic acid or thiol) by proton exchange.[85] This process is less facile than displacement of OA from the surface of the QD as $Pb(oleate)_2$ (a so-called "Z-type ligand") or a small $Pb_x(oleate)_y$ cluster, weakly adsorbing species that originate from the anionic surfactant mixture used in the synthesis, which produces Pb-enriched QDs.[77]

Our NMR data show that each thiolate molecule displaces an average of 2.6±0.2 OA molecules for the 1.4-nm QDs, 2.9±0.6 OA molecules for the 1.5-nm QDs, and 1.2±0.4 OA molecules for the 1.6-nm QDs. These data imply that, for the two smaller sizes of QDs, each thiol is displacing, on average, a Z-type Pb-$(oleate)_2$ ligand or a small $Pb_2(oleate)_4$ cluster, whereas, for the largest size, the thiol is displacing a single oleic acid or oleate ligand.[85, 88] In each case, the incoming thiol almost certainly binds as a thiolate, rather than a thiol, to an underlying Pb^{2+}, due to the strength of the Pb-S bond (10^8 larger binding constant than a Pb-OOC bond).[89] In cases where the thiolate displaces a neutral molecule, we suspect, but have not proven, that an adsorbed H^+ balances the charge. These NMR-derived displacement ratios are consistent with results of inductively coupled plasma optical emission spectrometry, which show that the Pb^{2+} enrichment of the OA-capped QDs (and therefore the concentration of surface-adsorbed $Pb_x(oleate)_y$ species) decreases with increasing size of the QD; specifically, Pb:S = 2.0:1 for the 1.4-nm QDs, 1.8:1 for the 1.5-nm QDs, and 1.6:1 for the 1.6-nm QDs, see section 2.6. The presence of non-lattice-bound oleate species on the QD surface also explains the anomalously high densities of oleate ligands on as-purified QDs (**Tables 2.1-2.3**, Row 1); this density decreases with increasing size of the QD, consistent with the trend in measured Pb:S ratios.

The linewidths of the NMR signals of displaced oleate ligands show that they are still in exchange between free and bound states, but spend more time off the QD surface than do the ligands that we classify as "bound". By comparing the chemical shifts of the displaced ligands shown in **Figure 2.10** of section 2.6, we find that the ligands displaced from 1.6-nm QDs spend more time off the QD surface (and less time bound) than the ligands displaced from the smaller two sizes of QDs (1.4- and 1.5-nm). This result does not prove, but is consistent with, our hypothesis that primarily Z-type Pb-$(oleate)_2$ ligands are displaced from 1.4-nm and 1.5-nm QDs and primarily oleic acid is displaced from 1.6-nm QDs. Exchange of oleic acid between free and bound states requires a proton exchange with bound oleate,[85] and is therefore less probable than the more non-specific adsorption of Pb-$(oleate)_2$.

2.4 The Protectiveness of Mixed Oleate/Thiolate Monolayers with Fluorinated and Unfluorinated Thiolates.

We assess the protectiveness of the ligand shells of the QDs using a molecular redox probe. We collected PL spectra of 13 μM solutions of QDs (of all three sizes) capped with OA or mixed monolayers of OA and 0.72 ± 0.09 nm^{-2} of DDT, F1DDT, F4DDT, F8DDT, or F10DDT, and treated with 0 – 2200 molar equivalents of the photo-oxidant Me_4BQ, **Figure 2.2A** (inset). **Figure 2.2A** shows a representative set of PL spectra of 1.6-nm PbS QDs coated exclusively with OA. The PL intensity of these QDs, and of QDs with all monolayer compositions, decreases with increasing concentrations of Me_4BQ. We quantify this relationship by dividing the integrated PL intensity of the sample with no added Me_4BQ by the integrated PL intensity of the sample with added Me_4BQ, at a series of concentrations of Me_4BQ, and denote this quantity as "PL_0/PL". **Figures 2.2B-D** are plots of PL_0/PL versus the concentration of added Me_4BQ for all three sizes

QDs with each monolayer composition. In all cases, these plots fit well to the Stern-Volmer equation, **eq 2.1** ($R^2 > 0.98$), consistent with our previous assignment of this quenching as

$$\frac{PL_0}{PL} = 1 + k_q\tau_0[Me_4BQ] \quad (2.1)$$

collisionally gated electron transfer from the photoexcited QD to Me_4BQ ("dynamic quenching"). In **eq 2.1**, k_q is the bimolecular quenching rate constant and τ_0 is the excitonic lifetime of the QDs in the absence of Me_4BQ, which we measure for each monolayer composition using transient absorption (TA) spectroscopy, see section 2.6, **Table 2.4**. For a collisionally-gated electron transfer event to occur, a Me_4BQ molecule, a weakly binding molecular probe, must permeate through the ligand shell during the lifetime of the QD exciton to within a few angstroms of the core. More efficient PL quenching is therefore directly correlated with a more permeable monolayer.[27, 39]

In order to compare the permeabilities of ligand shells of different composition, on QDs that may have slightly different hydrodynamic radii and exciton lifetimes, we define the collisional quenching efficiency, ϕ, **eq 2.2**, in which k_q is calculated from the slope of the Stern-Volmer plot

$$\phi = \frac{k_q}{k_0} \quad (2.2)$$

in **Figures 2.2B-D**, and k_0 is the diffusion-limited collision frequency. k_0 is dictated by the diffusion constants, hydrodynamic radii, both measured by diffusion-ordered spectroscopy (DOSY) NMR, and the contact radius of Me_4BQ and the QD, see section 2.6, **Figure 2.11** and **Table 2.5**.[27, 39] A larger value of ϕ corresponds to a more permeable ligand shell.

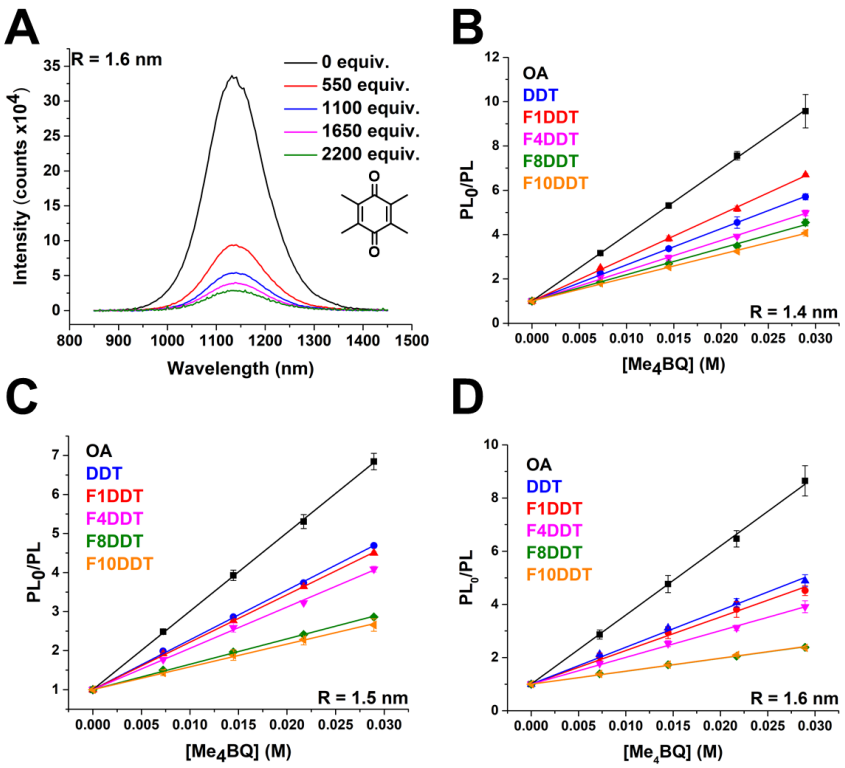

Figure 2.2. A) PL spectra of 1.6-nm PbS QDs (13 μM in benzene-d_6) coated exclusively with OA, collected 12 hr after the addition of 0-2200 molar equiv. of the quencher Me_4BQ, upon photoexcitation at 800 nm. **B-D)** Plots of PL_0/PL (solid symbols), defined in the text, for 1.4 nm (**B**), 1.5 nm (**C**), and 1.6 nm (**D**) PbS QDs (13.0 μM in benzene-d_6), in which the PbS QDs are coated with 0.72 ± 0.09 nm^{-2} of DDT (blue), F1DDT (red), F4DDT (pink), F8DDT (green), or F10DDT (orange) *vs.* the concentration of added Me_4BQ. Colored lines correspond to fits of the data to **eq 2.1**. The error bars are standard deviations of the mean of at least three separate measurements on independently prepared samples.

The collisional quenching efficiencies for all three sizes of OA-coated QDs, even before any ligand exchange, are <1%, see section 2.6, **Table 2.6**. Although this result indicates that permeation of Me_4BQ to within a few angstroms of the QD core is a rare event (occurring, in our mixtures, once every 0.2 μs when 1000 equiv. of Me_4BQ are added), it only takes one photo-oxidation event to permanently quench the PL of a QD and initiate corrosion, if recombination is slow and the photogenerated hole is not scavenged. It is therefore important to eliminate these

redox processes, especially in applications that require emission from the QDs. **Figure 2.3A** shows that OA/DDT ligand shells that are only 10±2% (1.4-nm QDs), 8.1±0.7% (1.5-nm QDs), or 14±1%

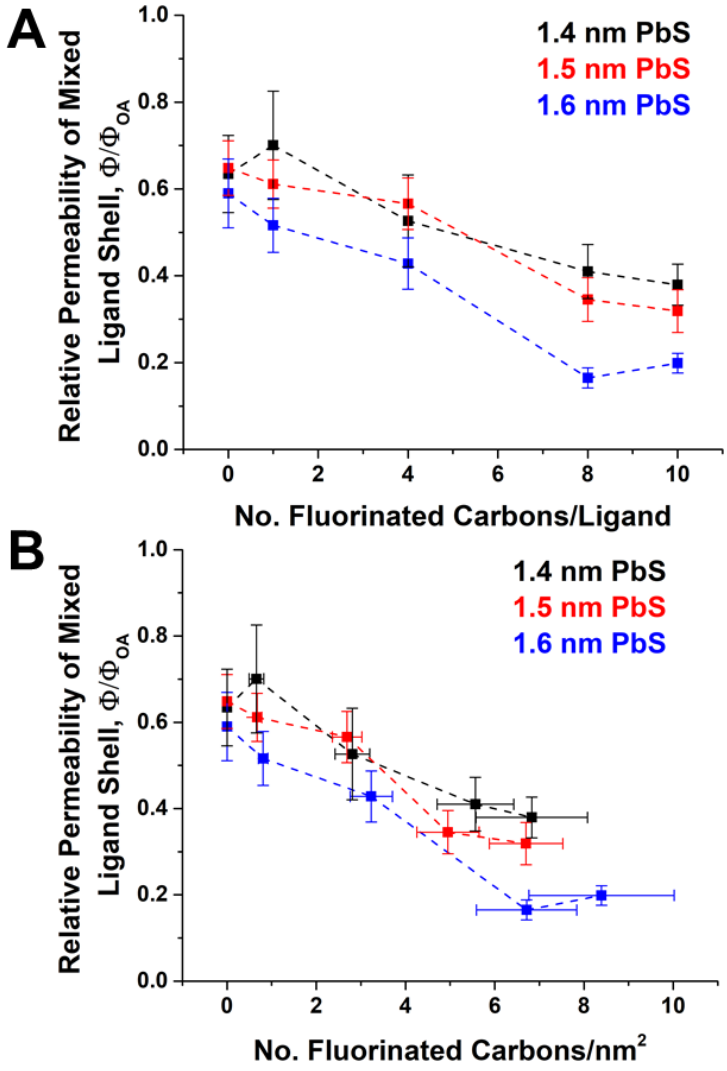

Figure 2.3. Plots of the permeability of the mixed oleate-thiolate ligand shell (quantified as ϕ/ϕ_{OA}, the collisional quenching efficiency for Me_4BQ and the QDs with each of the mixed monolayers) relative to that for Me_4BQ and the QDs with a pure oleate monolayer) *vs.* the number of fluorinated carbons of the thiolate ligand in the mixed monolayer, for PbS QDs with radii of 1.4 nm, 1.5 nm, and 1.6 nm, *vs.* **A)** the number of fluorinated carbons in each thiolate, and **B)** the density of fluorinated carbons per nm^2 as calculated from the density of ligands at the inorganic surface of the QDs. The results for the QDs with OA/DDT monolayers have x-coordinate of "0". The surface density of thiolate molecules is 0.72 ± 0.09 nm^{-2} in all cases. The error bars are standard deviations of the mean of at least three separate measurements on independently prepared samples.

(1.6-nm QDs) of DDT (with no fluorination) are 35% - 41% less permeable than pure OA ligand shells, despite equally dense or less dense total ligand coverage.

The two results outlined in the previous paragraph together indicate that the probability that a collision between the QD and Me_4BQ leads to photoinduced electron transfer is dictated not by the permeability of the "bulk" ordered portions of the monolayer, but by the presence of highly defective regions of the ligand shell that provide pathways for the molecule from the solvent to the QD core. In this sense, the factors one should consider in analyzing the protectiveness of these nanoparticulate monolayers as a function of their composition are very different than those one considers when studying planar SAMs. Specifically, the role of the thiolates, as minority components of the monolayer, in determining the permeability of the ligand shell is to "plug" bare spots and pinholes in the OA monolayer, not to dictate the intermolecular structure of the bulk of e monolayer. Given that unfluorinated DDT is neither sterically nor electronically more obstructive than OA, we conclude that it protects the surface of the QD more effectively than OA because the thiolate headgroup binds much more tightly to the QD surface than does the carboxylate or carboxylic acid headgroup, and certainly more tightly than the Z-type $Pb(oleate)_2$ complexes, and thus the mixed OA/thiolate monolayer is, on average, more densely packed than the pure OA monolayer, pictured in cross-sectional view in **Scheme 2.1A,B**.

By increasing the number of fluorinated carbons in the thiolate ligands from zero to ten, the permeability of the ligand shell to Me_4BQ decreases by an additional 40±10% (1.4-nm QDs), 51±9% (1.5-nm QDs), or 66±6% (1.6-nm QDs), **Figure 2.3A**, even though, by NMR, the thiolate coverage and the total ligand coverage are constant within measurement error (and show no trend even if we disregard the error bars). The impact of fluorination on the permeability of planar and

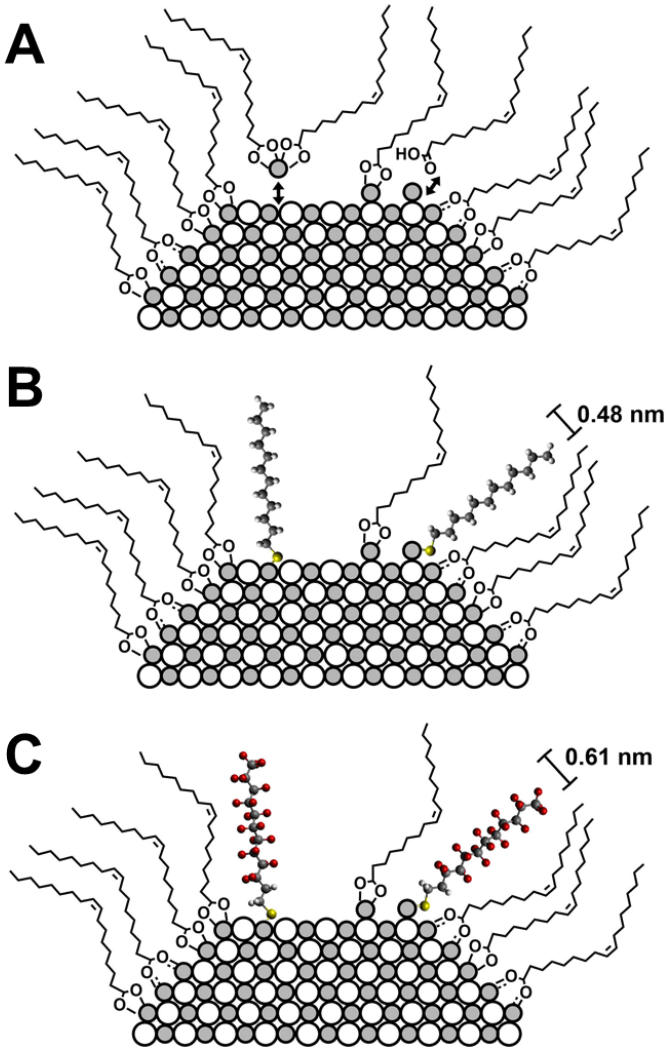

Scheme 2.1. Cross-sections of portions of the surface of (**A**) OA-capped QDs, (**B**) OA/DDT capped QDs, and (**C**) OA/F10DDT capped QDs. In **A**, sites transiently occupied by $Pb(oleate)_2$ are "bare spot"-type defects and sites transiently occupied by neutral oleic acid are "pinhole"-type defects in the monolayer that are plugged by tighter binding DDT (**B**) or F10DDT (**C**). The molecular diameters of DDT and F1**0**DDT are calculated from electron density maps, see the **Figure 2.13**.

nanoparticulate monolayers is related to both their larger molecular volume (than their hydrogenated analogs, **Scheme 2.1B,C**) and their oleophobicity.[27, 90] Specifically, the fluorinated segments of the thiolate ligands (when there four or more fluorinated carbons in the ligand) form rigid helices due to the polarization of the C-F bonds; the helical conformations are larger than

they would be if they were *trans*-extended. Section 2.6, **Figure 2.12**, contains density functional theory-optimized structures of each thiolate ligand. The molecular diameter of the fluorinated region of F10DDT is a factor of 1.3 greater than the molecular diameter of DDT as estimated from the electron density maps of the molecules. Furthermore, as the thiolate ligands are progressively fluorinated, van der Waals interactions between Me_4BQ and the ligand shell become increasingly less favorable than those between Me_4BQ and the solvent due to the low polarizability of the C–F groups.[66, 91]

Figure 2.3B is a plot of the permeability of each monolayer (the same data as in **Figure 2.3A**) *vs*. the number of fluorinated carbons per nm^2 of particle surface (= number of fluorinated carbons per thiolate ligand × surface density of thiolate ligands). This *x*-axis allows us to compare the protectiveness of the monolayers on different sizes of QDs, because it accounts for any variance in the density of ligands at the nanoparticle surface from size to size. For instance, as one can see from **Figure 2.3B**, our surface coverages of thiolates were consistently slightly higher for the largest QDs than for the two smallest sizes. We emphasize that, on going from left to right along the *x*-axis of this plot, we are not increasing the number of thiolate ligands per nm^2, but rather the number of C-F bonds per thiolate. If we examine a series of vertical slices of the permeability plots in **Figure 2.3B**, we find that the size of the QD does not impose a statistically significant effect on the ability of the thiolates to patch defects on the monolayer until we reach a threshold level of fluorination of the ligands, specifically, at ≥~6.7 fluorinated carbons/nm^2. We believe that the greater influence of fluorination for the largest QDs than for the smaller QDs is due to the fact that, as indicated by our NMR-derived displacement ratios, the defects in the OA monolayer of the largest QDs are pinhole-type defects at the sites of labile single oleic acid molecules, whereas

defects in the monolayer of the smaller QDs are larger bare spot-type defects at the sites of labile $Pb(oleate)_2$ complexes, **Scheme 2.1**. It appears that the steric hindrance of a highly fluorinated ligand is an effective protection mechanism, but a single highly fluorinated ligand passivates defects more effectively if those defects have the footprint of an oleic acid molecule rather than a $Pb(oleate)_2$ molecule.

It is tempting to also attribute the greater permeability of the monolayers on the smaller QDs to the increased curvature of their surfaces, which increases the cone angle explored by each ligand and, over certain ranges of core sizes and ligand lengths, results in less dense packing of the ligands at the outer edge of the ligand shell.[17] For our set of core sizes and ligand lengths, however, the density of ligands at the outer edge of a spherical OA/thiolate ligand shell (assuming every ligand is *trans*-extended) is actually the same or smaller for the larger QDs than for the smaller QDs, for a given density bound at the nanoparticle surface, see section 2.6. The "splaying" of ligands, while important to some degree in the intermolecular order of nanoparticle ligand shells, is therefore not as important as the chemistry of the QD surface in determining the permeability of monolayers on small PbS QDs.

Finally, we note that, for the largest size of QDs, we do not observe a further decrease in the ligand shell permeability as the number of fluorinated carbons increases from eight to ten. A similar plateau was reported for the work of adhesion of fluorinated self-assembled monolayers (FSAMs) with both nonpolar and polar contacting liquids by Lee and coworkers, but its onset was at four, rather than eight, fluorinated carbons.[92] We suspect, but have not proven, that the delayed onset of the plateau in our data (also a characteristic of the work of adhesion of films of our PbS QDs to a polar contacting liquid, see **Figure 2.14** of section 2.6) exists primarily because our QDs

have less than a 20% surface coverage of fluorinated thiolates while the planar SAMs used in Lee's work are 100% fluorinated thiolates.

2.5 Chapter Conclusions

We have shown that replacing only 8-16% of the native oleate/oleic acid ligands on the surfaces of PbS QDs with dodecanethiolate (DDT) decreases the permeability of the ligand shell of the QDs to duroquinone (Me_4BQ) by 35% - 41% (despite equally dense or less dense total ligand coverage), and that fluorinating the DDT ligands with up to 10 F's per molecule decreases the permeability an additional 40% - 66%. QDs of radius 1.6 nm with 15±2% surface coverage of 1H,1H,2H,2H,3H,3H,4H,4H-Perfluorododecaneanthiolate (F8DDT) or 14±2% surface coverage of 1H,1H,2H,2H-Perfluorododecanethiolate (F10DDT) have collisional quenching efficiencies (defined as the fraction of collisions of the QD and Me_4BQ that result in photo-oxidation of the QD) of just 0.047±0.006% or 0.057±0.005%, respectively. We conclude that the mechanism by which a small surface coverage of thiolate or fluorinated thiolate disproportionately improves the protectiveness of the monolayer is by displacing weakly bound oleate species, which constitute transient defect sites within the monolayer, with more tightly bound thiolates. These thiolates occupy increasing space, and become increasingly oleophobic, with increasing fluorination. NMR data suggest that these weakly bound oleate species are mostly oleic acid for the largest QDs and $Pb(oleate)_2$ for the smaller QDs. The size of the QD does not have a statistically significant effect on the permeability of the mixed OA/thiolate monolayers (relative to that of the pure OA monolayer) unless the thiolate is highly fluorinated (F8DDT or F10DDT), probably because these two molecules are bulky enough to plug the pinhole-type defects (that originate from displacement

of a single OA) in the monolayers of the largest QDs, but not bulky enough to fill the bare-spot-type defects (that originate from displacement of $Pb(oleate)_2$) of the smaller QDs.

Our assertion that the thiolates patch defects in the monolayer comes from two facts (one is logical and the other is empirical). First, in a ligand exchange process, the incoming ligands will first occupy bare spots in the monolayer (if there are any), and second replace the ligands with the lowest binding affinity for the QD surface, assuming that removing the original ligands reveals appropriate binding sites for the incoming ligands. These bare spots and weakly binding ligands, are, by definition, defects that increase the permeability of the monolayer to a small molecule. Second, addition of a small amount of DDT (with no fluorination) decreases the permeability of the monolayers by ~40%. In fact, in a separate study, we fully exchanged an oleate monolayer on a PbS QD for a decanethiolate monolayer and found that the decanethiolate layer completely shuts off charge transfer to a molecular probe, aminoferrocene, even though decanethiolate is approximately half the length of oleate and does not form highly ordered SAMs, even on crystalline gold.[89] So, while one might at first argue that the protectiveness of a fluorinated thiolate monolayer originates from the intermolecular structure and oleophobicity of the fluorinated portions of the molecules, we show here that the primary reason that these monolayers are protective is because of their high-affinity thiolate binding groups, not because of their fluorination. The fluorinated DDTs provide additional protection through both size exclusion and their oleophobicity.[27]

In previous work, we determined that the degree of Cd^{2+} enrichment of CdSe QDs, where excess Cd^{2+} is in the form of a polymer-like Cd-phosphonate adlayer on the crystalline CdSe core, has a larger role in dictating the intermolecular ordering of alkylphosphonate layers on CdSe QDs

than does the geometry of the nominally spherical particle.[20] Here, similarly, we find that the permeability of the ligand shell of a PbS QD, which, like average intermolecular order, is related to average packing density and the presence of various types of structural defects in the monolayer, is also dictated by the chemistry of the QD surface rather than by its geometry. While discussion of the assembly and structure of ordered SAMs is fundamentally interesting and relevant for many applications, it is how those structures are perturbed by the chemical and structural heterogeneity of the underlying nanoparticle surface that is relevant for preventing photo- or voltage-induced corrosion of QDs. Tightly binding fluorinated species are probably the best option for eliminating defect sites on nanoparticles, but fortunately – given the difficult syntheses, expense, and poor solubility of these molecules – effective passivation requires very small surface fractions of these molecules.

2.6 Supplementary Information

2.6.1 Synthesis and Purification of PbS

We adapted our synthesis procedure from a method originally reported by Hines and Scholes.[93] In a 50-mL three-necked round bottom flask, we added 0.36 g lead oxide (PbO, Sigma-Aldrich, 99.0%), a 20 mL solution of 1-octadecene (ODE, Sigma-Aldrich, 90%) and oleic acid (OA, Sigma-Aldrich, 90%). We utilized 1.05 mL OA and 19 mL ODE for R=1.4 nm and R=1.5 nm QDs and 3.0 mL OA and 17.0 mL ODE for R=1.7 nm. We heated the mixture to 150 °C under an N_2 atmosphere and constant N_2 bubbling for 30 minutes. We then lowered the temperature to 110 °C and injected the sulfur precursor solution. The sulfur precursor solution was prepared by dissolving 0.14 mL of bis(trimethylsilyl) sulfide in 8 mL ODE. For 1.4 nm PbS QDs, the heating mantle was removed immediately after the sulfur precursor injection. For 1.5 nm PbS QDs, the

temperature controller was turned off immediately after the injection. For 1.7 nm PbS QDs, the reaction temperature was maintained at 110 °C for 10 minutes. In all cases, the reaction solutions cooled slowly to room temperature. The QDs were purified by washing the reaction mixture with methanol (7:1 by volume) and then centrifuging it at 3500 rpm for 20 minutes. We decanted the supernatant, dried the QD pellet with N_2, and then redispersed the QDs in 5 mL of hexanes. We then repeated this washing procedure with methanol, acetone, and methanol. The QDs were dried under N_2 and redispersed in hexanes. The absorbance and photoluminescence spectra of the PbS are shown in **Figure 2.4**.

2.6.2 Size Determination of PbS QDs via Grand State Absorption and Photoluminescence (PL) Spectroscopy.

Ground state absorption spectra of solutions of PbS QDs in hexanes were collected on a Varian Cary 5000 spectrometer using a 2 mm/10 mm dual paths-length cuvette (in which we measure along the 2-mm axis of the cuvette), **Figure 2.4**. The baselines of all spectra were

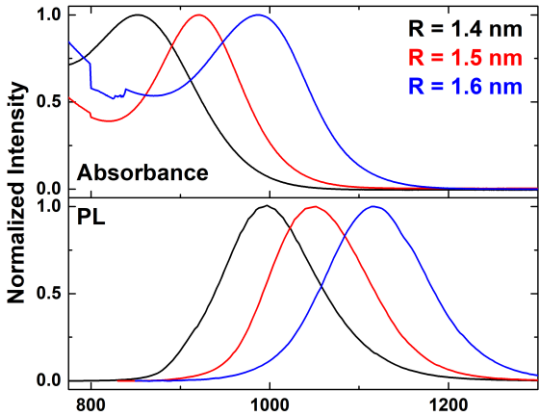

Figure 2.4. Normalized absorbance intensity (top panel) and photoluminescence intensity (bottom panel) for oleate-capped PbS QDs with radii of 1.4 nm (black), 1.5 nm (red), and 1.6 nm (blue). The discontinuities in the absorbance spectra around 800 nm are artifacts due to a grating change in the spectrometer.

corrected with neat hexanes prior to measurement. We determined the size of the QDs from the position of the first excitonic peak using a literature calibration curve.[77] The concentrations of all PbS solutions were measured from the absorbance at 400 nm. We determined the polydispersity of PbS QD solutions from the Gaussian linewidth of their PL spectra.

2.6.3 Transmission Electron Microscopy (TEM) Imaging.

All TEM images were acquired on 400 mesh holey carbon on copper TEM grids (Ted Pella) and imaged using a JEOL JEM-2100 FasTEM operated at 200 kV. Oleate-capped QD samples were prepared by drop casting a PbS QD solution in hexanes onto a TEM grid. We dried the TEM grid in the ambient atmosphere for 30 minutes and subsequently placed it into a vacuum oven at 35 ºC for one hour to remove any residual solvent. **Figure 2.5** shows representative TEM micrographs of the PbS QD samples. Analysis of the PbS with *ImageJ* software[94] yields average particle radii of 1.5 ±0.2 nm, 1.6 ± 0.2 nm, and 1.8 ± 0.2 nm for QDs with first excitonic peaks at 850 nm, 920 nm, and 990 nm, respectively. **Figure 2.6** contains the size histograms for the PbS QD samples.

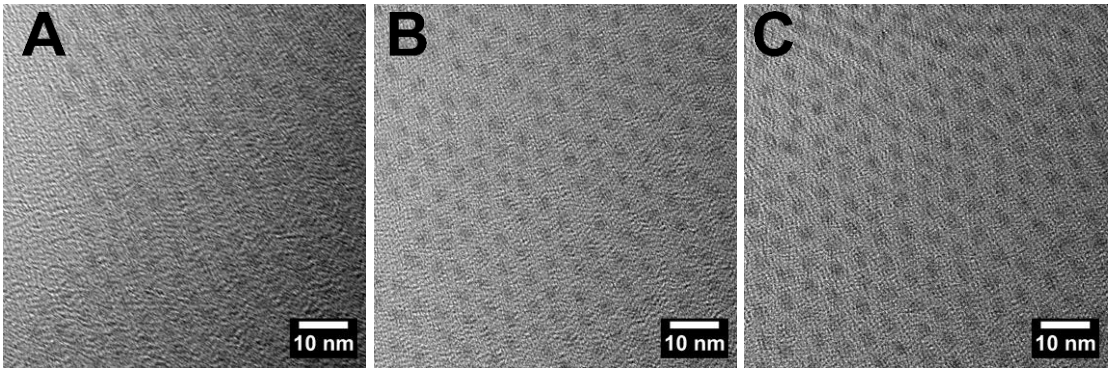

Figure 2.5. TEM micrographs of PbS QDs with first excitonic peaks at A) 850 nm, B) 920 nm, and C) 990 nm.

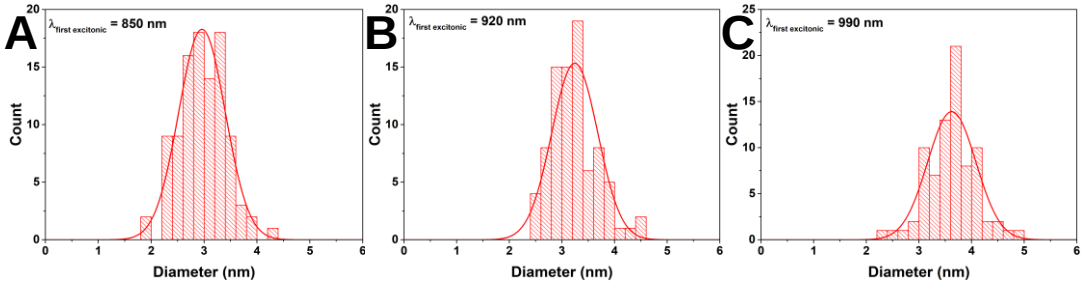

Figure 2.6 Histograms of QD diameter from QD diameter measurements in *ImageJ* for QDs with first excitonic peaks at A) 850 nm, B) 920 nm, and C) 990 nm. The radii of these QDs are 1.5 ±0.2 nm, 1.6 ± 0.2 nm, and 1.8 ± 0.2 nm, respectively.

2.6.4 Ligand Exchange of QDs and Sample Preparation for NMR Characterization and Fluorescence Quenching Experiments.

We performed exchanged portions of the oleate adlayer on PbS QDs with the following thiol molecules: 1-Dodecanethiol (DDT, Aldrich, 98%), 12,12,12-Trifluorododecane-1-thiol (F1DDT, Synquest Laboratories, 97%), and 9,9,10,10,11,11,12,12,12-Nonafluorododecane-1-thiol (F4DDT, Synquest Laboratories), 1H,1H,2H,2H,3H,3H,4H,4H-Perfluorododecaneanthiol (F8DDT, synthesis detailed below), or 1H,1H,2H,2H-Perfluorododecanethiol (F10DDT, synthesis detailed below).

We transferred 70 nanomoles of PbS QDs from the stock solution (as determined from ground state absorption spectroscopy) into a scintillation vial and removed the hexanes using a gentle flow of N_2. We then brought the QD pellet into a nitrogen glovebox and resuspended the QDs in 3.5 mL of a benzene-d_6 thiol solution. The benzene-d_6 thiol solution was prepared such that there were the appropriate equivalents of thiol molecule to accomplish the ligand exchange in

benzene-d_6 (Aldrich, 99.6%). The equivalents utilized to accomplish each ligand exchange can be found in **Tables 2.1-2.3** in section 2.2.

To prepare samples for NMR analysis, we transferred 500 μL of each QD dispersion to a scintillation flask and added 20 μL of ferrocene solution (20 mg of ferrocene (Aldrich, 98%) in 1.08 mL of benzene-d_6), and 240 μL of benzene-*d6*. NMR characterization of the sample was performed at least 12 hours after the sample was prepared. ^{19}F and ^{1}H NMR experiments were performed on an Agilent DD2 500 MHz system or a Bruker Avance III 600 MHz system.

For PL measurements, we added 500 μL of each QD dispersion into each of 5 vials. We then added 0, 25, 50, 75, 100 μL of Me_4BQ solution (49.2 mg of 2,3,5,6-Tetramethyl-1,4-benzoquinone (Me_4BQ, Aldrich 97%) to 1.36 mL of benzene-d_6), and enough benzene-d_6 to each vial to bring the volume to 760 μL. PL spectra were collected on the samples at least 12 hours after the samples were prepared, on a Horiba Fluorolog-3 spectrofluorimeter using the right-angle geometry with a 2 mm/10 mm dual path-length cuvette. We excited samples along the 2-mm axis of the cuvette. Samples of QDs with radii of 1.4 nm, 1.5 nm, or 1.6 nm were photoexcited at 765 nm, 820 nm, and 800 nm, respectively.

2.6.5 Quantification of the Composition of the Ligand Shell of QDs.

The composition of the monolayers was determined from at least 3 independently prepared samples of each type of ligand shell investigated utilizing literature procedures.[27]

Determination of Bound and Displaced Oleate after Addition of Thiolate Ligand. To determine the total number of oleates (bound + free) in each QD sample, we integrated the two olefinic protons in oleate species (centered at 7.0 ppm) relative to the ten protons in the ferrocene internal standard (4.01 ppm). We then fit the olefinic oleate protons to a sum of two Gaussian

peaks corresponding to bound and displaced oleate ligands, shown in **Figure 2.7**. We then calculated the fraction of the total oleate signal that contributed to the free and displaced peaks, and we multiplied these fractions by the total number of oleates (measured relative the ferrocene internal standard) to calculate the number of bound and displaced OA ligands.

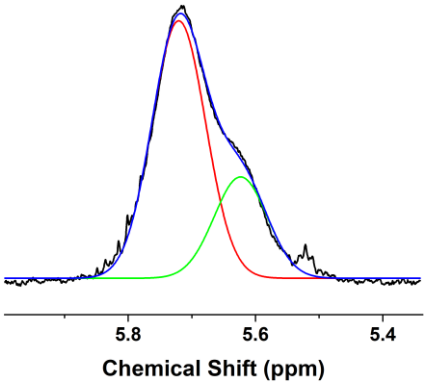

Figure 2.7. The olefinic region of a representative ^{1}H NMR spectrum of 1.5-nm PbS QDs treated with DDT. Solid lines are fits to Gaussian peaks that were utilized to quantify the number of bound and displaced OA ligands in the QD sample.

Estimation of the Number of Bound DDTs. We determined the number of bound DDT ligands indirectly by measuring the number of DDT ligands that oxidized to form didodecyl disulfide (DDDS) and assuming the rest of the DDT ligands were bound to the surface of the QD. To quantify the number of DDDS that formed, we manually baseline corrected the area of the NMR spectra around the signal for the protons alpha to the disulfide bond (2.56 ppm) using MestReNova, see **Figure 2.8**. We then integrated the signal for the protons alpha to the disulfide bond relative to the ferrocene internal standard. Since two DDT ligands oxidized to form one DDDS, we know the number of DDT ligands that were not bound is twice the number of DDDS molecules formed. We then subtracted the number of DDT that that reacted to form DDDS from the total number of

DDT ligands that we added to the sample to estimate the number of DDT ligands on the surface of the QD.

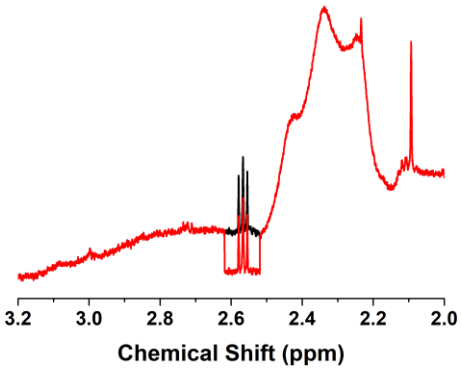

Figure 2.8. Representative ^{1}H NMR spectrum of 1.6-nm PbS QDs treated with DDT including a signal from didodecyl disulfide, the oxidation product of DDT, at 2.56 ppm before (black) and after (red) manually setting the baseline in MestReNova.

Estimation of the Bound Fluorinated Alkylthiolate Ligands. We verified that the integrated intensity of the terminal CF_3 signal from F1DDT, F4DDT, F8DDT, and F10DDT does not change (relative to an internal standard, 2-fluorobiphenyl) in the presence of QDs. We then collected ^{19}F NMR spectra of PbS QDS treated with F1DDT, F4DDT, F8DDT, and F10DDT (the number of equivalents used for each exchange can be found in **Tables 2.1-2.3**). We fit the terminal CF_3 signal to a sum of Lorentzian functions (four for F1DDT, F4DDT, and F10DDT; five for F8DDT) in which the narrow signals correspond to the nuclei from ligands that are primarily free in solution and the broadened peaks correspond to nuclei with ligands bound to the surface, see **Figure 2.9**. We then calculated the fraction of total signal that correspond to free ligands and bound ligands. We multiplied the fractions by the number of equivalents of added ligands to determine the number of free and bound fluorinated ligands.

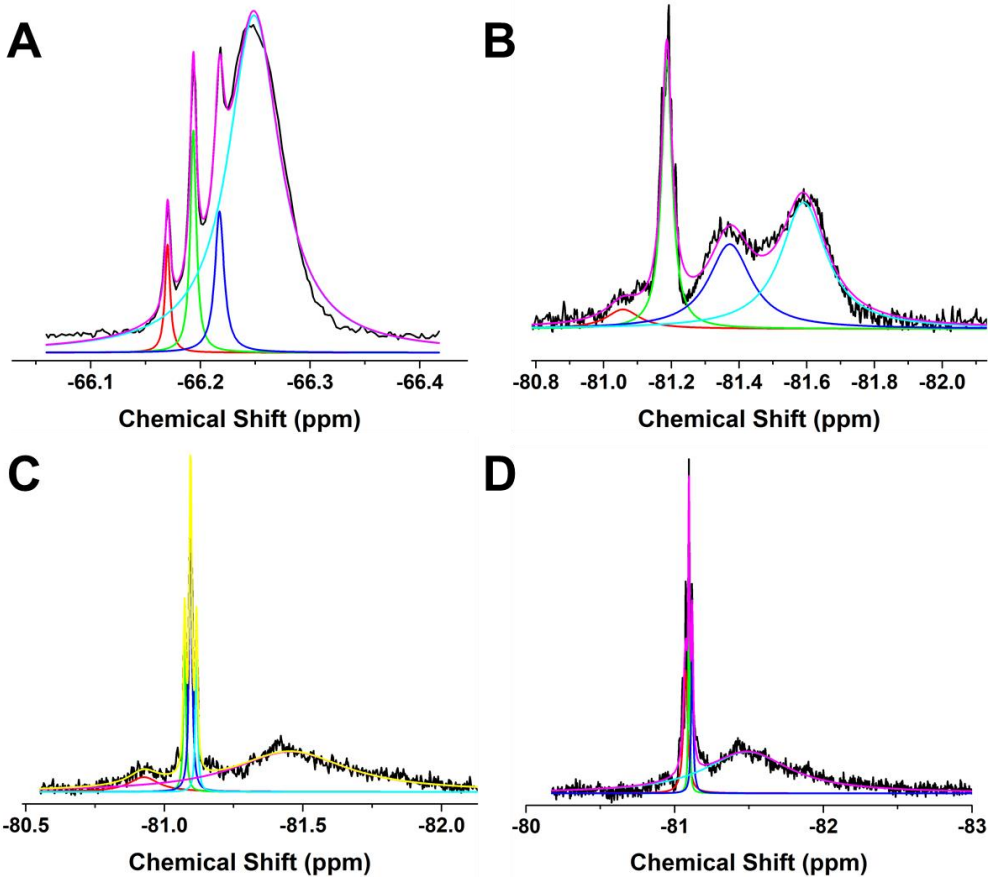

Figure 2.9. Representative ^{19}F NMR spectra of 1.5-nm PbS QDs treated with (A) F1DDT, (B) F4DDT, (C) F8DDT, and (D) F10DDT. Solid lines are fits to Lorentzian peaks that were utilized to quantify the number of bound and displaced OA ligands in the QD sample.

2.6.6 Investigating the Chemical Shift of Displaced Oleate Ligands.

To better visualize the chemical shift of the displace oleate ligands, we subtracted the ^{1}H NMR spectra of QDs capped with solely OA (normalized to a ferrocene internal standard) from the 1H NMR spectra of QDs with mixed monolayers of one of the thiolates and OA (normalized to a ferrocene internal standard). The difference spectra enable us to visualize the depletion of the bound OA ligands and the presence of the displaced ligands. In **Figure 2.10**, we show the NMR spectra for all three sizes of QDs with only OA ligands, after treatment with DDT, as well as, the

difference spectra. The upfield chemical shift of the displaced OA from 1.6-nm QDs compared to the displaced OA from 1.4-nm and 1.5-nm QDs, in **Figure 2.10**, indicates that displaced ligands from the 1.6-nm QDs spend less time bound to the surface of QD.[85]

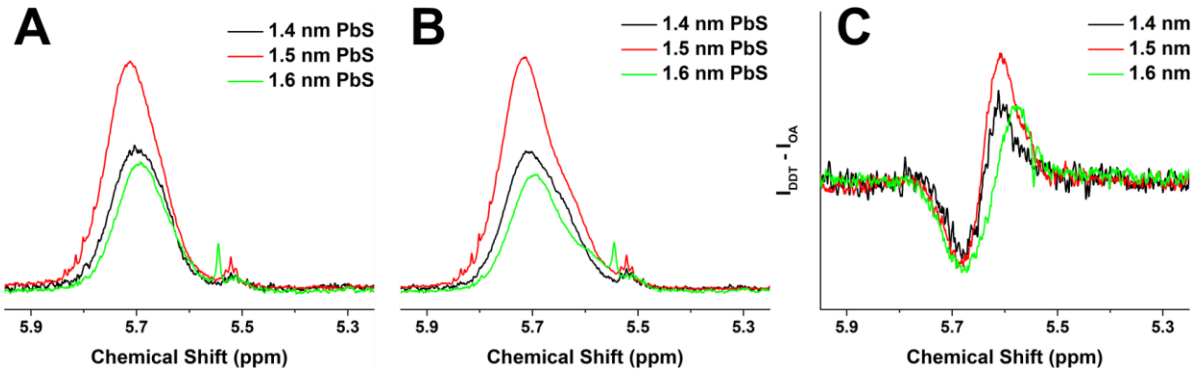

Figure 2.10. The olefinic region of ^{1}H NMR spectra of PbS QDs (A) before ligand exchange and (B) after treatment with DDT. Difference spectra (C) were generated by subtracting the spectra of QDs with only OA ligands from the spectra of QDs of the same size with mixed monolayers of OA/DDT. The negative features in the difference spectra correspond to the depletion of bound OA ligands, and the positive features correspond to the formation of displaced OA ligands. All spectra have been normalized using the intensity of a ferrocene internal standard.

2.6.7 Synthesis of F8DDT and F10DDT.

F10DDT was synthesized according a previously reported literature procedure.[78] NMR spectra were collected on a 400 MHz Agilent DD MR-400 system. ^{1}H NMR (400MHz, Chloroform-*d*) δ 2.76 (m, 2H), δ 2.42 (m, 2H), δ 1.60 (t, *J*=8.3 Hz, 1H). ^{19}F NMR (400MHz, Chloroform-*d*) δ -80.75 (t, *J*=10.1 Hz, 3F), δ -114.35 (m, 2F), δ -121.80 (m, 10F), δ -122.69 (m, 2F), δ -123.52 (m, 2F), δ -126.10 (m, 2F).

F8DDT was synthesized according to the same procedure, but starting with 1-Iodo-4-(perfluorooctyl)butane (F8I, Synquest Laboratories, 97%). A 50 mL three-neck flask was charged 15 mL of anhydrous reagent alcohol, 0.5 mL of sodium methoxide (2.2 mmol Sigma Aldrich, 25

wt. % in methanol), 0.22 mL thiolacetic acid (3.0 mmol, Sigma Aldrich, 97%) and 0.89 g F8I (1.5 mmol). The reaction solution was heated under N_2 at 70 °C for 16 hours and then cooled to room temperature. Ether was then added, and the organic layer was separated. The organic layer was washed three times with hot, saturated NaCl solution. The organic layer was dried over anhydrous, magnesium sulfate. The ether was removed under reduced pressure. The residue was suspended in 15 mL of anhydrous reagent alcohol. 0.14 g KOH (1.5 equivalents) dissolved in a minimal amount of water was added dropwise. The reaction mixture quickly turned orange, and reaction mixture was then heated at reflux for 12 hours. The reaction mixture was poured over 20 mL of ice cold, 2M HCl solution. The reaction mixture turned yellow. Ether was added, and the organic layer was separated and subsequently washed 3 times with saturated NaCl solution. The organic layer was dried over anhydrous, magnesium sulfate, and the ether was removed under reduced pressure. The product was purified using a silica gel plug and ethyl acetate. The ethyl acetate was removed under reduced pressure, resulting in a pale yellow solid. ^{1}H NMR (400MHz, Chloroform-*d*) δ 2.56 (dt, *J*=7.9 Hz, 6.4 Hz, 2H), δ 2.07 (m, 2H), δ 1.71 (m, 4H), δ 1.36 (t, *J*=7.9 Hz, 1H). ^{19}F NMR (400MHz, Chloroform-*d*) δ -80.78 (t, *J*=10.5 Hz, 3F), δ -114.36 (q, *J*=15.8 Hz, 2F), δ -121.84 (m, 6F), δ -122.73 (m, 2F), δ -123.51 (m, 2F), δ -126.11 (m, 2F).

2.6.8 Elemental Analysis of QDs.

We quantified the ratio of Pb to S (Pb:S) with ICP-OES of acid digested samples. Specifically, dried samples were digested in concentrated trace nitric acid (> 69%, Thermo Fisher Scientific, Waltham, MA, USA) and placed at 60 °C for at least 3 hours to allow for complete sample digestion. Ultra-pure H_2O (18.2 MΩ·cm) was added to produce a final solution of 3.0% nitric acid (v/v) in a total sample volume of 10 mL. Quantitative standards consisting of 1000, 500, 250, 125,

62.5, and 31.25 ng/g were made using a 10 µg/mL multi-element standard (IV-ICPMS-71A from Inorganic Ventures, Christiansburg, VA, USA) in 3.0% nitric acid (v/v) in a total sample volume of 5 mL.

ICP-OES was performed on a computer-controlled (QTEGRA software) Thermo iCap7600 ICP-OES (Thermo Fisher Scientific, Waltham, MA, USA) operating in axial view and equipped with a CETAC 520 autosampler (Omaha, NE, USA). Each sample was acquired using 5 second visible exposure time and 15 second UV exposure time, running 3 replicates. The spectral lines selected for analysis were S (180.731 nm) and Pb (220.353, 216.999, 182.205, 283.306 nm).

2.6.9 2.4.8 Transient Absorption Spectroscopy of PbS QDs to Determine τ_0.

Our nanosecond-microsecond transient absorption spectrometer is described in detail elsewhere.[37] Transient absorption measurements were collected in 2 mm glass cuvettes, while being stirred. In order to avoid the contribution of multiple exciton dynamics, the expectation value of excitons per QD was adjusted to be less than or equal to <0.3> for all ultrafast experiments.

We monitored the dynamics of ground state bleach recovery on the nanosecond-to-microsecond timescale for PbS QDs. We use **eq 2.3**, a sum of exponential functions convoluted

$$y = IRF \otimes \sum_1^n A_n e^{\frac{-(t-t_0)}{\tau_n}} \quad (2.3)$$

with an instrument response function (a Gaussian pulse) to fit all the kinetic traces extracted from TA datasets. We chose *n* to be the minimum integer to obtain a satisfactory fit, which we define as a fit that has symmetric residuals around the zero line at all delay times. We averaged the excitonic lifetimes of the QDs for all of the mixed oleate/thiolate ligand layers. **Table 2.4** contains the excitonic lifetimes of the QDs with each monolayer in the absence of Me_4BQ.

Table 2.4. Excitonic Lifetime of PbS QD Samples.

Sample	τ_0 (μs)
1.4-nm QDs with OA only	2.0 ± 0.2
1.4-nm QDs with OA/thiolate	1.97 ± 0.03
1.5-nm QDs with OA only	2.53 ± 0.05
1.5-nm QDs with OA/thiolate	2.37 ± 0.05
1.6-nm QDs with OA only	2.17 ± 0.03
1.6-nm QDs with OA/thiolate	2.18 ± 0.07

2.6.10 Determining the Diffusion-Limited Collision Frequency.

We calculated the diffusion-limited collision frequency, k_0, according **eq 2.4**.[40] In **eq 2.4,**

$$k_0 = \frac{4\pi N_A}{1000} R_C D_{Me_4BQ} \tag{2.4}$$

D_{Me_4BQ} is the diffusion constant of Me_4BQ in benzene-d_6 and R_C is the radius of collision. We define R_C as the sum of the hydrodynamic radii of the QD and the freely diffusing Me_4BQ molecule. We measured D_{Me_4BQ} *via* diffusion-ordered spectroscopy (DOSY) and calculated the hydrodynamic radii of the QD and Me_4BQ using the Stokes-Einstein equation, as explained below.

2.6.11 Diffusion-Ordered Spectroscopy (DOSY) NMR.

We recorded DOSY spectra of solutions of 32.9 μM PbS QDs with the appropriate number of thiolate ligands in benzene-d_6 and Me_4BQ on an Agilent DD2 600 MHz system using a double stimulated echo experiment with bipolar gradients ("dbppste_cc" sequence). We used a diffusion delay, Δ, of 0.1 s, and a gradient length, δ, of 6000 μs (PbS QDs) or 2000 μs (Me_4BQ). We chose 16 gradient strengths from 655 s/cm to 16,000 s/cm for PbS QD samples. For Me_4BQ samples, we chose 32 gradient strength values from 2% to 95%.

We plotted the dependence of the total integrated ^{1}H signal of the PbS QD samples (vinyl oleate protons, 5.69 ppm) and Me_4BQ (methyl protons, 1.51 ppm) as function of the gradient function, G^2, given by **eq 2.5** (**Figure 2.11**):

$$G^2 = (\gamma g \delta)^2 \left(\Delta - \frac{\delta}{3}\right) \tag{2.5}$$

Where γ is the gyromagnetic ratio of a proton (2.68×10^4 $s^{-1}G^{-1}$), g is the gradient strength (G/cm), δ is the length of the gradient pulse, and Δ is the diffusion delay. We then fit the curve curves to **eq 2.6**,

$$I(G^2) = I_0 e^{-DG^2} \tag{2.6}$$

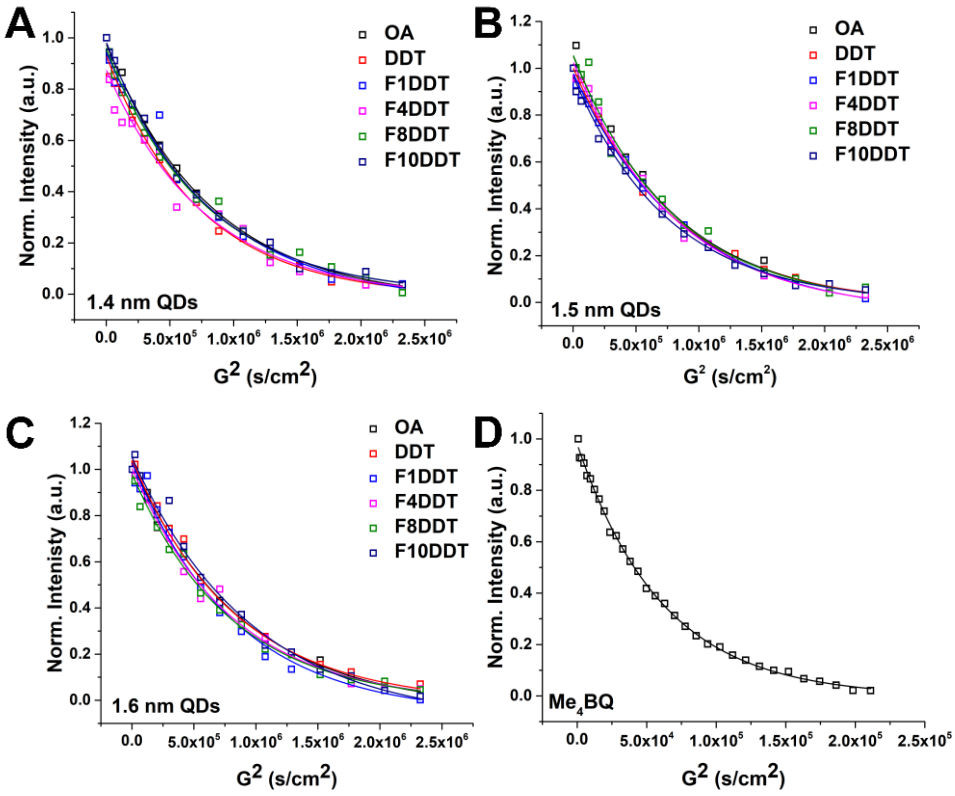

Figure 2.11. Plots of signal attenuation as a function of G^2 for **A)** 1.4-nm PbS QDs, **B)** 1.5-nm PbS QDs, **C)** 1.6-nm PbS QDs, and **D)** Me_4BQ. The solid lines are best fit functions to **eq 2.6**.

We then used the Stokes-Einstein equation (**eq 2.7**) to calculate the hydrodynamic radii.

$$r = \frac{k_B T}{6\pi\eta D_s} \quad (2.7)$$

In **eq 2.7**, r is the hydrodynamic radius, k_B is the Boltzmann constant, T is the temperature (298 K), η is 0.59 mPa·s, the viscosity of benzene-d_6, and D_s is the diffusion coefficient (the inverse of D from **eq 2.6**). The diffusion coefficients and hydrodynamic radii can be found in **Table 2.5**.

Table 2.5. DOSY Parameters for Me_4BQ and PbS QDs.

	D (cm^2/s)	**r (nm)**
1.4-nm PbS OA	$(1.22\pm 0.06)\times10^{-6}$	3.0±0.2
1.4-nm PbS + DDT	$(1.4\pm 0.1)\times10^{-6}$	2.7±0.2
1.4-nm PbS + F1DDT	$(1.4\pm 0.2)\times10^{-6}$	2.6±0.3
1.4-nm PbS + F4DDT	$(1.3\pm 0.2)\times10^{-6}$	2.9±0.5
1.4-nm PbS + F8DDT	$(1.32\pm 0.07)\times10^{-6}$	2.8±0.2
1.4-nm PbS + F10DDT	$(1.4\pm 0.2)\times10^{-6}$	2.8±0.2
1.5-nm PbS OA	$(1.3\pm 0.1)\times10^{-6}$	2.9±0.2
1.5-nm PbS + DDT	$(1.24\pm 0.06)\times10^{-6}$	3.0±0.2
1.5-nm PbS + F1DDT	$(1.14\pm 0.04)\times10^{-6}$	3.3±0.1
1.5-nm PbS + F4DDT	$(1.21\pm 0.08)\times10^{-6}$	3.0±0.2
1.5-nm PbS + F8DDT	$(1.3\pm 0.02)\times10^{-6}$	2.9±0.4
1.5-nm PbS + F10DDT	$(1.3\pm 0.01)\times10^{-6}$	2.8±0.2
1.6-nm PbS OA	$(1.14\pm 0.08)\times10^{-6}$	3.2±0.2
1.6-nm PbS + DDT	$(1.2\pm 0.1)\times10^{-6}$	3.0±0.2
1.6-nm PbS + F1DDT	$(1.2\pm 0.1)\times10^{-6}$	3.1±0.3
1.6-nm PbS + F4DDT	$(1.2\pm 0.1)\times10^{-6}$	3.1±0.3
1.6-nm PbS + F8DDT	$(1.0\pm 0.1)\times10^{-6}$	3.6±0.4
1.6-nm PbS + F10DDT	$(1.2\pm 0.1)\times10^{-6}$	3.0±0.3
Me_4BQ	$(1.6\pm 0.2)\times10^{-5}$	0.23±0.02

Table 2.6. Collisional Quenching Efficiencies for Me_4BQ/PbS QD Mixtures.

	$\Phi_{collision}$	Reference Used to calculate $\frac{\Phi}{\Phi_{OA}}$ [a]
1.4-nm PbS OA (*ref A)*	0.36 ± 0.04 %	1.4-nm PbS OA (*ref A)*
1.4-nm PbS OA (*ref B)*	0.34 ± 0.04 %	1.4-nm PbS OA (*ref B)*
1.4-nm PbS OA (*ref C)*	0.39 ± 0.04 %	1.4-nm PbS OA (*ref C)*
1.4-nm PbS OA (*ref D)*	0.37 ± 0.04 %	1.4-nm PbS OA (*ref D)*
1.4-nm PbS + DDT	0.23 ± 0.02 %	1.4-nm PbS OA (*ref A)*
1.4-nm PbS + F1DDT	0.24 ± 0.03 %	1.4-nm PbS OA (*ref B)*
1.4-nm PbS + F4DDT	0.18 ± 0.02 %	1.4-nm PbS OA (*ref B)*
1.4-nm PbS + F8DDT	0.16 ± 0.02 %	1.4-nm PbS OA (*ref C)*
1.4-nm PbS + F10DDT	0.14 ± 0.01%	1.4-nm PbS OA (*ref D)*
1.5-nm PbS OA (*ref A)*	0.21 ± 0.02 %	1.5-nm PbS OA (*ref A)*
1.5-nm PbS OA (*ref B)*	0.19 ± 0.02 %	1.5-nm PbS OA (*ref B)*
1.5-nm PbS OA (*ref C)*	0.20 ± 0.02 %	1.5-nm PbS OA (*ref C)*
1.5-nm PbS + DDT	0.135 ± 0.007 %	1.5-nm PbS OA (*ref A)*
1.5-nm PbS + F1DDT	0.119 ± 0.005 %	1.5-nm PbS OA (*ref B)*
1.5-nm PbS + F4DDT	0.110 ± 0.007 %	1.5-nm PbS OA (*ref B)*
1.5-nm PbS + F8DDT	0.070 ± 0.009%	1.5-nm PbS OA (*ref C)*
1.5-nm PbS + F10DDT	0.065 ± 0.009 %	1.5-nm PbS OA (*ref C)*
1.6-nm PbS OA (*ref A)*	0.25 ± 0.02 %	1.6-nm PbS OA (*ref A)*
1.6-nm PbS OA (*ref B)*	0.30 ± 0.02 %	1.6-nm PbS OA (*ref B)*
1.6-nm PbS OA (*ref C)*	0.26 ± 0.02 %	1.6-nm PbS OA (*ref C)*
1.6-nm PbS OA (*ref D)*	0.29 ±0.02 %	1.6-nm PbS OA (*ref D)*
1.6-nm PbS + DDT	0.15 ± 0.02 %	1.6-nm PbS OA (*ref A)*
1.6-nm PbS + F1DDT	0.16 ± 0.02 %	1.6-nm PbS OA (*ref B)*
1.6-nm PbS + F4DDT	0.11 ± 0.01 %	1.6-nm PbS OA (*ref C)*
1.6-nm PbS + F8DDT	0.047 ± 0.006 %	1.6-nm PbS OA (*ref D)*
1.6-nm PbS + F10DDT	0.057 ± 0.005 %	1.6-nm PbS OA (*ref D)*

[a]To account for the day to day variation of the permeability of the native, oleate ligand shell, we measured the permeability of OA and OA/thiolate ligand shell on the same day. We then used the oleate sample we compared the permeability of a OA/thiolate ligand shell to the OA ligand shell that was measured the same day to calculate $\frac{\Phi}{\Phi_0}$.

2.6.12 DFT-based Geometry Optimization of Ligands.

Quantum chemical calculations were performed at the density functional theory (DFT) level using Nwchem 6.5 software.[95] Geometries were optimized using the hybrid PBE0 functional with the 6-31++G** basis set for all atoms. Calculations were performed using the Conductor-like

Screening Model (COSMO) to account for solvent interactions where the solvent (benzene) is approximated as a dielectric continuum.[96] We performed geometry optimization on F10DDT, F4DDT, F1DDT, DDT, and OA using above procedure. The final optimized geometries are shown in **Figure 2.12**. Similarly, the electron density for each molecule was obtained using DFT.

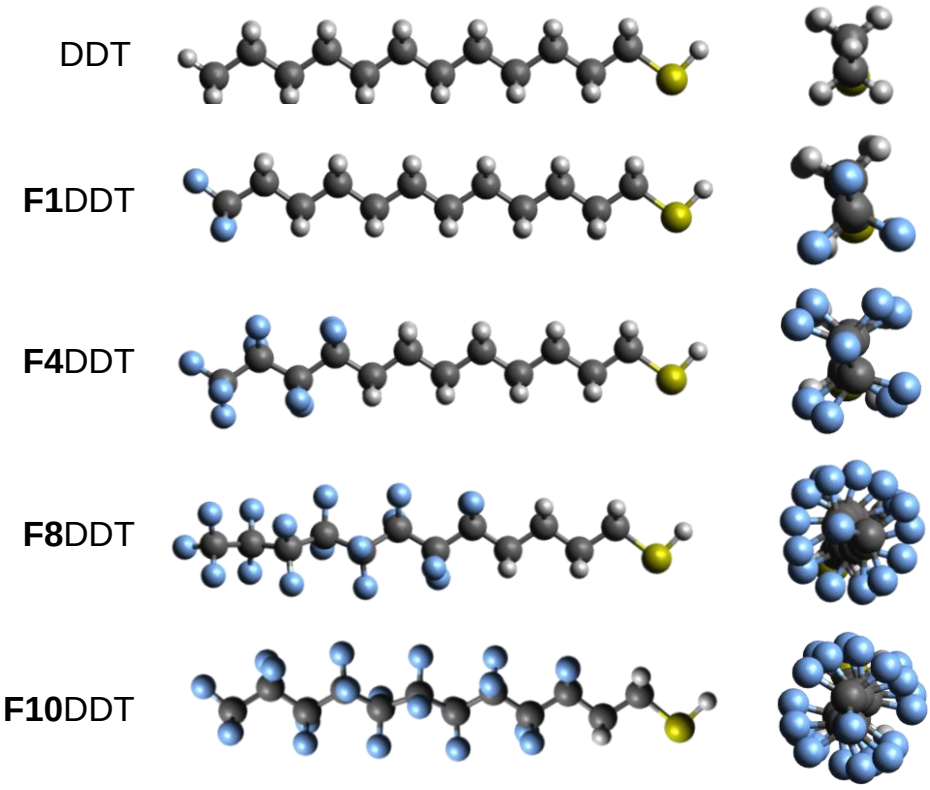

Figure 2.12. Size-on view (left column) and front-on view (right column) of DFT-optimized structures of the alkylthiolate and partially fluorinated alkylthiolate ligands.

2.6.13 Estimation of Molecular Diameter of DDT and F10DDT.

Electron density maps of DDT and F10DDT were visualized using VESTA[97] at an isovalue of 0.01. The thickness of the electron density, the "molecular diameter" was estimated as shown in **Figure 2.13**.

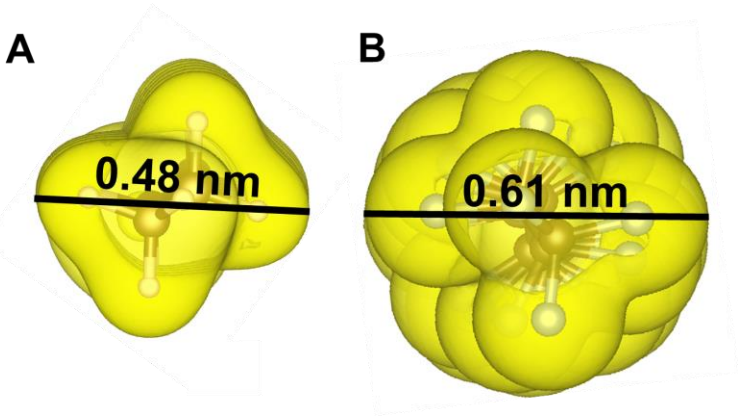

Figure 2.13. Electron density map of **A)** DDT and **B**) F10DDT, generated at an isovalue of 0.01.

2.6.14 Work of Adhesion of a Film of 1.6-nm PbS QDs and Acetonitrile.

Advancing contact angle measurements were collected using VCA Optima XE – video contact angle system. Films of 1.6-nm QDs were prepared by spin coating QD solutions in hexanes onto plasma-cleaned glass. Two films were prepared for each QD/ligand shell combination. The films were dried in a vacuum oven at 35 °C for 30 minutes before contact angle measurements were collected. We used acetonitrile as our contacting liquid. Three advancing contact angle measurements were taken on each film. The contact angle measurements were averaged for each QD/ligand shell combination. The work of adhesion between the films and the droplet of acetonitrile were calculated according the Young-Dupré equation, **eq 2.8**. In **eq 2.8**, W is the work of adhesion, γ_{LV} is the free energy of

$$W = \gamma_{LV}(1 + \cos\theta_a) \qquad (2.8)$$

the liquid- vapor interface, and θ_a is the measured contact angle. For ACN, γ_{LV} is 27.0 mJ·m^{-2}.[98] **Figure 2.14** is a plot of the W as a function of the number of fluorinated carbons in each thiolate ligand.

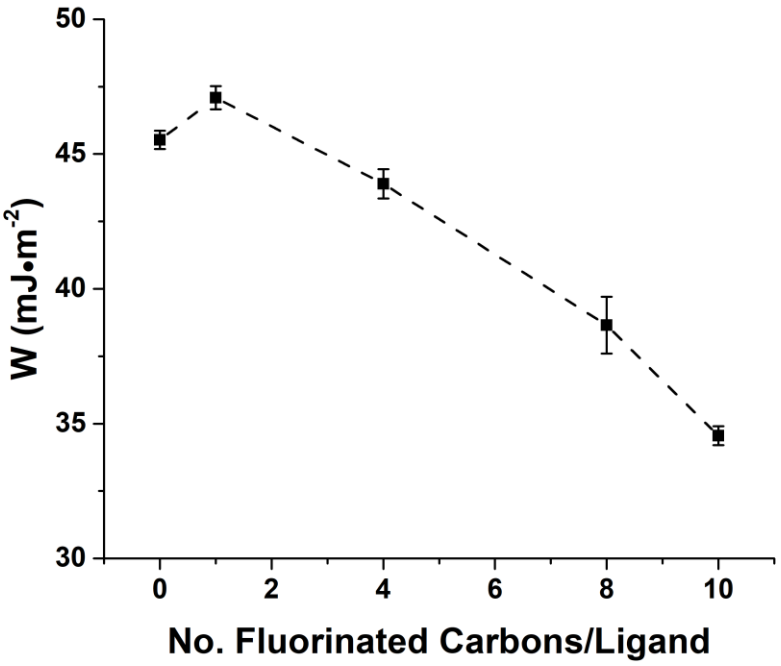

Figure 2.14. Plot of the work of adhesion, *W*, of a series of films of 1.6-nm QDs spin-coated onto glass. W is calculated from the advancing contact angle of a drop of ACN on the QD film based on **eq. 2.8**.

Chapter 3. Quantum Dot-Catalyzed Photoreductive Removal of Sulfonyl-Based Protecting Groups

Adapted From: **Perez, K.A.**, Rogers, C.C., Weiss, E. A. Quantum Dot-Catalyzed Photoreductive Removal of Sulfonyl-Based Protecting Groups, *Angew. Chem.*, doi:10.1002/anie.202005074.

3.1 Chapter Summary

This chapter describes the use of $CuInS_2$/ZnS quantum dots (QDs) as photocatalysts for the reductive deprotection of aryl sulfonyl-protected phenols. For a series of aryl sulfonates with electron-withdrawing substituents, the rate of deprotection for the corresponding phenyl aryl sulfonates increases with decreasing electrochemical potential for the two electron transfers within the catalytic cycle. The rate of deprotection for a substrate that contains a carboxylic acid, a known QD-binding group, is accelerated by more than a factor of ten from that expected from the electrochemical potential for the transformation, a result that suggests that formation of metastable electron donor-acceptor complexes provides a significant kinetic advantage. This deprotection method does not perturb the common NHBoc or toluenesulfonyl protecting groups and, as demonstrated with an estrone substrate, does not perturb proximate ketones, which are generally vulnerable to many chemical reduction methods used for this class of reactions.

3.2 Deprotection of Sulfonyl Protected Phenols

Sulfonyls are viable protecting groups for phenols, because, unlike alkylsulfonates, phenylsulfonates are stable to nucleophilic attack. Sulfonyl protection strategies for phenols are perhaps not as widely used as they could be, however, because the deprotection requires harsh conditions. Electrochemical cleavage of the S-O bond of a sulfonyl protected phenol requires reduction with a potential of at least -1.4 V *vs*. SCE,[99-100] and thermal deprotection reactions employ strong acids (H_2SO_4) or strong reducing agents (Na, Li or Mg) that are incompatible with substituents or other protecting groups on the phenol.[101] Given that these deprotection reactions have been accomplished *via* electrochemical deprotection[99, 102] and direct photolysis,[103-104] and that

visible-spectrum photons have energies ranging from 3.10 eV (400 nm) to 1.77 eV (700 nm), the deprotection of sulfonated phenols is a good candidate reaction for a photoredox approach.

In the photoreductive deprotection, a photosensitizer absorbs two successive photons, donates two electrons in sequence to liberate a phenol and the corresponding sulfinate anion from the protected species, and donates two holes to a sacrificial terminal reductant. Unlike direct photolysis, photoredox catalysis does not require that a substrate be directly photoexcited, so UV light-driven undesirable side reactions are minimized.[105] For more than 30 years,[106-107] photoredox strategies using organic dyes and ruthenium- and iridium-based complexes as photocatalysts have enabled deprotection of, for example, *para*-methoxybenzyl protected alcohols[108] and amides,[109] 4-methoxybenzyl protected primary amines and alcohols,[110] and *N*-tosyl amides.[106, 111-112] This strategy has not been demonstrated for sulfonyl protected phenols, however, possibly because the only commercially available inorganic complexes with excited-state oxidation potentials greater than -1.4 V *vs.* SCE are *fac*-$Ir(ppy)_3$, *fac*-$Ir(dF\text{-}ppy)_3$, and $[Ir(ppy)_2(dtbbpy)]^+$, all of which have peak absorption at wavelengths shorter than 400 nm.[113] Photons with energy above 400 nm often directly photoexcite the substrate (in addition to the photosensitizer) and thereby enable parasitic reactions. Recently, colloidal semiconductor quantum dots have been investigated as visible-light-absorbing photoredox catalysts for organic transformations.[56, 114-115]

3.3 QD-photocatalyzed deprotection of sulfonyl protected phenols

This chapter describes the photocatalytic reductive deprotection of a series of aryl sulfonyl-protected phenols using copper indium sulfide/zinc sulfide core/shell quantum dots ($CuInS_2$/ZnS QDs) as light harvesters and photo-redox catalysts. $CuInS_2$/ZnS QDs have high excited-state oxidation potentials, >-1.9 V *vs*. SCE, and excited-state lifetimes of ~30-500 ns.[46, 49, 116] While, as

mentioned above, these QDs are not unique in their ability to catalyze this class of reaction, we highlight in this report two advantages of using $CuInS_2$/ZnS QDs for photocatalyzed deprotections: (i) their size can be tuned to absorb photons as low-energy as 730 nm (we use 532-nm illumination in this study),[46, 117] whereas the Ir compounds require blue or UV light, and (ii) while photoredox reactions catalyzed by molecules require diffusion-limited collisions between substrates and excited-state catalysts, we can design QDs to reversibly associate with suitably functionalized or charged substrates.[57] Formation of metastable complexes of photocatalyst and substrate is beneficial for increasing the yield of photoredox reactions, because this association increases the probability of electron transfer to the substrate or intermediate upon photoexcitation of the catalyst.[48, 58]

Figure 3.1 summarizes our proposed photocatalytic cycle for the 2-e$^-$ deprotection of phenyl aryl sulfonates. $CuInS_2$/ZnS QDs, synthesized using an adapted literature procedure[46] and

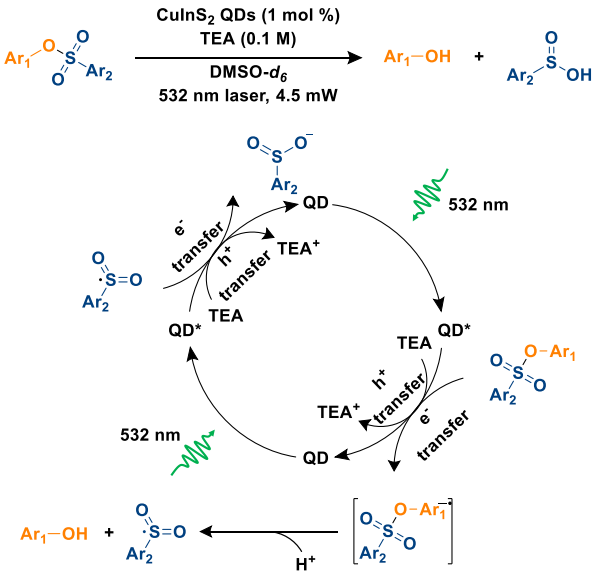

Figure 3.1. Reaction conditions and proposed catalytic cycle for the photocatalyzed 2-e$^-$ deprotection of aryl sulfonates by $CuInS_2$/ZnS QDs. Ar_1 and Ar_2 are aryl groups on the protected alcohol and the protecting group, respectively, see **Table 3.1**. Sacrificial triethylammonium (TEA^+) decomposes into diethyl amine and acetaldehyde, see **Figure 3.4** of the section 3.7.

solubilized in DMSO-d_6 with a 3-mercapto-1-propanol ligand shell (details in section 3.7), are photoexcited by a 532-nm photon to form QD*. QD* then transfers one electron to the substrate and one hole to the sacrificial reductant, triethylamine (TEA), to return to its ground state. The S-O bond in the singly reduced substrate breaks to form a phenoxide ion, which is protonated to form phenol, and a sulfonyl radical. The QD is then excited a second time to form QD*, whereupon QD* transfers a hole to TEA and an electron to the sulfonyl radical to form a sulfinate anion.

We synthesized a series of phenyl aryl sulfonates, **Table 3.1**, using adapted literature procedures (see section 3.7),[118-121] and measured the potential necessary to liberate phenol from each phenyl aryl sulfonate substrate from the potential corresponding to the peak of the irreversible cathodic wave in its cyclic voltammogram (CV), $E_{p,c}$, **Table 3.1** and section 3.7. The reductive wave at $E_{p,c}$ is irreversible for every substrate in the presence of our sacrificial reductant, TEA, and there are no other reductive waves at potentials lower than the reduction potential of the QDs, $E_{red,QD}$, of ~-1.9 V *vs.* SCE (see section 3.7),[49] so we conclude that the wave includes both electrons within the catalytic cycle in **Figure 3.1**.

Table 3.1 lists the ^{1}H NMR-determined yields of phenol product and % conversions of substrates **1 - 11** for the QD-photocatalyzed deprotection reactions, after 48 hours of illumination with a 4.5-mW, 532-nm laser diode. All NMR spectra are in section 3.7. For substrates where $E_{p,c} > E_{red,QD}$ (substrates **1**-**5**), the yield of the deprotection is zero. For substrates where $E_{p,c} < E_{red,QD}$ (substrates **6**-**11**), the yield generally increases as $E_{p,c}$ decreases, with the exception of substrate **6**, discussed below. The deprotection of **6**-**11** proceeds cleanly to produce phenol, as indicated by the close agreement between % conversion and % yield.

Table 3.1. $CuInS_2$/ZnS QD-Catalyzed Deprotection of Phenyl Aryl Sulfonates.

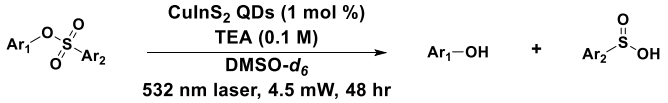

Substrate	Ar_1	Ar_2	$E_{p,c}[S/S^{2-}]$ (V *vs.* SCE)[a]	% Conversion[b]	% Yield[b]
1		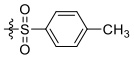	-2.20	0	0
2			-2.20	0	0
3		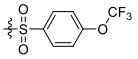	-2.09	0	0
4			-2.02	0	0
5		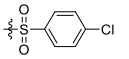	-2.00	0	0
6		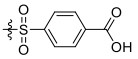	-1.81	100	92
7		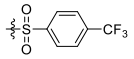	-1.72	57	57
8			-1.72	78	78
9		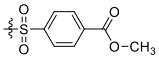	-1.55	100	91
10		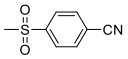	-1.48	87	83
11		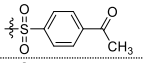	-1.44	100	93
12	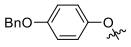	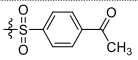	-1.50	69[c,d]	54[c,d]
13	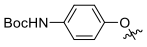	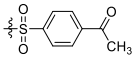	-1.49	43[c,d]	43[c,d]
14	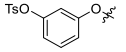	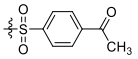	-1.48	100[c]	93[c]
15	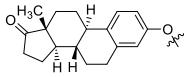	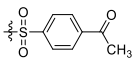	-1.46	100[c]	85[e]
16	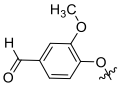	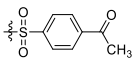	-1.45	98[c]	0[c]

[a]The potentials at which we observed peak cathodic current ($E_{p,c}$) were determined from CVs of 10 mM of the protected substrate under N_2 with 100 mM tetrabutylammonium hexafluorophosphate, and 1 M TEA in DMSO, using a glassy carbon working electrode, a Ag wire reference electrode, and a Pt wire counter electrode. The potentials are referenced to SCE using a decamethylferrocene internal standard. The notation "$E_{p,c}[S/S^{2-}]$" indicates that two electrons are transferred during the wave, one to the substrate and one to the liberated sulfonyl radical after S-O bond cleavage. [b]The conversions and yields listed are NMR yields for samples of 10 μM $CuInS_2$/ZnS QDs, 0.001 M substrate, and 0.1 M TEA in DMSO-d_6 illuminated with a 4.5-mW, 532-nm laser diode for 48 hours. [c]Yield and conversion determined after 24 hours. [d]The reaction stopped progressing after 24 hours even though starting material was still present. [e] Isolated yield for sample of 0.22 mM $CuInS_2$/ZnS QDs, 0.022 M substrate, 2.2 M TEA in DMSO-d_6 illuminated with a 4.5-mW 532-nm laser diode for 24 hours.

We confirmed that both electrons required to accomplish the sulfonate deprotection reaction originate from the QD (as opposed to TEA, which can act as a hydride donor), by performing the deprotection of **11** using 1000 equiv 5,10-dihydro-5,10-dimethylphenazine (DMPZ) as a sacrificial reductant instead of 1000 equiv TEA.[122] The yield of the reaction (after illumination with 532-nm light for 2 hours) is 20% lower with DMPZ than with TEA, probably because DMPZ is larger and has a lower probability of extracting the hole from the QD, but the deprotection clearly does not require a hydride donor to occur. This result substantiates the mechanism we proposed in **Figure 3.1**.

3.4 Kinetics of QD-photocatalyzed deprotection of sulfonyl protected phenols

Figure 3.2A shows the kinetics of the deprotection reactions for substrates **6-11.** The QDs do not precipitate or etch over the course of these reactions (see section 3.7). We determined the initial rate of each reaction from fits to these kinetic traces in the linear regime and plotted these initial rates versus $E_{p,c}$ in **Figure 3.2B.** The initial rate of the deprotection reaction generally increases as $E_{p,c}$ decreases. We also observe a positive correlation between the initial rate of the reaction and the level at which % yield ([phenol]) plateaus (see section 3.7). We suspect the plateau is caused by competition for catalytic sites between substrates and liberated sulfinate anions (*i.e.* given ample time, sulfinate ions will bind to QD surface and block catalytic sites).

As is clear from inspection of **Figure 3.2B**, the initial rate of deprotection of **6** is enhanced by more than a factor of ten from that expected from its $E_{p,c}$ value. A direct comparison of the rate constant for deprotection of **6** with that of the corresponding ester **9**, which has a lower reduction potential than **6** (by 0.26 V) leads to the tentative conclusion that the ability of **6** to associate with the surface of the QD through its carboxylate group provides a kinetic advantage in this reaction.

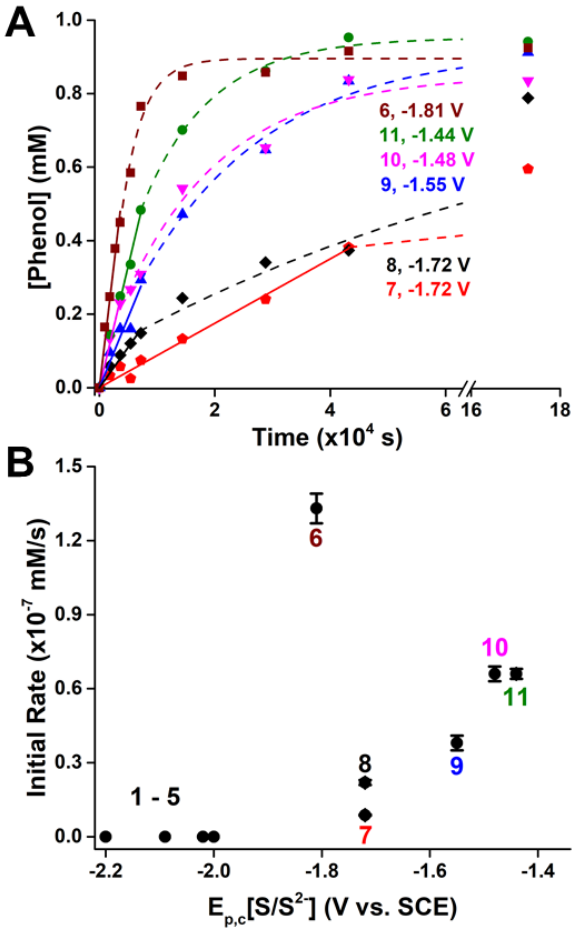

Figure 3.2. (A) The concentration of phenol product in reaction mixtures with 10 μM $CuInS_2$/ZnS QDs, 0.001 M substrate (labeled as in **Table 3.1**), and 0.1 M TEA in DMSO-d_6 as function of time of illumination with a 4.5-mW, 532-nm laser diode. The potentials listed in the legend correspond to the measured $E_{p,c}[S/S^{2-}]$ value for each substrate. The lines are the fits used to acquire the initial rates of the reactions. (B) The rate constants, as determined by the method of initial rates, for the deprotection reactions as a function of the $E_{p,c}[S/S^{2-}]$ of the substrates, listed in **Table 3.1**.

None of the other substrates have substituents known to bind to the surfaces of semiconductor QDs, which typically occurs through the coordination of surface metal ions (by, *e.g.*, COO^-, S^-) or dative binding of surface metal ions (by, *e.g.*, NH_2).[22, 67] Importantly, carboxylate groups such as the one on **6** is known, at least for CdSe QDs, to be *reversible* binders,[57] so that once the deprotection occurs, the product will not permanently block its catalytic site on the QD surface.

To support our proposal that increasing a substrate's affinity for the QD surface increases the initial rate of 2-e^- deprotection of that substrate, we compared the performances of photocatalysts $CuInS_2$/ZnS and *fac*-$Ir(ppy)_3$ for the deprotection of substrates **6** and **11**, **Figure 3.3**. Because *fac*-$Ir(ppy)_3$ does not absorb 532 nm light, we used a 5-mW 405-nm laser as an excitation source; we adjusted the catalyst loading to achieve the same optical density at 405 nm for the two photocatalysts (1 mol% $CuInS_2$ QDs; 9.7 mol% $Ir(ppy)_3$). The photoredox steps for deprotection of **11** should be diffusion controlled for both $Ir(ppy)_3$ and the QDs, since **11** does not have a group with affinity for the QD surface. $Ir(ppy)_3$ generates a factor of six more phenol from **11** than does the QD photocatalyst within the first 15 minutes of illumination. This result is expected, at least at short reaction times, because $Ir(ppy)_3$'s excited-state lifetime (~2 μs)[123] is ~50× longer than that of the QDs (35 ns).[49] A longer excited state lifetime increases the probability of a charge transfer reaction before the photocatalyst returns to its ground state. The longer lifetime of $Ir(ppy)_3$ makes

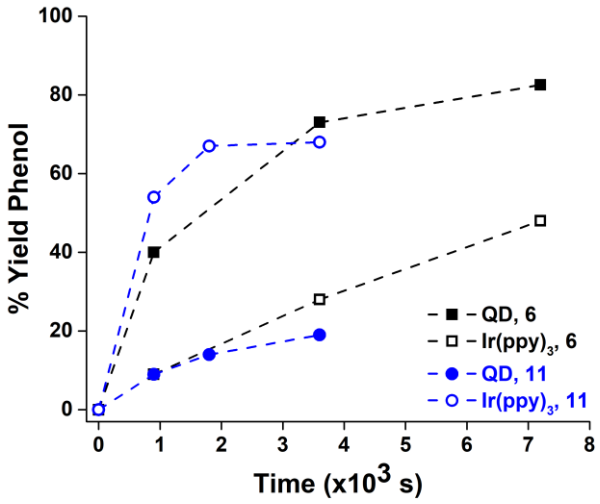

Figure 3.3. The yield of phenol product after the photocatalyzed deprotections of substrate **6** (black squares) and substrate **11** (blue circles) using 1 mol % $CuInS_2$ QDs (filled symbols) and 9.7 mol % *fac*-$Ir(ppy)_3$ (open symbols) upon illumination from a 5-mW, 405-nm laser. **6** has a carboxylic acid substituent and **11** has no substituent with reported affinity for the QD surface.

the results of the reaction of substrate **6**, which *does* have a carboxylate binding group for the QD surface but has no mechanism for generating a complex with $Ir(ppy)_3$, even more notable: the QDs generate a factor of 6.7 more phenol from **6** than does $Ir(ppy)_3$ within the first 15 minutes of illumination. This comparison not only supports our proposal that meta-stable association of the substrate and the QD provides a kinetic advantage for this 2-e^- reaction, but also that this kinetic advantage more than compensates for its shorter excited-state lifetime when compared to $Ir(ppy)_3$.

3.5 Orthogonality and scope of QD-photocatalyzed deprotection method

To demonstrate the orthogonality of this photocatalyzed deprotection method, we synthesized substrates that contain two protecting groups (compounds **12**, **13**, **14**), one 4-acetylphenyl sulfonate group and another protecting group that, thermodynamically, should not be redox-active with respect to the photoexcited QD. The synthetic procedures for these substrates are in section 3.7. **Table 3.1** shows that, after 24 hours of illumination of the QD-substrate mixtures with 532-nm light, the % conversion matches the % yield for deprotection of **13** and **14**; we do not observe any perturbation of the tert-butyloxycarbonyl (Boc) or toluenesulfonyl (Ts) protecting groups on those substrates. Although QDs successfully liberate phenol from **12**, the % conversion of starting material is 15 percentage points greater than the % yield of desired product. We suspect the benzyl ether groups on the substrate and the desired, deprotected product may partially decompose when subjected to these reductive conditions, see section 3.7 for more details. Additionally, as discussed above, we suspect that the % conversion of substrates **12** and **13** is limited by binding of the sulfinate anion product to the surface of the QD, which poisons the catalyst.

Common reducing agents for aryl sulfonyl deprotections, including magnesium, SmI_2, $LiAlH_4$, and sodium amalgam[101] can also cause unwanted reductions of carbonyl groups. To demonstrate

the functional group tolerance of the photocatalytic deprotection route, we attempted photo-deprotections of **15**, derived from estrone, and **16**, derived from vanillin, which contain carbonyl groups that would be reduced in the presence of any of the chemical reducing agents listed above. **Table 3.1** shows that, upon illumination with 532-nm light for 24 h, we achieve selective cleavage of **15** to liberate estrone without perturbation of the ketone. In contrast, we observe no formation of vanillin from **16** even though 98% of starting material has disappeared. Given the disappearance of the sharp aldehyde peak after illumination (see section 3.7), we suspect the QD reduces the aldehyde to form a ketyl radical, which then couples to another radical to form C–C products.[56]

3.6 Chapter Summary

In summary, photo-redox catalysis is a simple and effective route to the reductive deprotection of aryl sulfonyl-protected phenols using green (532-nm) light and $CuInS_2$/ZnS QDs as photocatalysts, as long as the potential needed for the required two electron transfers, $E_{p,c}$, is less than the measured reduction potential of the QD (~-1.9 V *vs*. SCE). The initial rate of deprotection increases as $E_{p,c}$ becomes more positive. We find that, if a substrate contains a QD-binding group, here a carboxylic acid, the rate of deprotection is greatly accelerated from that expected from the $E_{p,c}$ value of the substrate, likely because the substrate can associate with a surface of a QD, and the rates of the two electron transfer reactions are not diffusion-controlled. The kinetic advantage provided by reversible association of QD and substrate more than compensates for the shorter excited-state lifetime of $CuInS_2$/ZnS QDs when we compared their performance to that of *fac*-$Ir(ppy)_3$. The QD-catalyzed photodeprotection method is selective for the removal of sulfonyl protecting groups with electron-withdrawing substituents in the presence of Boc and tosyl groups, and does not perturb proximate ketones, which are generally vulnerable to many chemical

reduction methods used for this class of reactions. The orthogonality and selectivity of this method makes it potentially attractive for accomplishing deprotection steps within multi-step syntheses of complex molecules. Furthermore, it might be useful in light-controlled syntheses of polymers that proceed through successive protection and deprotection reactions.[124-125] Finally, photocatalyzed deprotection reactions may be a route to unique ligand shell structures on QDs that cannot be accessed by ligand exchange; such structures could be useful for a wide variety of chemical sensing and biological tagging applications.[126]

3.7 Supplementary Information

3.7.1 Synthesis of $CuInS_2$/ZnS QDs.

$CuInS_2$ Cores. We synthesized $CuInS_2$ QDs using a modified literature procedure.[46] A 100 mL three-neck round bottom flask was charged with 0.285 g CuI, 0.330 g $InCl_3$, and 7.5 mL trioctylphosphine (TOP, 97 %) in a glovebox. The flask was connected to Schlenk line. 15 mL of 1-octadecene (ODE, 90 %) and 9 mL of oleylamine (70 %) were added to the flask. The flask was heated under vacuum at 100 °C for 60 mins. The flask was then heated to 110 °C, and a solution of 310 μL of bis(trimethylsilyl) sulfide in 7.5 mL of degassed and dried ODE was injected under nitrogen. The heating mantle was removed, and the flask was cooled in a water bath after the desired size of QD was achieved (approximately 30 s). The reaction mixture was split among four 50 mL Falcon tubes, washed with ethanol, and centrifuged at 3500 rpm for 5 minutes. The supernatants were decanted, and the pellets were suspended in a minimal amount of toluene.

ZnS Shells. A 50 mL three-neck round bottom flask was charged with 0.3 g of zinc acetate dihydrate, 7.5 mL of ODE, and 1.5 mL of oleic acid (90%). The flask was put under vacuum and heated to 100°C for 30 minutes. The temperature of the flask was reduced to 80 °C and put under

N_2. The QD cores in toluene were injected into the flask. The flask was put back under vacuum slowly to minimize bumping. After 5 minutes, the heating mantle was removed, and the flask was cooled in a water bath. The mixture was split among six 15-mL Falcon tubes, and the particles were precipitated with acetone and centrifuged at 7500 rpm for 5 minutes. The supernatant was decanted, and the pellets were suspended in a minimal amount of toluene. The washing processed was repeated with methanol twice, and the final pellets were dried with a gentle flow of N_2 and then suspended in toluene.

3.7.2 Ligand Exchange with 3-Mercapto-1-Propanol.

100 nmol of QDs were dried from an aliquot of the QD stock solution in toluene. The particles were suspended in 0.5 mL of chloroform. A 15-mL Falcon tube was charged with 400 equiv. of 3-mercapto-1-propanol (MPO) per QD and 520 equiv. of tetramethylammonium hydroxide pentahydrate per QD. We added the QDs in chloroform, 3 mL of acetonitrile, and 2 mL of acetone to the Falcon tube, shaking after each addition, centrifuged the tube at 3500 rpm for 5 min, and decanted the supernatant. The pellet was then dried under N_2 for one hour, and the particles were suspended in DMSO-d_6.

3.7.3 Triethylamine Oxidation Mechanism.

Figure 3.4 shows the accepted mechanism for conversion of oxidized sacrificial reagent TEA to dimethylamine and acetaldehyde.[127]

3.7.4 Synthesis and Characterization of Substrates.

*Synthesis of Substrates **1** and **6**.* Substrates **1** and **6** were synthesized according to an adapted literature procedure.[118] A representative procedure is detailed here for **6**. A 25 mL round bottom flask was charged with 0.5 g phenol (5.3 mmol), 0.7 g NaOH (17.5 mmol), and 4.25 mL H_2O. The

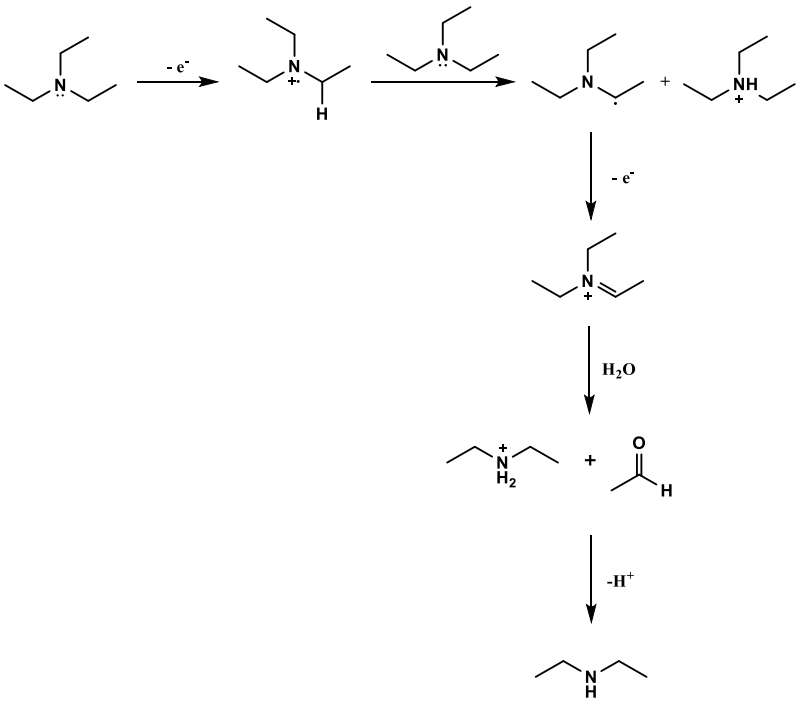

Figure 3.4. Mechanism of triethylamine degradation upon oxidation.

flask was cooled in an ice bath. A solution of 1.21 g tosyl chloride (6.4 mmol) in 7.4 mL THF was added dropwise. After the addition was complete, the reaction stirred at room temperature for 3 hours. The mixture was extracted with ethyl acetate, and the organic layer was washed with water three times before being dried over anhydrous $MgSO_4$. The solvent was removed under vacuum to isolate the product as a white solid.

*Synthesis of Substrates **2-5** and **7-13***. Substrates **2-5** and **7-13** were synthesized according to an adapted literature procedure.[120] A representative procedure is detailed here for **8**. 0.17 g phenol (1.8 mmol) phenol and 3.4 mL dry DCM were added to a 25 mL round bottom flask. The flask was cooled in an ice bath and purged with N_2. 0.31 mL triethylamine (2.2 mmol) was added. 0.5 g 1-naphthalenesulfonyl chloride (2.2 mmol) was dissolved in a minimal amount of dry DCM and

added dropwise. The solution stirred overnight. The reaction mixture was acidified to a pH of ~2, and the organic layer was extracted with DCM two times. The organic layers were combined and dried over Na_2SO_4, and the solvent was removed to isolate the crude product. Substrates **5** and **7-10** were recrystallized from ethanol to afford a pure, solid product. Substrates **2-4** and **11-13** were purified *via* column chromatography with a mixture of toluene and ethyl acetate.

*Synthesis of Substrate **14***. **14** was synthesized starting with resorcinol using adapted literature procedures.[119, 121] 0.5 g resorcinol (4.5 mmol) and 10 mL diethyl were added to a 100 mL round bottom flask. The flask was put under N_2 and cooled with an ice bath. 12 mL of a saturated aqueous solution of sodium hydrogen carbonate. A solution of 0.95 g 4-toluenesulfonyl chloride (5.0 mmol) was added dropwise. The solution stirred overnight. The mixture was then diluted with 30 mL of diethyl ether, washed two times with a saturated aqueous solution of potassium carbonate, washed two times with water, and washed with brine. The organic layer was dried over $MgSO_4$. The solvent was removed under vacuum to isolate the crude product. The crude product was purified *via* column chromatography with an 80:20 mixture of hexanes:ethyl acetate.

100 mg of 3-hydroxyphenyl 4-methylbenzenesulfonate (0.38 mmol) was dissolved in 1 mL of anhydrous DCM in a 20 mL scintillation vial. The vial was placed into an ice bath. 58 uL of triethylamine (0.42 mmol) and 0.043 g of 4-dimethylaminopyridine (DMAP, 0.36 mmol) were added to the vial. After the DMAP was fully dissolved, 0.092 g 4-acetylbenzenesulfonyl chloride (0.042 mmol) was added in portions. The solution stirred overnight. 5 mL of DCM was added to the vial. The organic layer was washed with brine twice and dried over anhydrous Na_2SO_4. The solvent was removed under vacuum to isolate the crude product. The crude product was purified

via column chromatography with a 95:5 mixture of toluene:ethyl acetate, and a white solid was isolated.

*Synthesis of Substrates **15** and **16***. Substrates **15** and **16** were synthesized according to an adapted literature procedure.[119] A representative procedure is detailed here for substrate **16**. 0.35 g vanillin (2.3 mmol) and 10 mL of anhydrous DCM were added to a 25 mL round bottom flask. The flask was put into an ice bath. 0.64 mL triethylamine (4.6 mmol) and 0.28 g DMAP (2.3 mmol) was added to the flask. 0.5 g of 4-acetylbenzenesulfonyl chloride (2.3 mmol) was added in portions. The solution stirred overnight. DCM was added to the flask, and the organic layer was washed with brine twice and dried over anhydrous Na_2SO_4. The solvent was removed under vacuum to isolate the crude product. The crude product was purified by passing it through a silica plug with 60:40 mixture of hexanes:ethyl acetate.

Characterization of Substrates. ^{1}H NMRs were collected on a 500 MHz Bruker Avance III HD system equipped with a TXO Prodigy probe. Mass spectra were collected on a Bruker AmaZon-SL.

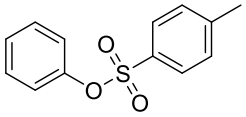

Phenyl tosylate (**1**). White solid. ^{1}H NMR (500 MHz, $CDCl_3$) δ 7.71 (d, *J* = 7.9 Hz, 2H), 7.33-7.26 (m, 5H), 6.98 (dd, *J* = 7.7, 1.7 Hz, 2H), 2.45 (s, 3H). MS (ESI) m/z: $[M+Na]^+$ 270.94.

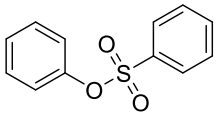

Phenyl benzenesulfonate (**2**). Colorless oil ^{1}H NMR (500 MHz, $CDCl_3$) δ 7.87 – 7.80 (m, 2H), 7.66 (tt, *J* = 7.5, 1.3 Hz, 1H), 7.56 – 7.49 (m, 2H), 7.32 – 7.21 (m, 3H), 7.00 – 6.95 (m, 2H). MS (ESI) m/z: $[M+Na]^+$ 256.96.

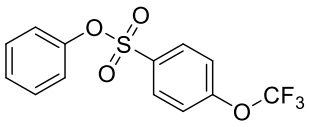

Phenyl 4-(trifluoromethoxy)benzenesulfonate (**3**)**.** Colorless oil ^{1}H NMR (500 MHz, $CDCl_3$) δ 7.89 (dt, *J* = 8.9, 2.1 Hz, 2H), 7.38 – 7.24 (m, 5H), 7.03 – 6.97 (m, 2H). MS (ESI) m/z: $[M+Na]^+$ 341.03.

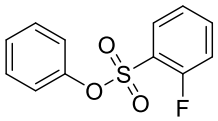

Phenyl 2-fluorobenzenesulfonate (**4)**. Colorless oil ^{1}H NMR (500 MHz, $CDCl_3$) δ 7.85 – 7.74 (m, 1H), 7.71 – 7.62 (m, 1H), 7.33 – 7.24 (m, 3H), 7.18 – 7.16 (m, 2H), 7.12 (d, *J* = 7.8 Hz, 2H). MS (ESI) m/z: $[M+Na]^+$ 274.96.

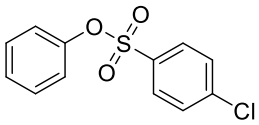

Phenyl 4-chlorobenzenesulfonate (**5)**. White solid. ^{1}H NMR (500 MHz, $CDCl_3$) δ 7.77 (d, *J* = 8.3 Hz, 2H), 7.51 (d, *J* = 8.3 Hz, 2H), 7.31 (q, *J* = 7.7 Hz, 3H), 7.00 (d, *J* = 7.8 Hz, 2H). MS (ESI) m/z: $[M+Na]^+$ 290.97.

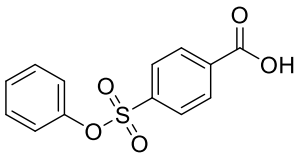

Phenyl 4-carboxybenzenesulfonate **6**. White solid. ^{1}H NMR (500 MHz, $CDCl_3$) δ 8.22 (d, *J* = 8.5 Hz, 2H), 7.94 (d, *J* = 8.4 Hz, 2H), 7.36 – 7.27 (m, 3H), 6.99 (dd, *J* = 8.5, 1.3 Hz, 2H). MS (ESI) m/z: $[M]^-$ 276.82.

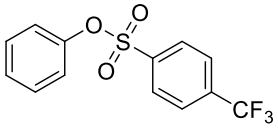

Phenyl 4-trifluoromethylbenzenesulfonate (**7**). White solid. ^{1}H NMR (500 MHz, $CDCl_3$) δ 7.97 (d, *J* = 8.2 Hz, 2H), 7.80 (d, *J* = 8.2 Hz, 2H), 7.31 (m, 3H), 7.00 (d, *J* = 7.4, 2H). MS (ESI) m/z: $[M+Na]^+$ 325.03.

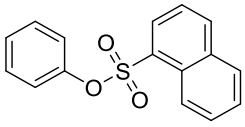

1-naphthalenesulfonic acid phenyl ester (**8**). White solid. ^{1}H NMR (500 MHz, $CDCl_3$) δ 8.83 (d, *J* = 8.7 Hz, 1H), 8.11 (dd, *J* = 20.0, 7.8 Hz, 2H), 7.99 (d, *J* = 8.2 Hz, 1H), 7.79 (t, *J* = 7.9 Hz, 1H), 7.68 (t, *J* = 7.6 Hz, 1H), 7.47 (t, *J* = 7.8 Hz, 1H), 7.20 – 7.14 (m, 3H), 6.87 (dd, *J* = 7.6, 2.2 Hz, 2H). MS (ESI) m/z: $[M+Na]^+$ 307.04.

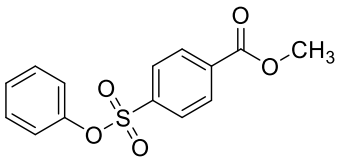

methyl 4-phenoxysulfonylbenzoate (**9**). White solid. ^{1}H NMR (500 MHz, $CDCl_3$) δ 8.17 (d, *J* = 8.5 Hz, 2H), 7.91 (d, *J* = 8.5 Hz, 2H), 7.35 – 7.27 (m, 3H), 7.02 – 6.95 (m, 2H), 3.97 (s, 3H). MS (ESI) m/z: $[M+Na]^+$ 315.04.

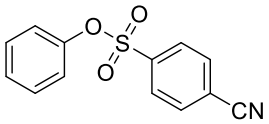

4-cyanobenzolsulfonsaeurephenylester (**10**). White solid. ^{1}H NMR (500 MHz, $CDCl_3$) δ 7.96 (d, *J* = 8.5 Hz, 2H), 7.83 (d, *J* = 8.4 Hz, 2H), 7.34 - 7.29 (m, 3H), 7.03 – 6.96 (m, 2H). MS (ESI) m/z: $[M+Na]^+$ 281.99.

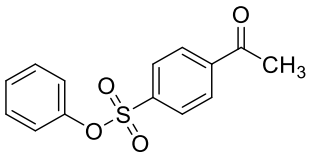

4-Acetyl-benzolsulfonsaeure-phenylester (**11**). White solid. ^{1}H NMR (500 MHz, $CDCl_3$) δ 8.07 (d, *J* = 8.5 Hz, 2H), 7.94 (d, *J* = 8.5 Hz, 2H), 7.35 – 7.28 (m, 3H), 7.35 – 7.28 (m, 2H), 2.66 (s, 3H). MS (ESI) m/z: $[M+Na]^+$ 299.04.

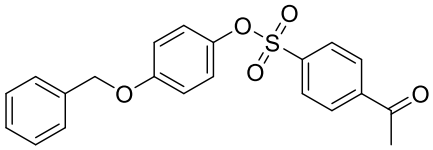

12. White solid. ^{1}H NMR (500 MHz, $CDCl_3$) δ 8.06 (d, *J* = 8.4 Hz, 2H), 7.92 (d, *J* = 8.4 Hz, 2H), 7.42 – 7.31 (m, 5H), 6.92 – 6.82 (m, 4H), 5.01 (s, 2H), 2.66 (s, 3H). MS (ESI) m/z: $[M+Na]^+$ 405.14.

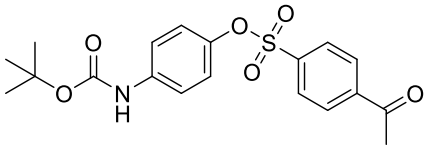

13. White solid ^{1}H NMR (500 MHz, $CDCl_3$) δ 8.06 (d, *J* = 8.5 Hz, 2H), 7.91 (d, *J* = 8.5 Hz, 2H), 7.28 (d, *J* = 8.7 Hz, 2H), 6.92 – 6.83 (m, 2H), 6.48 (s, 1H), 2.66 (s, 3H), 1.50 (s, 9H). MS (ESI) m/z: $[M+Na]^+$ 414.18.

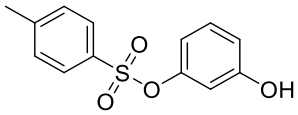

3-hydroxyphenyl 4-methylbenzenesulfonate (intermediate for **14**) White sold. ^{1}H NMR (500 MHz, $CDCl_3$) ^{1}H NMR (500 MHz, $CDCl_3$) δ 7.72 (d, *J* = 8.4 Hz, 2H), 7.31 (d, *J* = 8.6, 2H), 7.17 – 7.06 (m, 1H), 6.72 (ddd, *J* = 8.2, 2.4, 0.9 Hz, 1H), 6.59 – 6.50 (m, 2H), 2.45 (s, 3H)

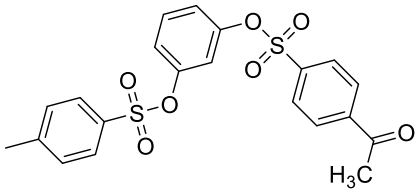

14. White solid. ^{1}H NMR (500 MHz, $CDCl_3$) δ 8.09 (d, *J* = 8.4 Hz, 2H), 7.89 (d, *J* = 8.5 Hz, 2H), 7.65 (d, *J* = 8.3 Hz, 2H), 7.33 (d, *J* = 8.1 Hz, 2H), 7.23 (t, J = 8.3 Hz, 1H), 6.96 – 6.90 (m, 2H), 6.69 (t, *J* = 2.3 Hz, 1H), 2.67 (s, 3H), 2.46 (s, 3H). MS (ESI) m/z: $[M+Na]^+$ 469.10.

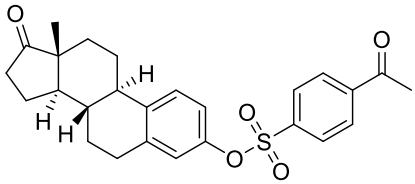

15. Yellow solid. ^{1}H NMR (500 MHz, $CDCl_3$) δ 8.09 (d, *J* = 8.5 Hz, 2H), 7.97 (d, *J* = 8.5 Hz, 2H), 7.17 (d, *J* = 8.6 Hz, 1H), 6.79 (d, *J* = 2.6 Hz, 1H), 6.67 (dd, *J* = 8.6, 2.7 Hz, 1H), 2.84 (dd, *J* = 9.1, 4.3 Hz, 2H), 2.67 (s, 3H), 2.51 (dd, *J* = 19.1, 8.8 Hz, 1H), 2.39 – 2.31 (m, 1H), 2.27 – 2.22 (m, 1H), 2.14 (dt, *J* = 18.6, 8.9 Hz, 1H), 2.09 – 1.93 (m, 3H), 1.66 – 1.37 (m, 5H), 1.29 – 1.24 (m, 1H), 0.91 (s, 3H). MS (ESI) m/z: $[M+Na]^+$ 475.24.

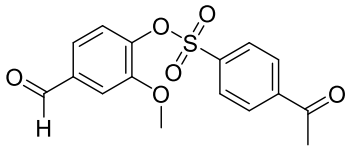

16. White solid. ^{1}H NMR (500 MHz, $CDCl_3$) δ 9.94 (s, 1H), 8.09 (d, *J* = 8.5 Hz, 2H), 8.01 (d, *J* = 8.6 Hz, 2H), 7.51 – 7.36 (m, 3H), 3.63 (s, 3H), 2.67 (s, 3H). MS (ESI) m/z: $[M+Na]^+$ 357.08.

3.7.5 Electrochemical Measurements.

Cyclic voltammograms of substrates, **Figure 3.5**, were obtained using a Princeton Applied Research VersaSTAT 3 potentiostat, a glassy carbon working electrode, a silver wire reference electrode, and a Pt counter electrode in anhydrous DMSO. The solutions were 10 mM substrate, 100 mM tetramethylammonium hexafluorophosphate, and 1 M triethylamine. Decamethylferrocene was added as an internal standard. All samples were purged with N_2 before measurement.

A cyclic voltammogram of the QDs, **Figure 3.6**, was collected on a sample of 1 mM $CuInS_2$/ZnS QDs with MPO ligands and 50 mM tetramethylammonium hexafluorophosphate with a ferrocene internal standard. The oxidation of the internal standard is not entirely reversible in the CV due to interactions between oxidized ferrocene and the QDs.

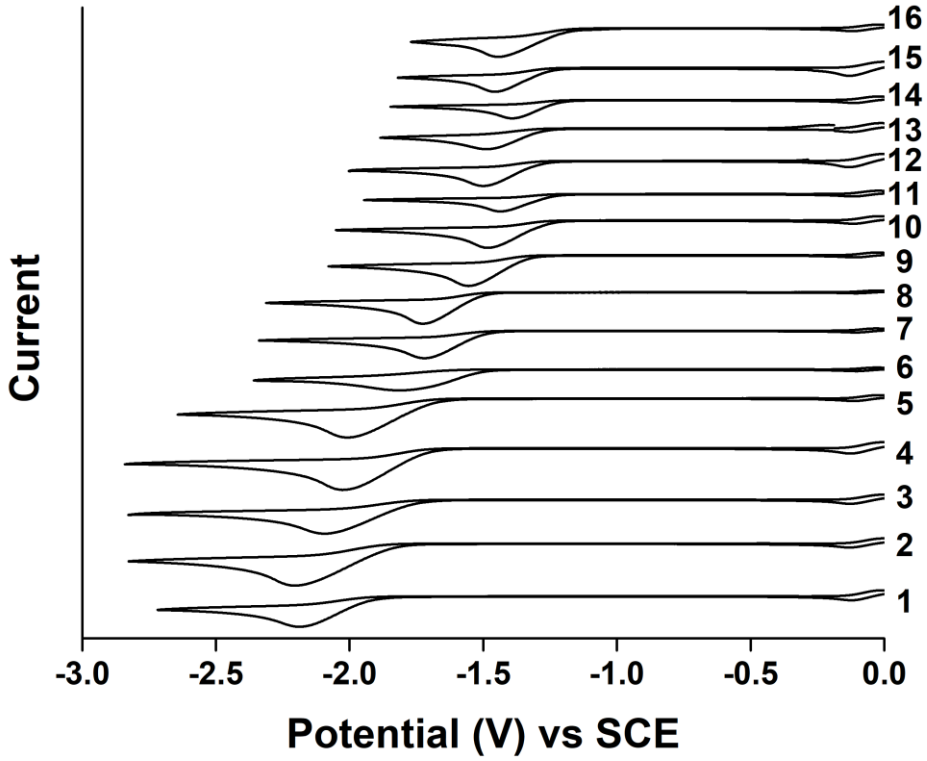

Figure 3.6. CVs of solutions of 10 mM substrate (numbered as in **Table 3.1**) under N_2 with 100 mM tetrabutylammonium hexafluorophosphate, and 1 M triethylamine in DMSO, using a glassy carbon working electrode, a Ag wire reference electrode, and a Pt wire counter electrode. The potentials are referenced to SCE using a decamethylferrocene internal standard.

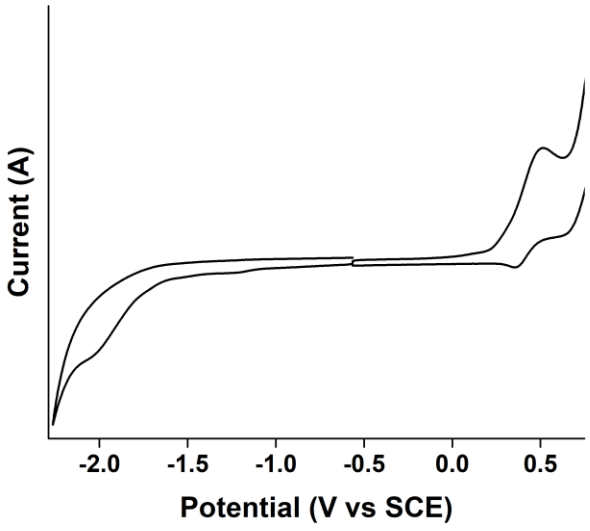

Figure 3.5. CV of a sample of 1 mM $CuInS_2$ QDs with MPO ligands and 50 mM tetramethylammonium hexafluorophosphate with a ferrocene internal standard.

3.7.6 Photocatalytic Setup.

All catalytic mixtures were put into air-tight vials and purged with Ar before illumination. Samples of 10 μM $CuInS_2$ QDs, 0.001 M substrate, and 0.1 M triethylamine in DMSO-d_6 were illuminated with a 4.5-mW, 532 nm laser diode (Thorlabs CPS532), while being constantly stirred. After illumination, a ferrocene internal standard (0.2 equiv. relative to substrate) was added, and ^{1}H NMR spectra of the catalytic mixtures were collected on a 400 MHz Bruker Avance III HD Nanobay system. Absorbance spectra were also collected on all samples.

Photocatalysis Experiments Comparing Activity of $CuInS_2$ QDs and fac-Ir(ppy)$_3$. Samples containing QDs or *fac*-Ir(ppy)$_3$ with OD=0.15 at 405nm, 0.001 M substrate, and 0.1 M triethylamine in DMSO-d_6 were illuminated with a 5-mW, 405 nm laser. After illumination, a ferrocene internal standard (0.2 equiv. relative to substrate) was added, and ^{1}H NMR spectra of the catalytic mixtures were collected on a 400 MHz Bruker Avance III HD Nanobay system. Absorbance spectra were also collected on all samples.

*Photocatalysis Experiments Comparing Trimethylphenazine to Triethylamine***.** Samples of 10 μM, 0.001 M substrate, 0.01 M hole quencher (triethylamine or dimethylphenazine) in DMSO-d_6 were illuminated with a 4.5-mW, 532 nm laser diode. After illumination, a ferrocene internal standard (0.2 equiv. relative to substrate) was added, and ^{1}H NMR spectra of the catalytic mixtures were collected on a 400 MHz Bruker Avance III HD Nanobay system. Absorbance spectra were also collected on all samples.

*Photocatalysis Experiment to Determine Isolated Yield of Deprotection of **15**.* A sample of 220 uM QDs, 10 mg **15** (0.022 M), 2.2 M TEA in 1 mL DMSO-d_6 was illuminated with a 4.5-mW, 532 nm laser diode for 24 hours. After illumination, DMSO-d_6 was removed *via* a high vacuum

line. The residue was dissolved in DCM and purified *via* column chromatography with an 80:20 mixture of hexanes:ethyl acetate. 5.1 mg (85 % yield) of estrone was isolated as a white solid. The ^{1}H NMR spectrum matched a ^{1}H NMR of an authentic estrone sample.

*3.7.7 Quantification of Catalytic Performance for Substrates **1-14** and **16.***

NMR yields are listed in **Table 3.1** for the deprotection of substrates **1-14** and **16** by $CuInS_2$/ZnS QDs upon illumination. A ferrocene internal standard (0.2 mol equiv. relative to substrate) was used to determine the yield of phenolic product. In each of the **Figures 3.7** to **3.17** below, the top spectrum (blue) corresponds to the control sample, which was not illuminated, and the bottom spectrum (red) corresponds to the sample that was illuminated according to the conditions outlined in the footnotes of **Table 3.1**.

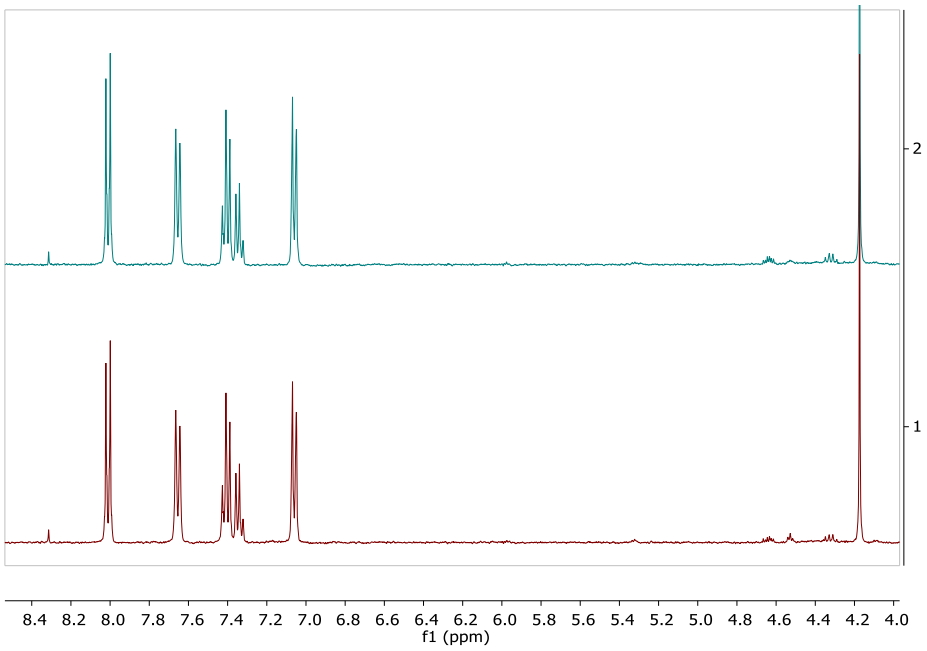

Figure 3.7. NMR spectra of the reaction mixtures from the deprotection of **3**. This a representative example of substrates (**1**-**5**) that QDs failed to deprotect.

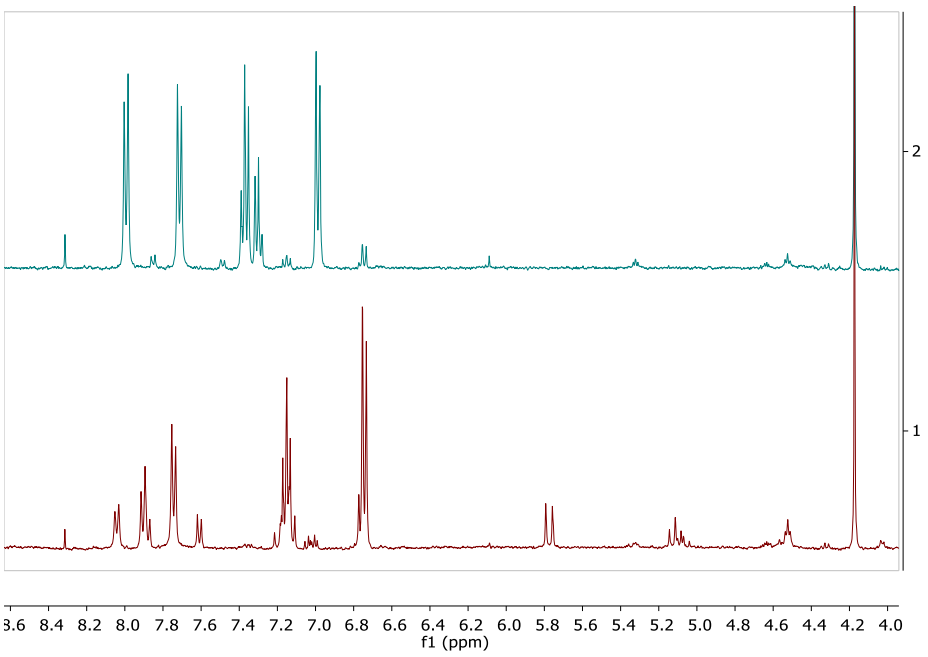

Figure 3.8. NMR spectra of the reaction mixtures from the deprotection of **6**.

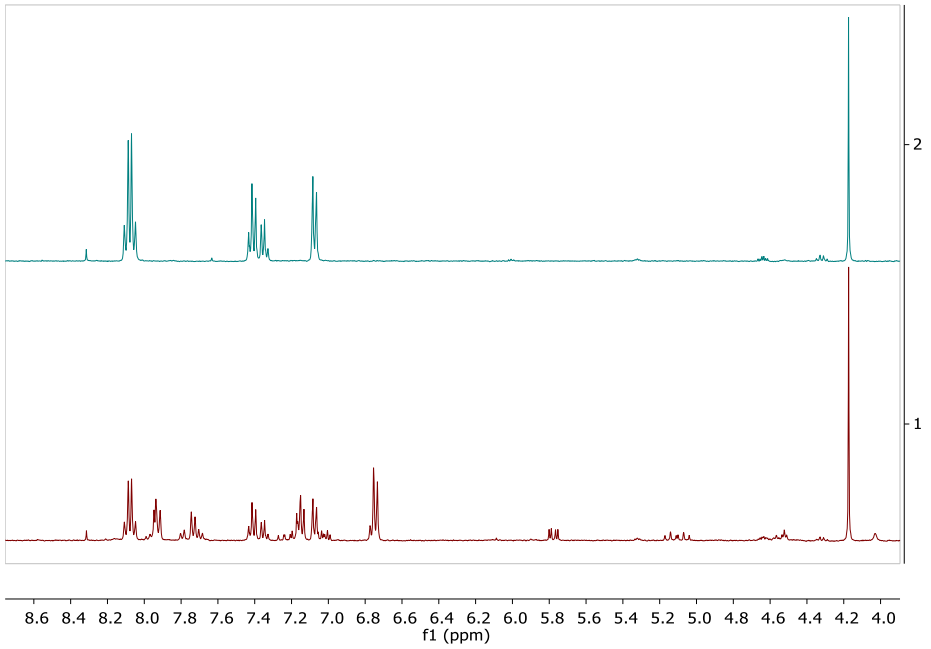

Figure 3.9. NMR spectra of the reaction mixtures from the deprotection of **7**.

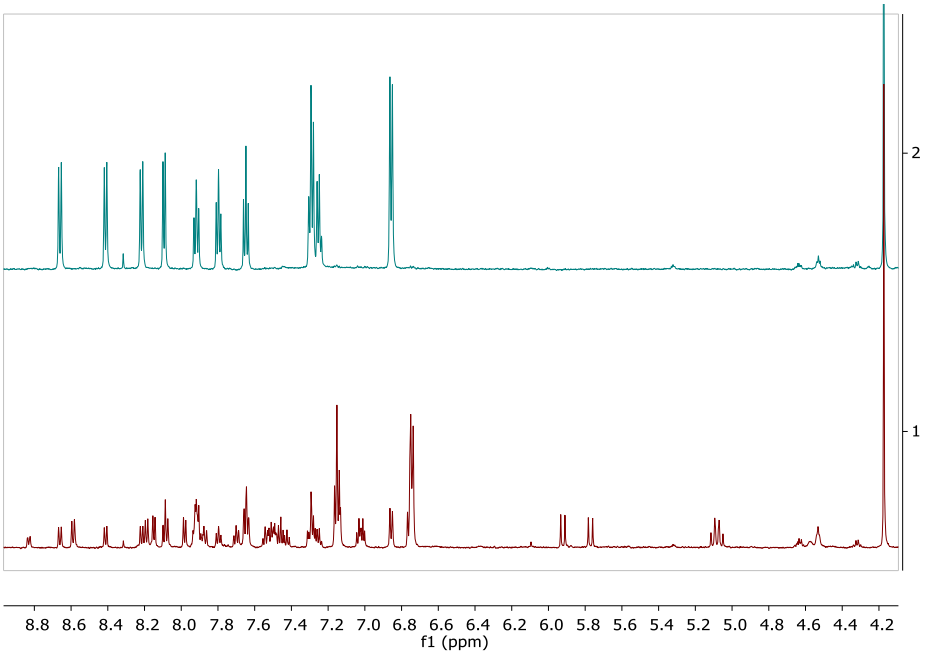

Figure 3.10. NMR spectra of the reaction mixtures from the deprotection of **8**.

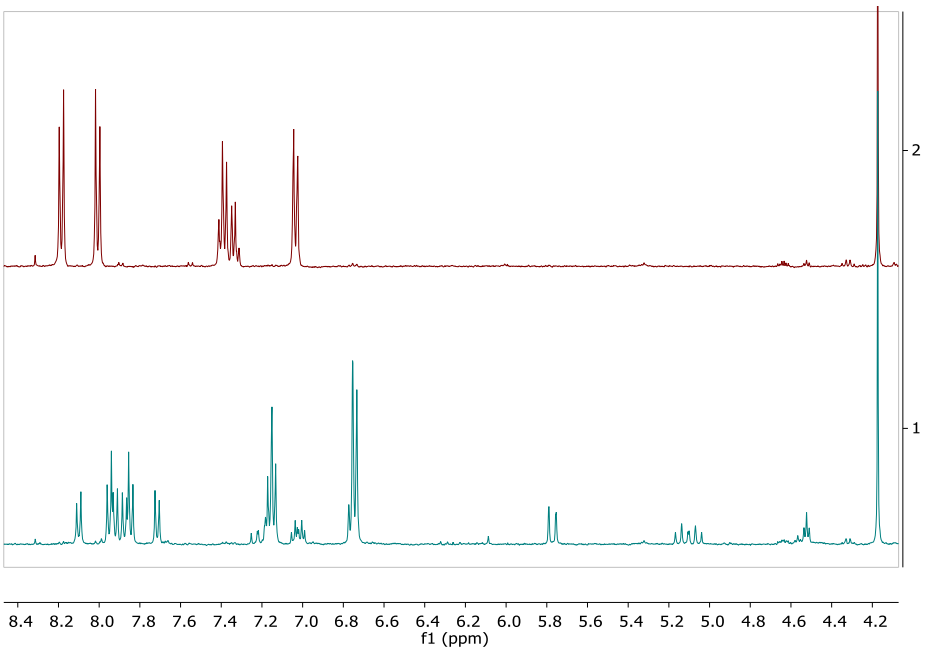

Figure 3.11. NMR spectra of the reaction mixtures from the deprotection of **9**.

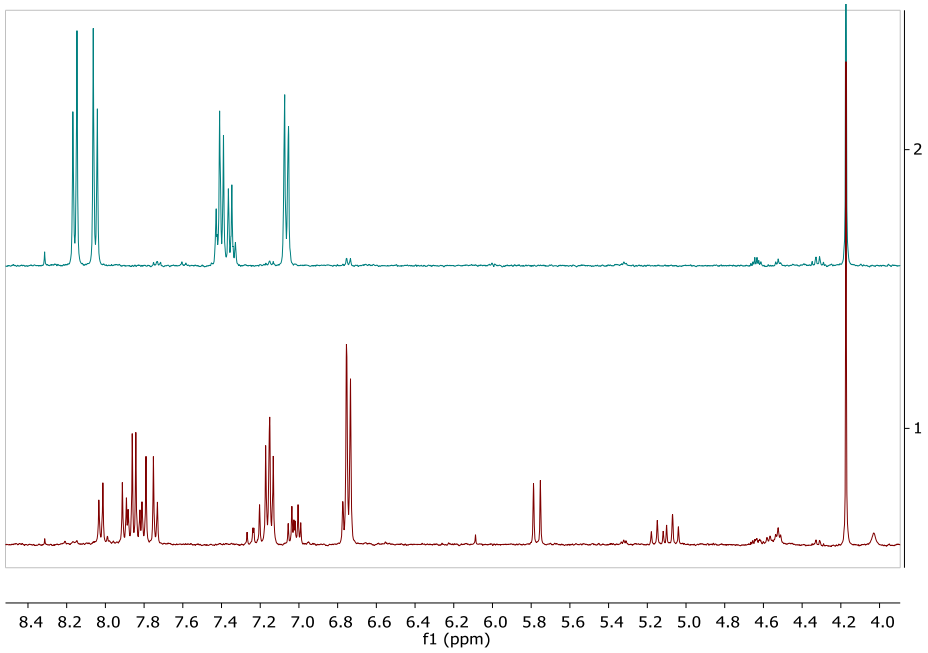

Figure 3.12. NMR spectra of the reaction mixtures from the deprotection of **10**.

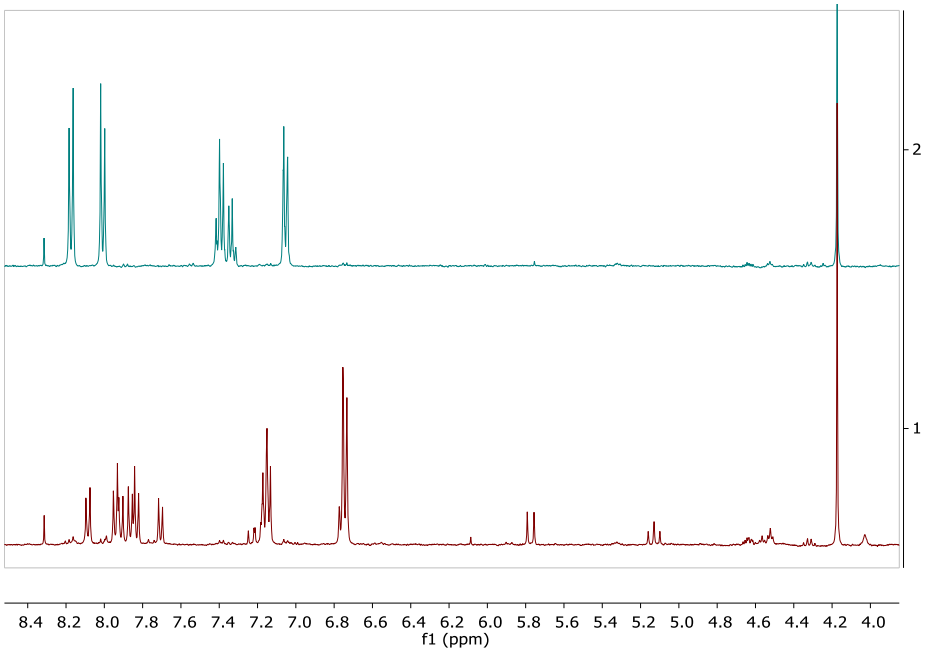

Figure 3.13. NMR spectra of the reaction mixtures from the deprotection of **11**.

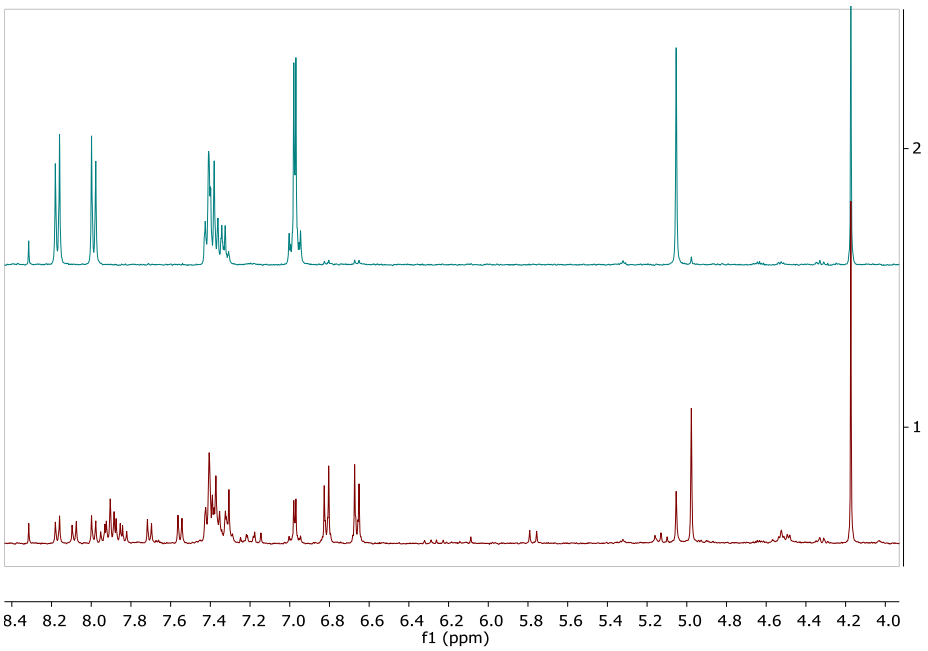

Figure 3.14. NMR spectra of the reaction mixtures from the deprotection of **12**.

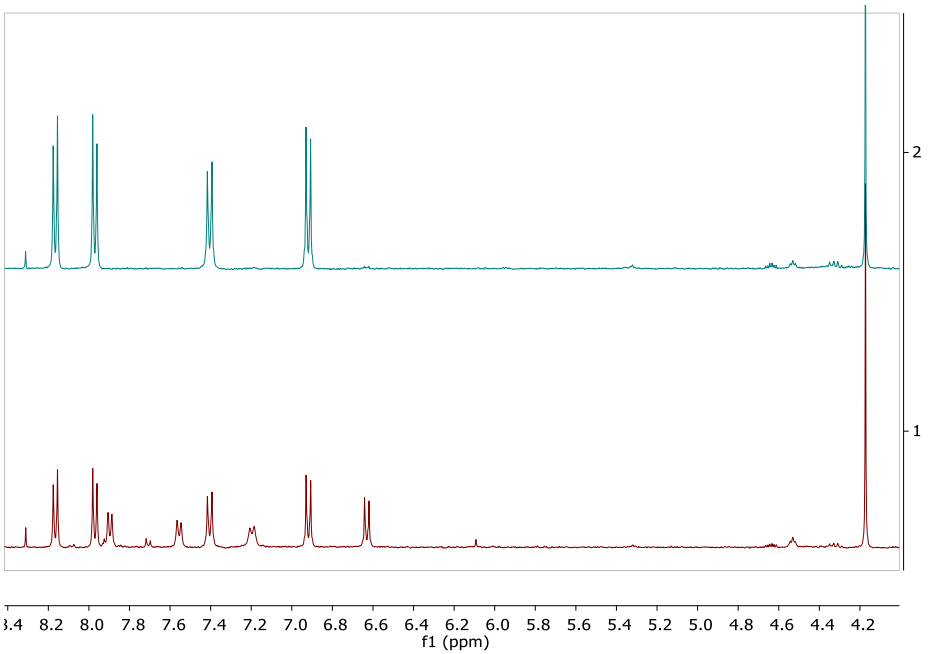

Figure 3.15. NMR spectra of the reaction mixtures from the deprotection of **13**.

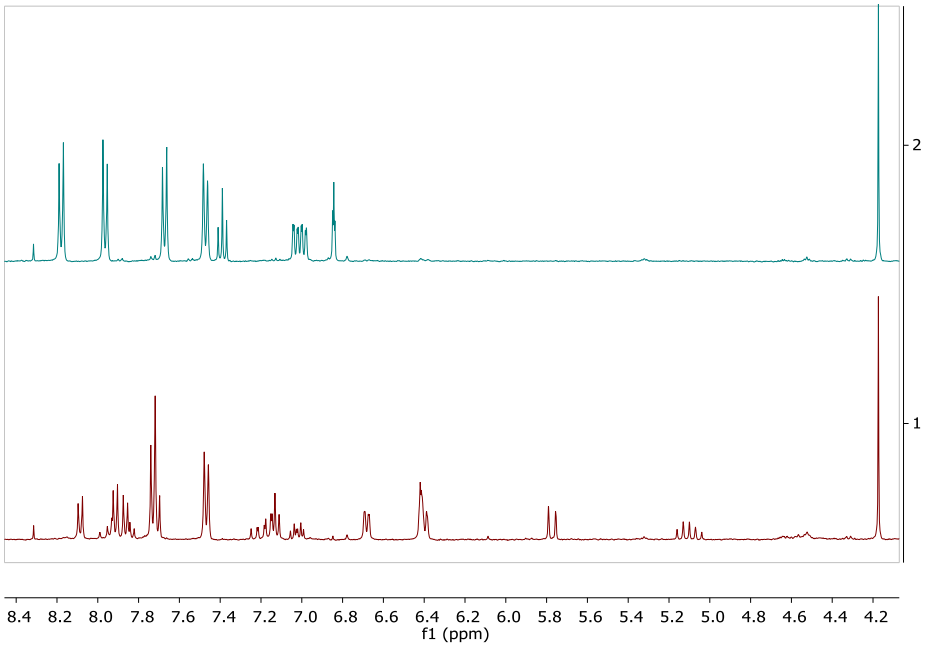

Figure 3.16. NMR spectra of the reaction mixtures from the deprotection of **14**.

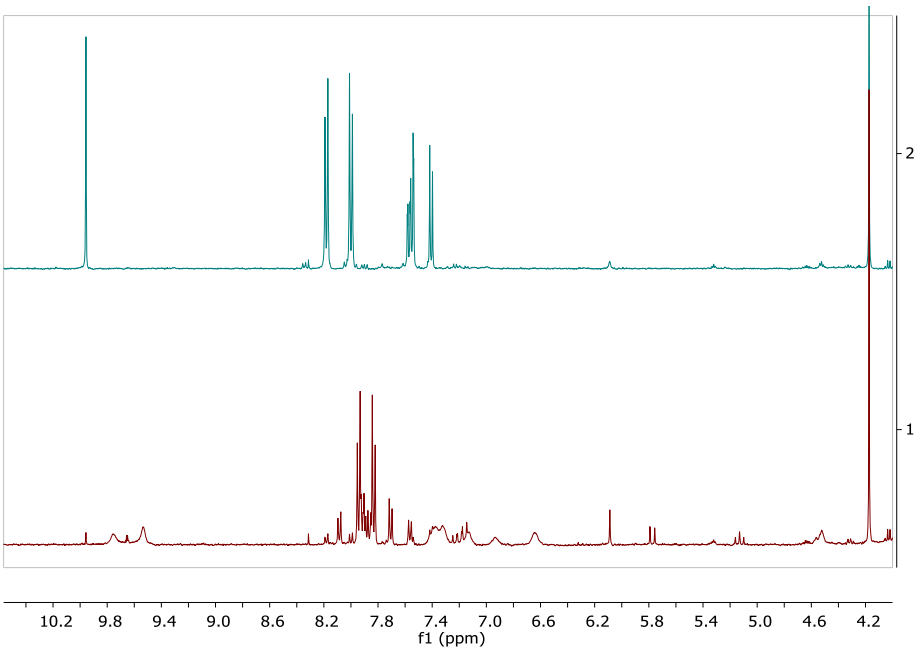

Figure 3.17. NMR spectra of the reaction mixtures from the deprotection of **16**.

3.7.8 Control Studies.

Experiments conducted in the absence of illumination or in the absence of QDs show no phenol formation, **Table 3.2**. While QDs illuminated without added sacrificial reductant do form phenol from substrate **11**, the deprotection proceeds more slowly than when TEA is added to the reaction mixture. The deprotection reaction likely proceeds without added TEA because (1) the MPO ligands on the surface of the QDs can act as a sacrificial reductant and (2) the $CuInS_2$ QDs are copper-deficient,[46] so they can accommodate holes. We suspect that hole transfer is the rate limiting step of this redox reaction,[7] so the introduction of an excess sacrificial reductant, *e.g.* TEA, accelerates the deprotection reaction.

Table 3.2. Control Studies for QD-catalyzed Deprotection of **11.**

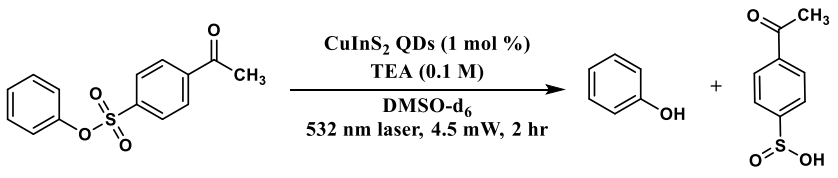

entry	deviation from standard	% yield phenol
1	none	32
2	no light	0
3	no QDs	0
4	no TEA	15

3.7.9 QD Catalyst Stability.

To monitor the catalytic stability of the QDs, we compared their ground state absorbance spectra before and after illumination; an example is shown in **Figure 3.18**. We do not observe any negative features when we subtract the absorbance spectrum from after catalysis from the spectrum before catalysis, so we conclude that the QDs did not etch or precipitate. Additionally, we observe a peak *ca.* 350 nm in the difference spectrum. This feature can be attributed to the sulfinic acid that forms as a result of the deprotection reaction, **Figure 3.19**. The absorbance spectrum of the sulfinic acid molecule is dependent on the pH of the solution. An authentic sample of the sulfinic acid was prepared following a literature procedure.[128]

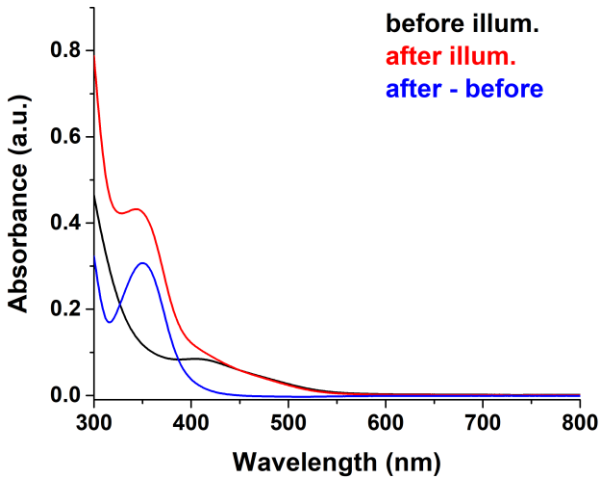

Figure 3.18. Absorbance spectra of catalysis mixture for **6** before (black), after (red), and a difference spectra (blue) illumination with 532 nm light.

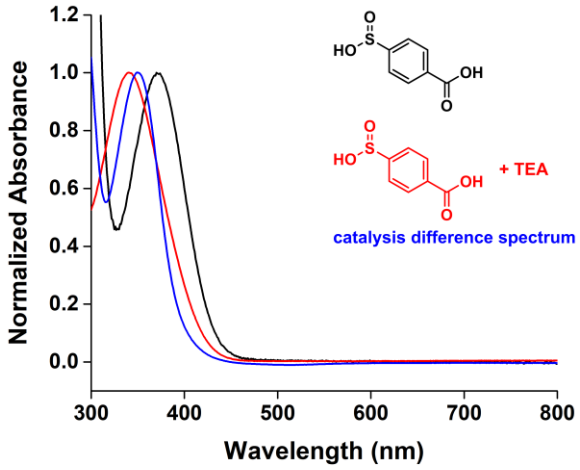

Figure 3.19. Normalized absorbance spectra of sulfinic acid formed as a result of deprotection of **6** in DMSO (black), in a 0.1 M TEA solution in DMSO (red), and difference spectra (blue) from **Figure 3.18**.

3.7.10 Analysis of Initial Rate of Reaction vs. Yield of Phenol

For substrates **6-11**, we compared the initial rate of the reaction and the yield of phenol liberated after 48 hours of illumination, listed in **Table 3.1**, **Figure 3.20**. We oberserve that the yield of phenol after 48 hours generally increases as the initial rate of the reaction increases. We

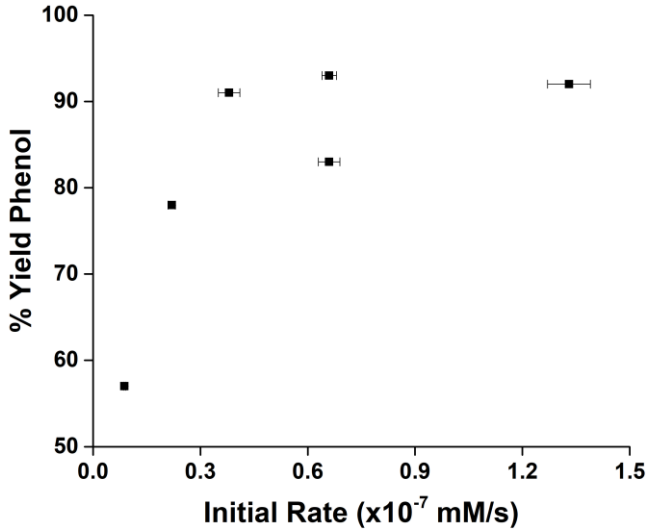

Figure 3.20. The yield of phenol produced after 48 h upon QD-photocatalyzed deprotection of **6-11** as a function of the initial rate of the reaction.

suspect that the sulfinate ions that form can bind to the surface of the QD, and, for the slower reactions, the sulfinate ion can poison the catalyst before all of the substrate is coverted to product.

3.7.11 Benzyl Ether Reaction with QDs.

When substrate **12** was subjected to photocatalysis conditions for 24 hours, 69% of the starting material was consumed, but the yield of the deprotection reaction was only 54%, **Table 3.1**. We attribute this disagreement between % conversion and % yield to the undesired decomopsition of benzyl ether, which is susceptible to reduction. When we subjected a sample of 4-benzyloxyphenol, the desired product from the deprotection of **12**, to the catalytic conditions, we observed the appearance of new peaks in the aromatic region in the ^{1}H NMR spectrum and the loss of ~10 % of 4-benzyloxyphenol, **Figure 3.21**.

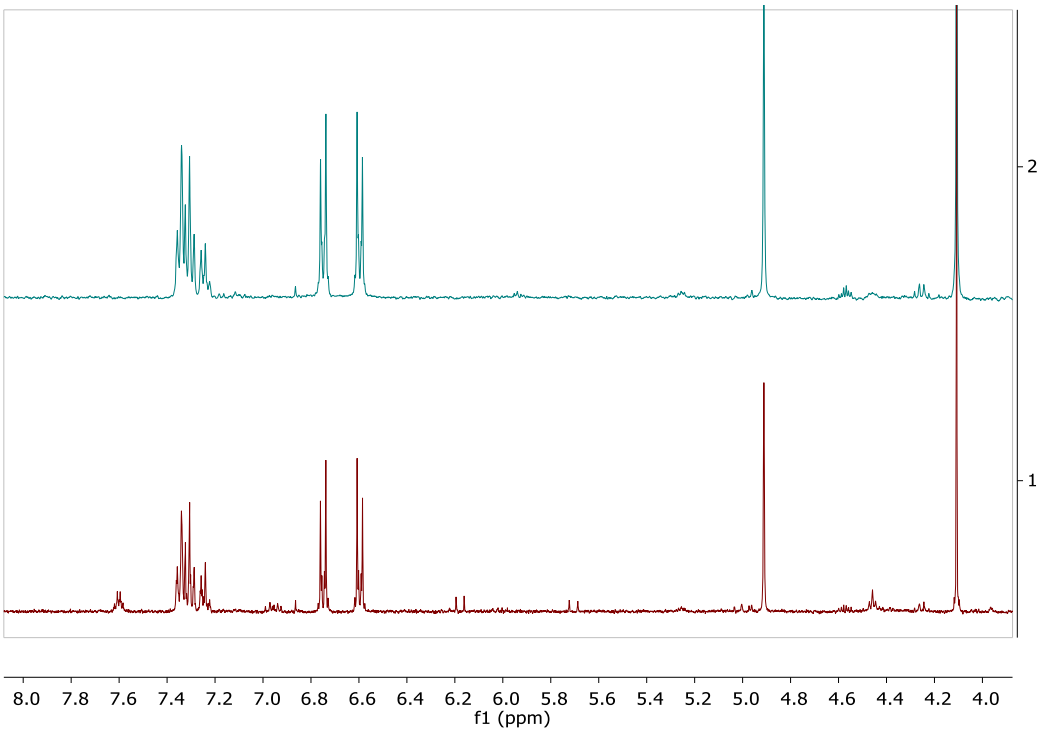

Figure 3.21. ^{1}H NMR spectra of mixtures of 10 μM $CuInS_2$ QDs, 0.001 M 4-benzyloxyphenol, and 0.1 M triethylamine in DMSO-d_6 were illuminated with a 4.5-mW, 532 nm laser diode for 0 hr (blue, top spectrum) and 24 hours (red, bottom spectrum).

3.7.12 Decomposition of Aldehydes by QDs.

When substrate **16** was subjected to photocatalysis conditions for 24 hours, 97% of the starting material was consumed, while the yield of vanillin, the desired product, was 0, **Table 3.1**. From the ^{1}H NMR spectrum of the reaction mixture after illumination, **Figure 3.17**, we observe the formation of several broad features between 9.4 and 9.8 ppm and a partial dissapearance of the sharp signal at 10 ppm, the aldehyde region the NMR spectrum. When we subjected a sample of vanillin, the desired product from the deprotection of **16**, to the catalytic conditions, we oberve the appearance of multiple signals in the aldehyde and aromatic regions of the NMR spectrum, **Figure 3.22**. We suspect that QDs reduce the alheyde to form a reactive ketyl radical, leading to undesired C-C coupling side reactions.[56]

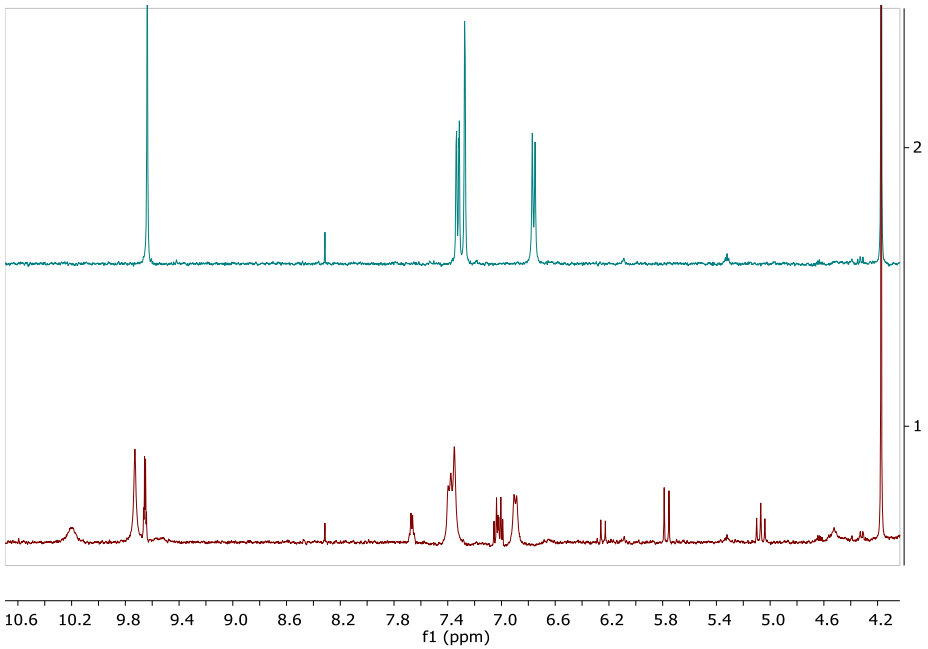

Figure 3.22. ^{1}H NMR spectra of mixtures of 10 μM $CuInS_2$ QDs, 0.001 M vanillin, and 0.1 M triethylamine in DMSO-d_6 were illuminated with a 4.5-mW, 532 nm laser diode for 0 hr (blue, top spectrum) and 24 hours (red, bottom spectrum).

3.7.13 NMR Spectra of Substrates.

1,

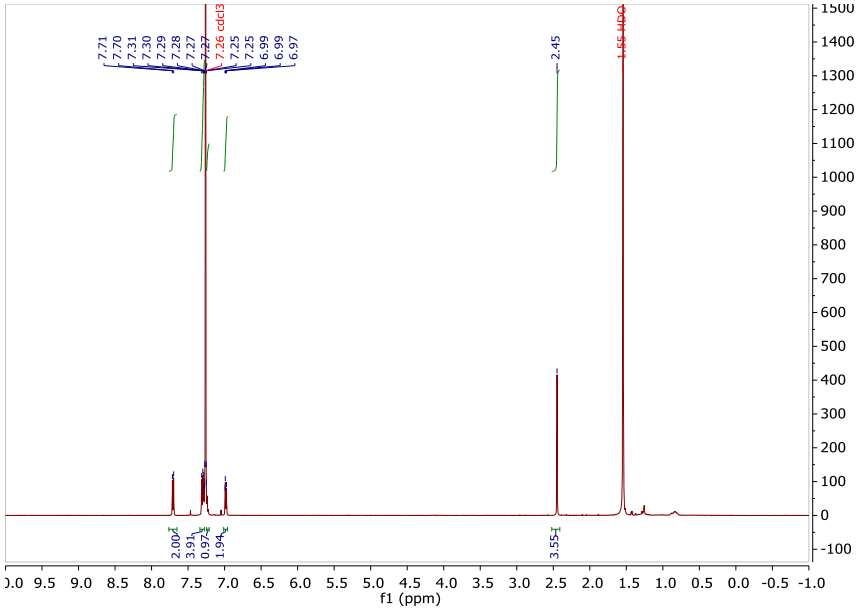

2,

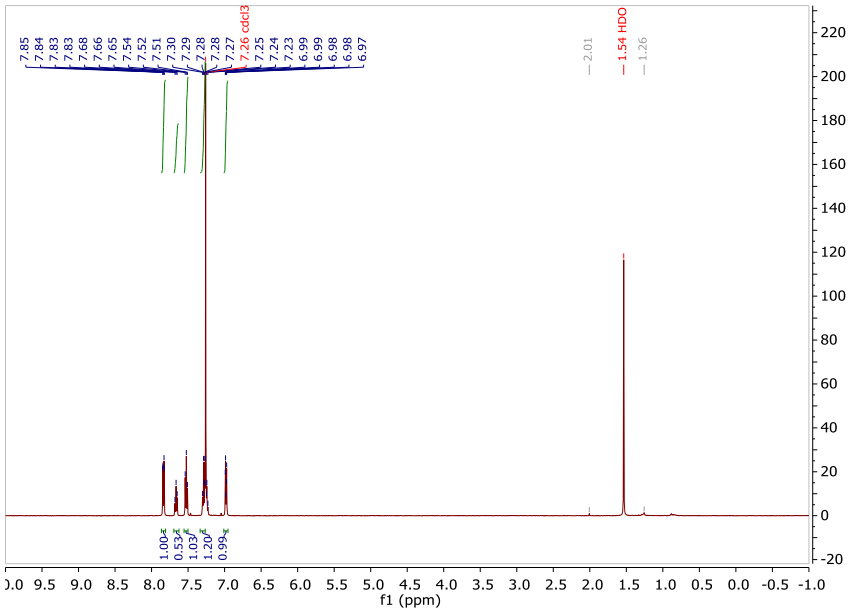

3,

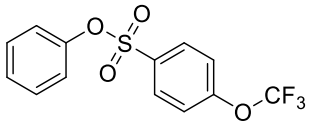

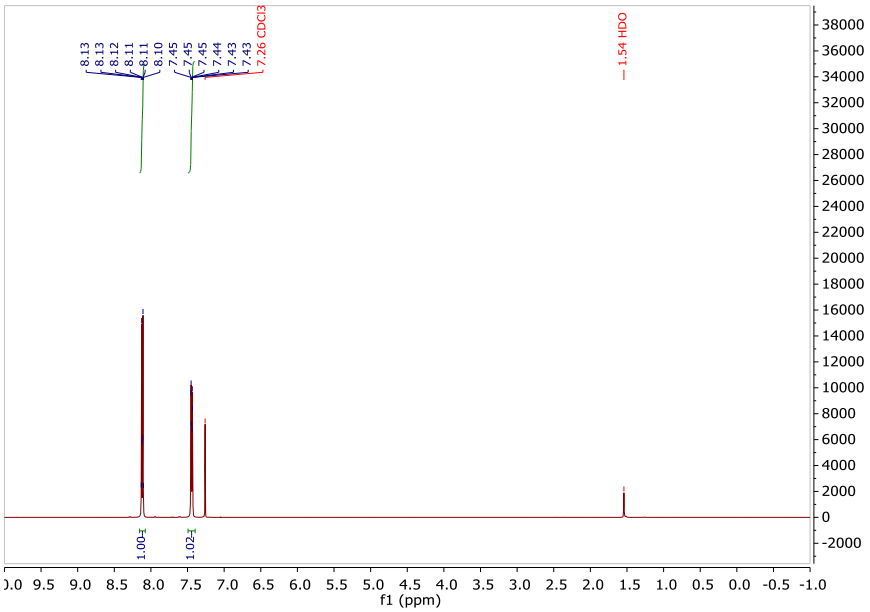
8.13
8.13
8.12
8.11
8.11
8.10
7.45
7.45
7.45
7.44
7.43
7.43
7.26 CDCl3
1.54 HDO
1.00
1.02
38000
36000
34000
32000
30000
28000
26000
24000
22000
20000
18000
16000
14000
12000
10000
8000
6000
4000
2000
0
-2000
f1 (ppm)

4,

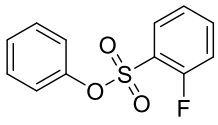

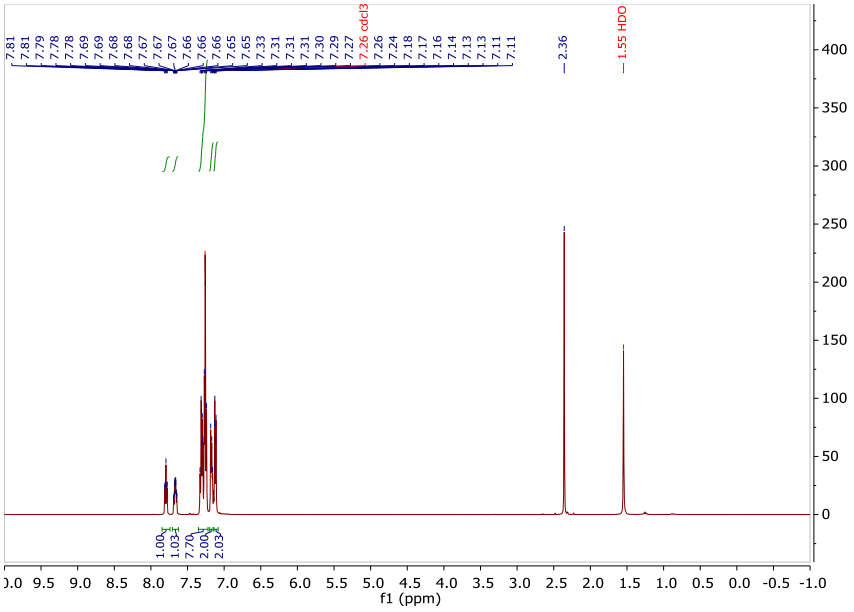
7.81
7.81
7.79
7.78
7.78
7.69
7.69
7.68
7.68
7.67
7.67
7.67
7.66
7.66
7.66
7.65
7.65
7.33
7.31
7.31
7.31
7.30
7.29
7.27
7.26 cdcl3
7.26
7.24
7.18
7.17
7.16
7.14
7.13
7.13
7.11
7.11
2.36
1.55 HDO
1.00
1.03
7.70
2.00
2.03
400
350
300
250
200
150
100
50
0
f1 (ppm)

5,

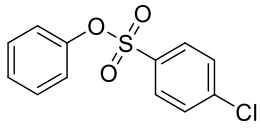
O
O
S
O
Cl

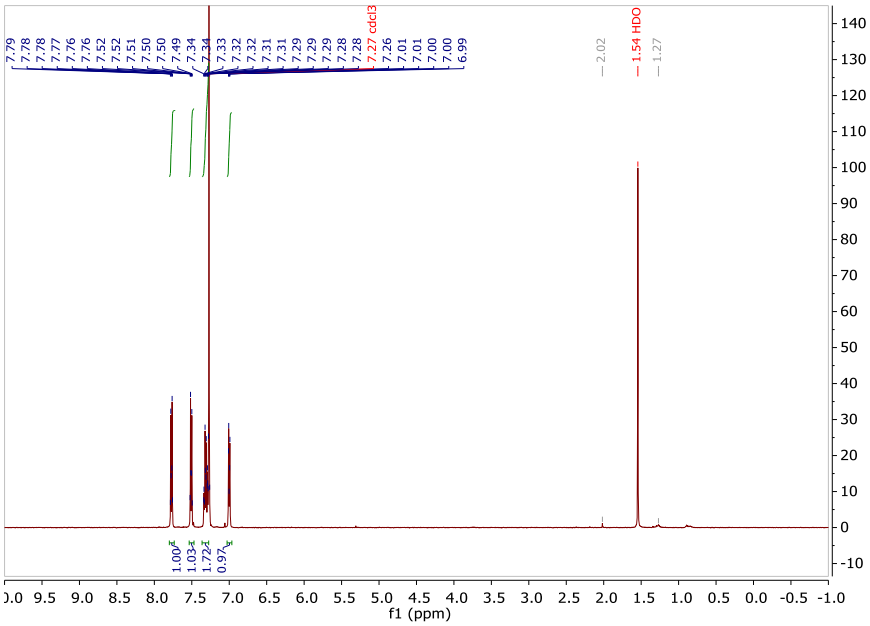
7.79
7.78
7.78
7.77
7.76
7.76
7.52
7.51
7.50
7.50
7.49
7.34
7.34
7.33
7.32
7.31
7.31
7.29
7.29
7.29
7.28
7.27 cdcl3
7.26
7.01
7.01
7.00
7.00
6.99
2.02
1.54 HDO
1.27
1.00
1.03
1.72
0.97
f1 (ppm)

6,

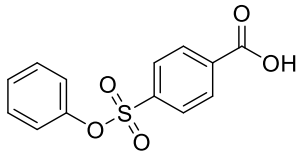
O
OH
O
S
O
O

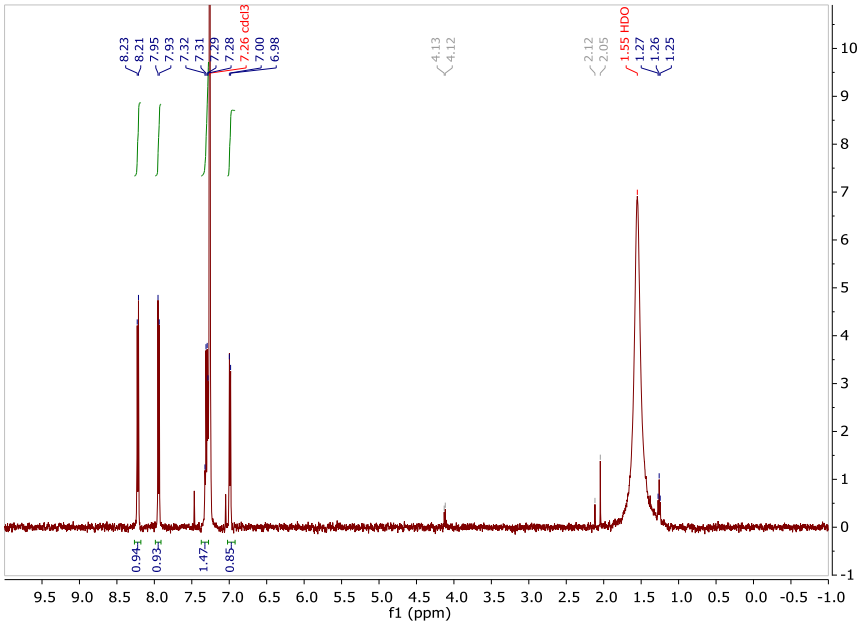
8.23
8.21
7.95
7.93
7.32
7.31
7.29
7.28
7.26 cdcl3
7.00
6.98
4.13
4.12
2.12
2.05
1.55 HDO
1.27
1.26
1.25
0.94
0.93
1.47
0.85
f1 (ppm)

7,

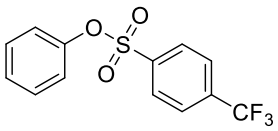

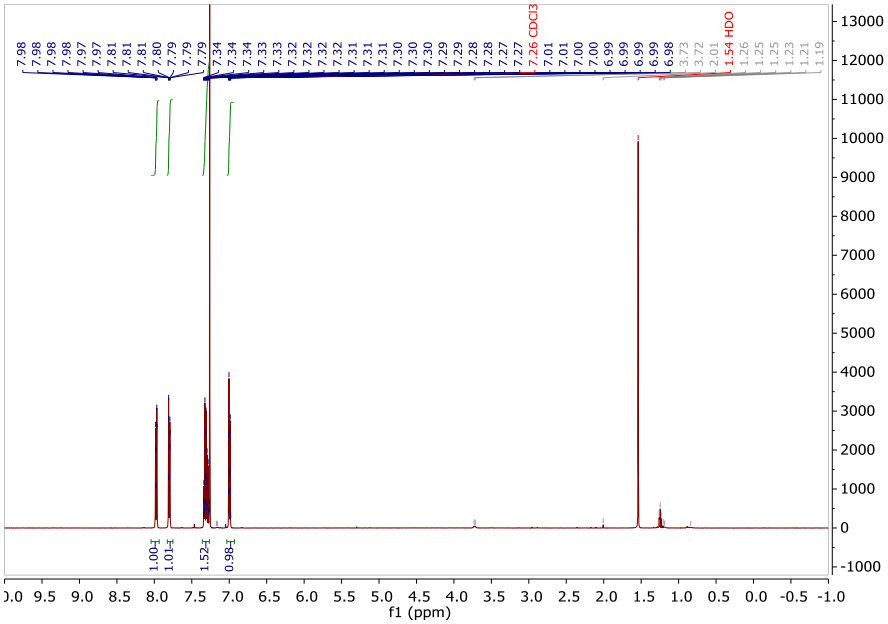
7.98 7.98 7.98 7.98 7.97 7.97 7.81 7.81 7.81 7.80 7.79 7.79 7.79 7.34 7.34 7.34 7.33 7.32 7.32 7.32 7.31 7.31 7.31 7.30 7.30 7.30 7.29 7.29 7.28 7.28 7.27 7.27 7.26 CDCl3 7.01 7.01 7.00 7.00 6.99 6.99 6.99 6.99 6.98 3.73 3.72 2.01 1.54 HDO 1.26 1.25 1.25 1.23 1.21 1.19
1.00 1.01 1.52 0.98
13000 12000 11000 10000 9000 8000 7000 6000 5000 4000 3000 2000 1000 0 -1000
9.5 9.0 8.5 8.0 7.5 7.0 6.5 6.0 5.5 5.0 4.5 4.0 3.5 3.0 2.5 2.0 1.5 1.0 0.5 0.0 -0.5 -1.0
f1 (ppm)

8,

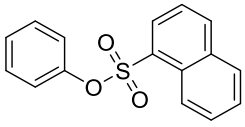

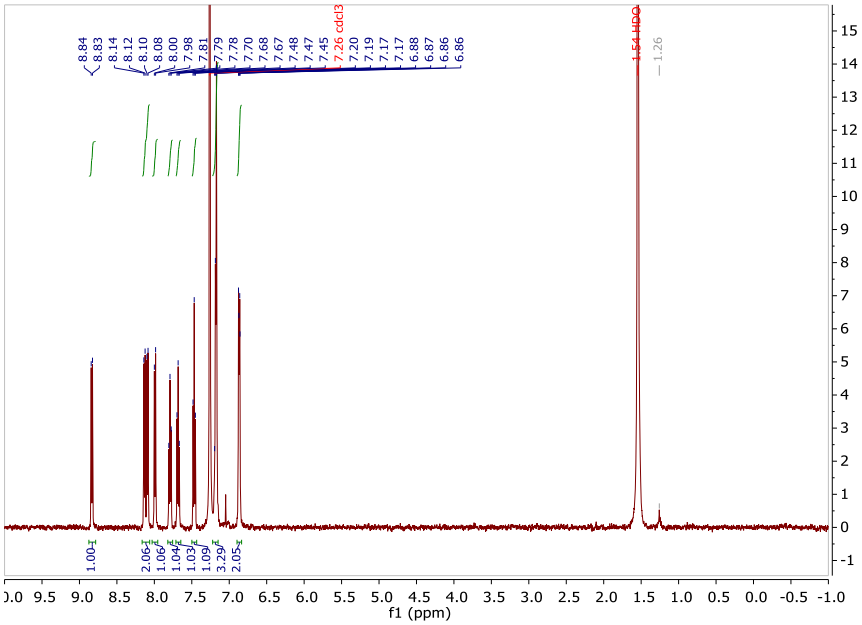
8.84 8.83 8.14 8.12 8.10 8.08 8.00 7.98 7.81 7.79 7.78 7.70 7.68 7.67 7.48 7.47 7.45 7.26 cdcl3 7.20 7.19 7.17 7.17 6.88 6.87 6.86 6.86 1.54 HDO 1.26
1.00 2.06 1.06 1.04 1.03 1.09 3.29 2.05
15 14 13 12 11 10 9 8 7 6 5 4 3 2 1 0 -1
9.5 9.0 8.5 8.0 7.5 7.0 6.5 6.0 5.5 5.0 4.5 4.0 3.5 3.0 2.5 2.0 1.5 1.0 0.5 0.0 -0.5 -1.0
f1 (ppm)

9,

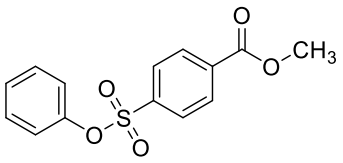

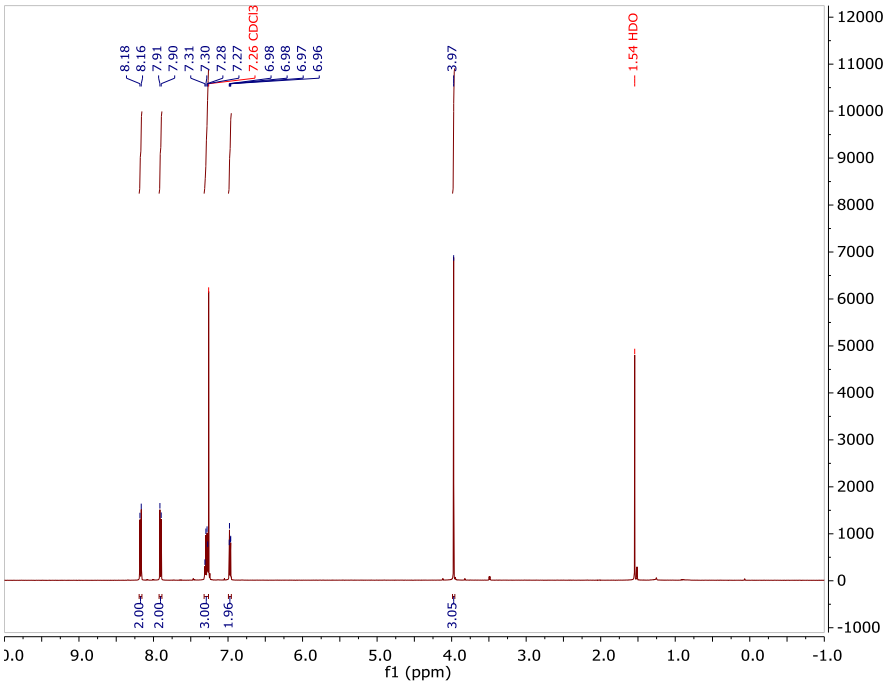
8.18
8.16
7.91
7.90
7.31
7.30
7.28
7.27
7.26 CDCl3
6.98
6.98
6.97
6.96
3.97
1.54 HDO
2.00
2.00
3.00
1.96
3.05
f1 (ppm)

10,

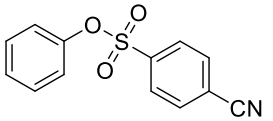

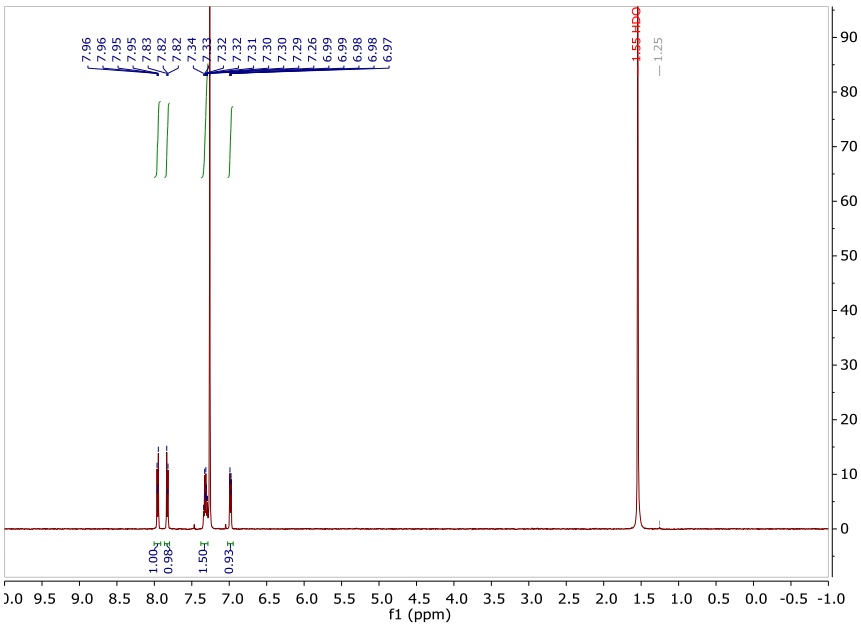
7.96
7.96
7.95
7.95
7.83
7.82
7.82
7.34
7.33
7.32
7.32
7.31
7.30
7.30
7.29
7.26
6.99
6.99
6.98
6.98
6.97
1.55 HDO
1.25
1.00
0.98
1.50
0.93
f1 (ppm)

11,

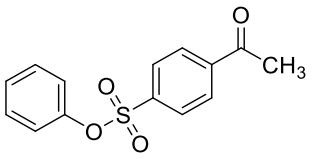

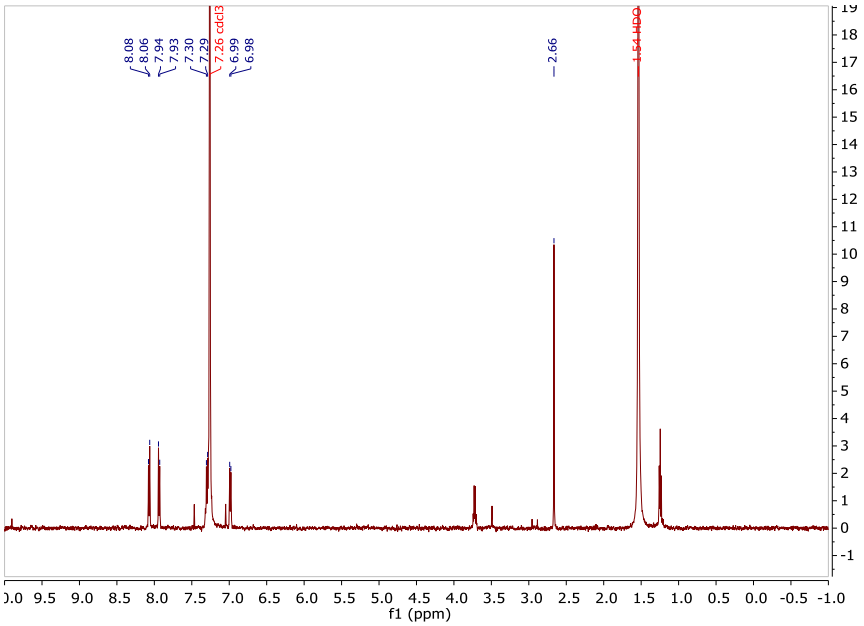
8.08
8.06
7.94
7.93
7.30
7.29
7.26 cdcl3
6.99
6.98
2.66
1.64 HDO
f1 (ppm)

12,

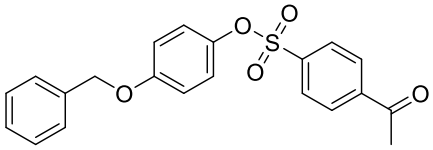

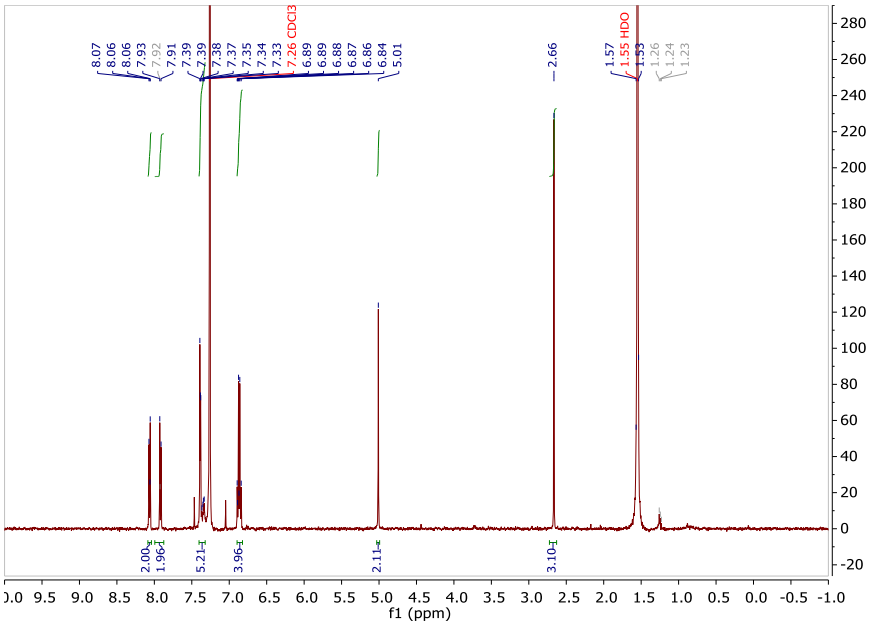
8.07
8.06
8.06
7.93
7.92
7.91
7.39
7.39
7.38
7.37
7.35
7.34
7.33
7.26 CDCl3
6.89
6.89
6.88
6.87
6.86
6.84
5.01
2.66
1.57
1.55 HDO
1.53
1.26
1.24
1.23
2.00
1.96
5.21
3.96
2.11
3.10
f1 (ppm)

13,

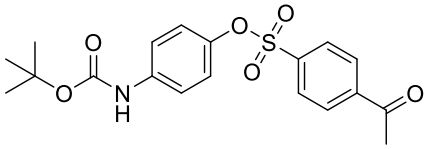

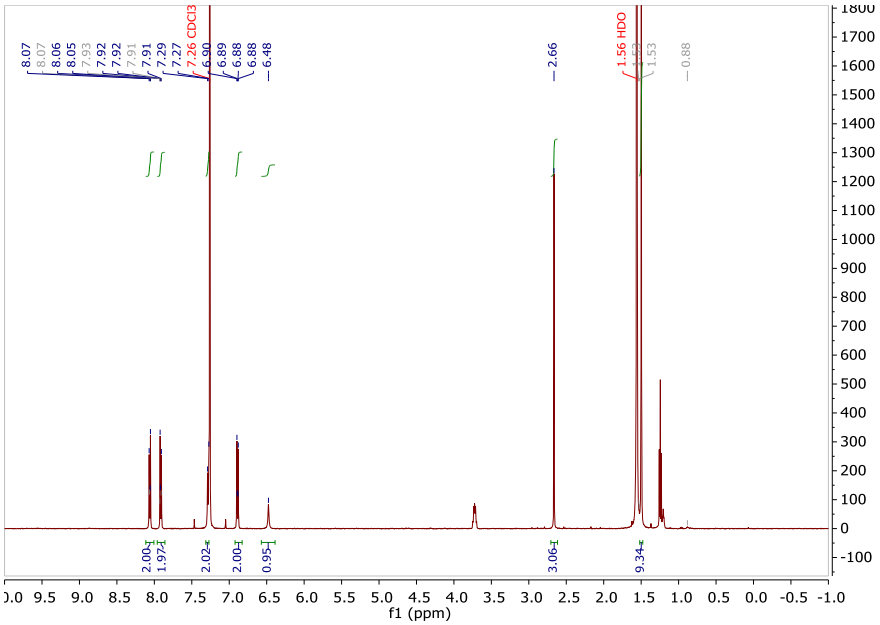
8.07
8.07
8.06
8.05
7.93
7.92
7.92
7.91
7.91
7.29
7.27
7.26 CDCl3
6.90
6.89
6.88
6.88
6.48
2.66
1.56 HDO
1.53
0.88
2.00
1.97
2.02
2.00
0.95
3.06
9.34
f1 (ppm)

14,

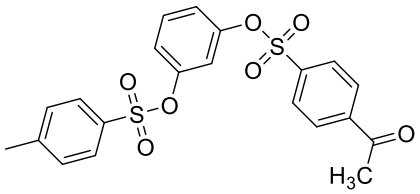

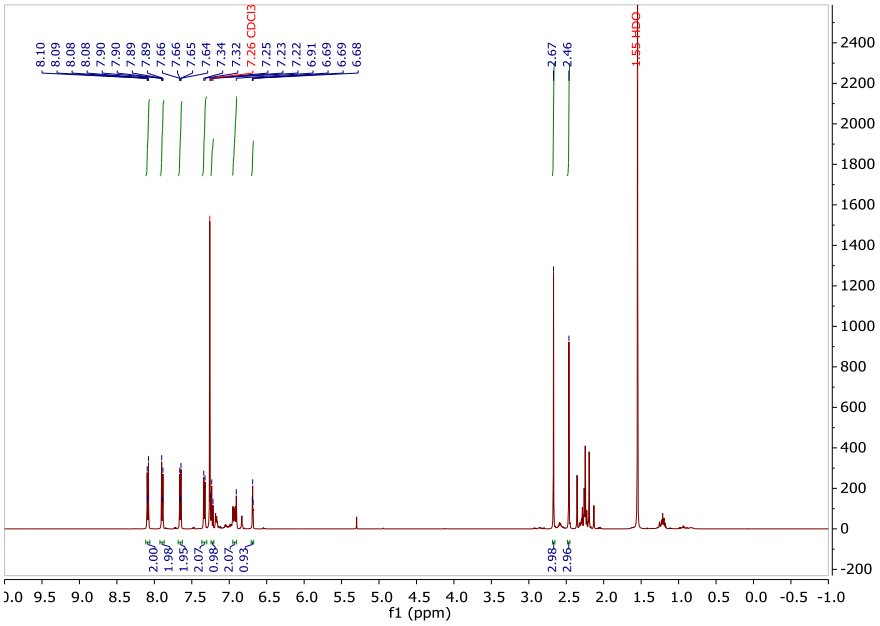
8.10
8.09
8.08
8.08
7.90
7.90
7.89
7.89
7.66
7.66
7.65
7.64
7.34
7.32
7.26 CDCl3
7.25
7.23
7.22
6.91
6.69
6.69
6.68
2.67
2.46
1.55 HDO
2.00
1.98
1.95
2.07
0.98
2.07
0.93
2.98
2.96
f1 (ppm)

15,

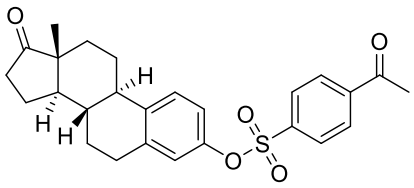

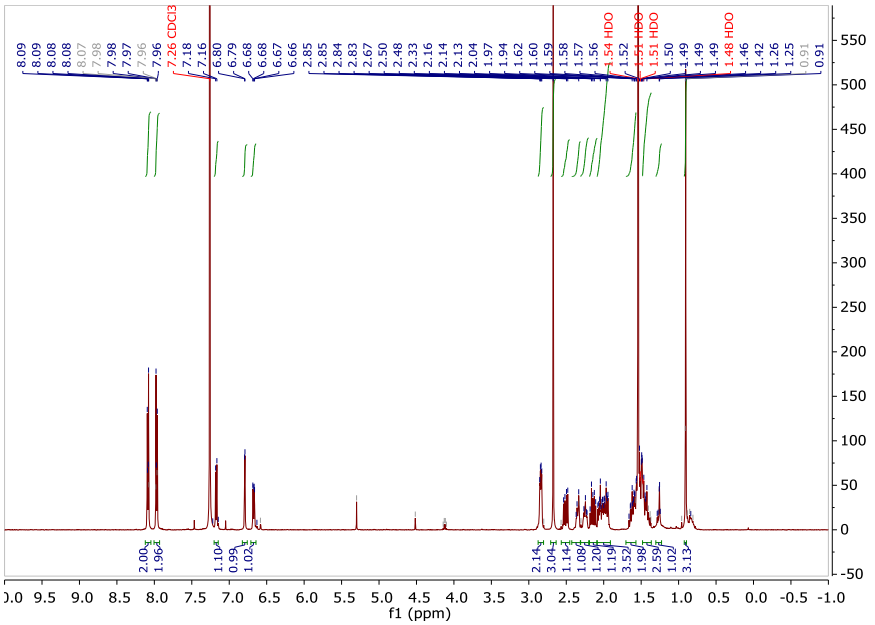

16,

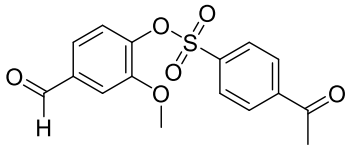

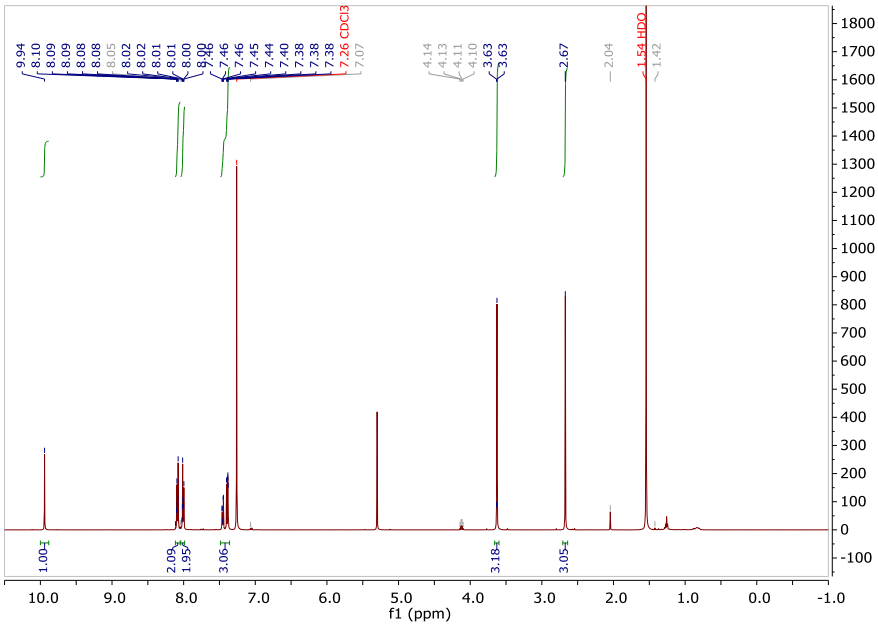

Chapter 4. Conclusions

4.1 Dissertation Summary

This dissertation describes the relationship between the surface chemistry of colloidal QDs and (1) their reactivity towards a molecular redox probe and (2) their catalytic efficiency for photoredox reactions.

In chapter 2, we identified the mechanisms by which fluorinated alkylthiolate ligands prevent photoinduced charge transfer between PbS QDs and a freely diffusing molecular photo-oxidant, duroquinone. The introduction of a small number (8-16 % of the total number of ligands on the surface of QDs) of dodecanethiolate ligands decreased the permeability of the ligands shell to duroquinone as a result of the strong thiolate-Pb bond. Upon increasing the number of fluorinated carbons from zero to ten, we observed a further decrease in the ligand shell permeability due to the steric bulk and oleophobicity of the fluorinated segments of the ligands. Through a combination of NMR, photoluminescence spectroscopy, transient absorption spectroscopy, and inductively coupled plasma optical emission spectroscopy, we observed that the surfaces of 1.4 nm and 1.5 nm QDs were more difficult to protect than 1.6 nm QDs because the ligand shells of the smaller QDs contain larger defects ($Pb(oleate)_2$ complexes) compared to the smaller oleic acid defects in the 1.6 nm QD's ligand shells. These defects in the ligand shell provide pathways for the duroquinone to interact with the inorganic core of the PbS QDs.

In chapter 3, we described the photoreductive deprotection of phenyl aryl sulfonates by visible-light absorbing $CuInS_2$. This approach is applicable to a range of substrates, including phenol protected with a variety of sulfonyl protecting groups, estrone, and molecules that contain other protecting groups. The QDs outperformed the state-of-the-art *fac*-$Ir(ppy)_3$ catalyst for the reductive deprotection of a molecule that contains a carboxylic acid moiety, a known QD-binding group,

due to the kinetic advantage of forming a metastable electron donor-acceptor complex between the QDs and substrate. This strategy of localizing a substrate on a photocatalyst to increase the rate of a reaction is a notable advantage of colloidal QDs in general, because their surface chemistry can be tuned independently of their electronic properties.

4.2 Future Directions and Outlook

4.2.1 *Investigation of the Effect of Ligand Shell Morphology on the Redox Activity of QDs*

As discussed in Chapters 1 & 2, charge transfer between quantum dots and molecular acceptors is strongly dependent on interactions between the molecular acceptor and the ligands on the surface of the QD. The morphology of the mixed-ligand shells (*e.g.* random, striped, patchy, Janus-like) is known to affect biological activity of nanoparticles and their wetting properties.[129-131]

On gold nanoparticles, mixed ligand layers of fluorinated and hydrogenated molecules form stripe-like domains, patches, and Janus domains, depending on the relative lengths of the ligand molecules and the presence or absence of branched alkyl chains.[36] NMR methods have been used to characterize the ligand shell morphology on gold nanoparticles, but they require the preparation of ligand shells with 0 to 100 % of fluorinated ligands.[35-36] While we demonstrated that the installation of fluorinated thiolate ligands onto the surface of QDs is a successful strategy for suppressing photoinduced charge transfer from PbS QDs to duroquinone, we were unable to characterize the morphology (*e.g.* phase segregation between the fluorinated ligands and oleate ligands) of the ligand shell due to the poor solubility of terminally fluorinated ligands. To circumvent the poor solubility of terminally fluorinated ligands, molecules with fluorinated sections proximate to the QD-binding group and terminally hydrogenated sections can be used. Various ligand shell morphologies should be attainable by using fluorinated and hydrogenated

ligands of different lengths.[36] Through a combination of NMR characterization and photoluminescence quenching experiments, the effect of the ligand shell morphology on the redox properties of QDs can be studied.

4.2.2 Increasing the Efficiency of the Photocatalytic Reduction of CO_2 via QDs with Fluorinated Ligands

As outlined in Chapter 2, the installation of fluorinated ligands onto the surface of PbS QDs decreased the redox activity of the QDs with a freely diffusing molecular acceptor. This decreased redox activity is a result of the steric bulk of the fluorinated ligands and the unfavorable intermolecular interactions between the molecular acceptor and the fluorinated ligands. Interestingly, fluorinated compounds are known to exhibit high solubility in supercritical CO_2, and to date, the only nanoparticles that have exhibited colloidal stability in supercritical CO_2 are capped with fluorinated ligands due to a higher CO_2-philicity of fluorocarbons compared to hydrocarbons.[132-134]

Although QDs have reduction potentials sufficient for CO_2 reduction,[58] they have not yet been implemented as solo-photocatalysts for the reduction of CO_2. Fluorinated ligands offer a unique route to increase the local concentration of CO_2 near the surface of QDs, which may be advantageous for increasing the photocatalytic efficiency of QDs for CO_2 reduction. We hypothesize that the catalytic efficiency of CO_2 reduction by QDs can be tuned by varying the degree of fluorination of the ligand shell of QDs.

4.2.3 Ligand-Assisted Substrate Localization through Reversible Covalent Bond Formation to Enhance Photocatalytic Performance of QDs

As we demonstrated in Chapter 3, localization of a substrate onto the surface of a QD can accelerate the rate of a redox reaction with QDs. One limitation of this strategy is that the binding affinity of a substrate with the surface of the QD must be low, such that it does not permanently bind to the surface and "poison" the catalyst.[48] A more versatile approach for localizing redox partners near the surface of QDs is to leverage advantageous interactions between the ligand shell of the QDs and redox partner; this has been achieved previously using electrostatic interactions and coordination bonds.[58, 135] Alternatively, the terminal functional groups of the ligands on the QD can form temporary covalent bonds with a substrate, *e.g.* thiolate ligands containing a 1,2-diol can form an acetal linkage with substrates containing ketones or aldehydes in mildly acidic conditions.[136] The QDs can then photo-reduce the localized substrate, and because the acetal bond is reversible in mildly acidic conditions, the reduced substrate can then desorb. We hypothesize the rate of reduction of the substrate by QDs with ligands with vicinal diols will be faster than QDs with ligands than cannot engage in acetal formation. Because this ligand-assisted substrate localization strategy does not require that a substrate contains a QD-binding group (*e.g.* a carboxylic acid), it is a more general and widely applicable approach.

References

1. Alivisatos, A. P., Semiconductor Clusters, Nanocrystals, and Quantum Dots. *Science* **1996,** *271*, 933-937.
2. Gao, Y.; Peng, X., Photogenerated Excitons in Plain Core Cdse Nanocrystals with Unity Radiative Decay in Single Channel: The Effects of Surface and Ligands. *J. Am. Chem. Soc.* **2015,** *137*, 4230-4235.
3. Song, W.-S.; Yang, H., Efficient White-Light-Emitting Diodes Fabricated from Highly Fluorescent Copper Indium Sulfide Core/Shell Quantum Dots. *Chem. Mater.* **2012,** *24*, 1961-1967.
4. Yu, W. W.; Qu, L.; Guo, W.; Peng, X., Experimental Determination of the Extinction Coefficient of CdTe, CdSe, and CdS Nanocrystals. *Chem. Mater.* **2003,** *15*, 2854-2860.
5. Shi, L.; De Paoli, V.; Rosenzweig, N.; Rosenzweig, Z., Synthesis and Application of Quantum Dots FRET-Based Protease Sensors. *J. Am. Chem. Soc.* **2006,** *128*, 10378-10379.
6. Frasco, M. F.; Chaniotakis, N., Semiconductor Quantum Dots in Chemical Sensors and Biosensors. *Sensors* **2009,** *9*, 7266-7286.
7. Kodaimati, M. S.; McClelland, K. P.; He, C.; Lian, S.; Jiang, Y.; Zhang, Z.; Weiss, E. A., Viewpoint: Challenges in Colloidal Photocatalysis and Some Strategies for Addressing Them. *Inorg. Chem.* **2018,** *57*, 3659-3670.
8. Nozik, A. J.; Beard, M. C.; Luther, J. M.; Law, M.; Ellingson, R. J.; Johnson, J. C., Semiconductor Quantum Dots and Quantum Dot Arrays and Applications of Multiple Exciton Generation to Third-Generation Photovoltaic Solar Cells. *Chem. Rev.* **2010,** *110*, 6873-6890.
9. Ning, Z.; Molnár, M.; Chen, Y.; Friberg, P.; Gan, L.; Ågren, H.; Fu, Y., Role of Surface Ligands in Optical Properties of Colloidal CdSe/CdS Quantum Dots. *Phys. Chem. Chem. Phys.* **2011,** *13*, 5848-5854.
10. Tan, S. J.; Jana, N. R.; Gao, S.; Patra, P. K.; Ying, J. Y., Surface-Ligand-Dependent Cellular Interaction, Subcellular Localization, and Cytotoxicity of Polymer-Coated Quantum Dots. *Chem. Mater.* **2010,** *22*, 2239-2247.
11. Kim, S.; Bawendi, M. G., Oligomeric Ligands for Luminescent and Stable Nanocrystal Quantum Dots. *J. Am. Chem. Soc.* **2003,** *125*, 14652-14653.
12. Fokina, A.; Klinker, K.; Braun, L.; Jeong, B. G.; Bae, W. K.; Barz, M.; Zentel, R., Multidentate Polysarcosine-Based Ligands for Water-Soluble Quantum Dots. *Macromolecules* **2016,** *49*, 3663-3671.
13. Dai, J.; Xi, J.; Li, L.; Zhao, J.; Shi, Y.; Zhang, W.; Ran, C.; Jiao, B.; Hou, X.; Duan, X., *et al.*, Charge Transport between Coupling Colloidal Perovskite Quantum Dots Assisted by Functional Conjugated Ligands. *Angew. Chem. Int. Ed.* **2018,** *57*, 5754-5758.
14. Laaksonen, T.; Pelliniemi, O.; Quinn, B. M., Ion Permeability of SAMs on Nanoparticle Surfaces. *J. Am. Chem. Soc.* **2006,** *128*, 14341-14346.
15. Love, J. C.; Estroff, L. A.; Kriebel, J. K.; Nuzzo, R. G.; Whitesides, G. M., Self-Assembled Monolayers of Thiolates on Metals as a Form of Nanotechnology. *Chem. Rev.* **2005,** *105*, 1103-1169.

16. Weeraman, C.; Yatawara, A. K.; Bordenyuk, A. N.; Benderskii, A. V., Effect of Nanoscale Geometry on Molecular Conformation: Vibrational Sum-Frequency Generation of Alkanethiols on Gold Nanoparticles. *J. Am. Chem. Soc.* **2006,** *128*, 14244-14245.
17. Bordenyuk, A. N.; Weeraman, C.; Yatawara, A.; Jayathilake, H. D.; Stiopkin, I.; Liu, Y.; Benderskii, A. V., Vibrational Sum Frequency Generation Spectroscopy of Dodecanethiol on Metal Nanoparticles. *J. Phys. Chem. C* **2007,** *111*, 8925-8933.
18. Moreels, I.; Justo, Y.; De Geyter, B.; Haustraete, K.; Martins, J. C.; Hens, Z., Size-Tunable, Bright, and Stable PbS Quantum Dots: A Surface Chemistry Study. *ACS Nano* **2011,** *5*, 2004-2012.
19. Choi, H.; Ko, J.-H.; Kim, Y.-H.; Jeong, S., Steric-Hindrance-Driven Shape Transition in PbS Quantum Dots: Understanding Size-Dependent Stability. *J. Am. Chem. Soc.* **2013,** *135*, 5278-5281.
20. Frederick, M. T.; Achtyl, J. L.; Knowles, K. E.; Weiss, E. A.; Geiger, F. M., Surface-Amplified Ligand Disorder in CdSe Quantum Dots Determined by Electron and Coherent Vibrational Spectroscopies. *J. Am. Chem. Soc.* **2011,** *133*, 7476-7481.
21. Cass, L. C.; Malicki, M.; Weiss, E. A., The Chemical Environments of Oleate Species within Samples of Oleate-Coated PbS Quantum Dots. *Anal. Chem.* **2013,** *85*, 6974-6979.
22. De Roo, J.; De Keukeleere, K.; Hens, Z.; Van Driessche, I., From Ligands to Binding Motifs and Beyond; the Enhanced Versatility of Nanocrystal Surfaces. *Dalton Trans.* **2016,** *45*, 13277-13283.
23. Hines, D. A.; Kamat, P. V., Quantum Dot Surface Chemistry: Ligand Effects and Electron Transfer Reactions. *J. Phys. Chem. C* **2013,** *117*, 14418-14426.
24. García-Rodríguez, R.; Liu, H., Mechanistic Insights into the Role of Alkylamine in the Synthesis of CdSe Nanocrystals. *J. Am. Chem. Soc.* **2014,** *136*, 1968-1975.
25. Yu, W. W.; Wang, Y. A.; Peng, X., Formation and Stability of Size-, Shape-, and Structure-Controlled CdTe Nanocrystals: Ligand Effects on Monomers and Nanocrystals. *Chem. Mater.* **2003,** *15*, 4300-4308.
26. Abargues, R.; Navarro, J.; Rodríguez-Cantó, P. J.; Maulu, A.; Sánchez-Royo, J. F.; Martínez-Pastor, J. P., Enhancing the Photocatalytic Properties of PbS QD Solids: The Ligand Exchange Approach. *Nanoscale* **2019,** *11*, 1978-1987.
27. Weinberg, D. J.; He, C.; Weiss, E. A., Control of the Redox Activity of Quantum Dots through Introduction of Fluoroalkanethiolates into Their Ligand Shells. *J. Am. Chem. Soc.* **2016,** *138*, 2319-2326.
28. Pong, B.-K.; Trout, B. L.; Lee, J.-Y., Modified Ligand-Exchange for Efficient Solubilization of CdSe/ZnS Quantum Dots in Water: A Procedure Guided by Computational Studies. *Langmuir* **2008,** *24*, 5270-5276.
29. Liu, L.; Guo, X.; Li, Y.; Zhong, X., Bifunctional Multidentate Ligand Modified Highly Stable Water-Soluble Quantum Dots. *Inorg. Chem.* **2010,** *49*, 3768-3775.
30. Zhang, Z.; Edme, K.; Lian, S.; Weiss, E. A., Enhancing the Rate of Quantum-Dot-Photocatalyzed Carbon–Carbon Coupling by Tuning the Composition of the Dot's Ligand Shell. *J. Am. Chem. Soc.* **2017**.
31. Moreels, I.; Martins, J. C.; Hens, Z., Solution Nmr Techniques for Investigating Colloidal Nanocrystal Ligands: A Case Study on Trioctylphosphine Oxide at InP Quantum Dots. *Sens. Actuators B Chem.* **2007,** *126*, 283-288.

32. Morris-Cohen, A. J.; Malicki, M.; Peterson, M. D.; Slavin, J. W. J.; Weiss, E. A., Chemical, Structural, and Quantitative Analysis of the Ligand Shells of Colloidal Quantum Dots. *Chem. Mater.* **2013,** *25*, 1155-1165.
33. Hens, Z.; Martins, J. C., A Solution NMR Toolbox for Characterizing the Surface Chemistry of Colloidal Nanocrystals. *Chem. Mater.* **2013,** *25*, 1211-1221.
34. Malicki, M.; Knowles, K. E.; Weiss, E. A., Gating of Hole Transfer from Photoexcited PbS Quantum Dots to Aminoferrocene by the Ligand Shell of the Dots. *ChemComm* **2013,** *49*, 4400-4402.
35. Marbella, L. E.; Millstone, J. E., NMR Techniques for Noble Metal Nanoparticles. *Chem. Mater.* **2015,** *27*, 2721-2739.
36. Şologan, M.; Cantarutti, C.; Bidoggia, S.; Polizzi, S.; Pengo, P.; Pasquato, L., Routes to the Preparation of Mixed Monolayers of Fluorinated and Hydrogenated Alkanethiolates Grafted on the Surface of Gold Nanoparticles. *Farad. Discuss.* **2016,** *191*, 527-543.
37. Knowles, K. E.; Malicki, M.; Weiss, E. A., Dual-Time Scale Photoinduced Electron Transfer from PbS Quantum Dots to a Molecular Acceptor. *J. Am. Chem. Soc.* **2012,** *134*, 12470-12473.
38. Aruda, K. O.; Bohlmann Kunz, M.; Tagliazucchi, M.; Weiss, E. A., Temperature-Dependent Permeability of the Ligand Shell of PbS Quantum Dots Probed by Electron Transfer to Benzoquinone. *J. Phys. Chem. Lett.* **2015,** *6*, 2841-2846.
39. Knowles, K. E.; Tagliazucchi, M.; Malicki, M.; Swenson, N. K.; Weiss, E. A., Electron Transfer as a Probe of the Permeability of Organic Monolayers on the Surfaces of Colloidal PbS Quantum Dots. *J. Phys. Chem. C* **2013,** *117*, 15849-15857.
40. Lakowicz, J. R., *Principles of Fluorescence Spectroscopy*. 3rd ed.; Springer: New York, 2006.
41. Rawalekar, S.; Kaniyankandy, S.; Verma, S.; Ghosh, H. N., Ultrafast Charge Carrier Relaxation and Charge Transfer Dynamics of CdTe/CdS Core−Shell Quantum Dots as Studied by Femtosecond Transient Absorption Spectroscopy. *J. Phys. Chem. C* **2010,** *114*, 1460-1466.
42. Wang, Y.-F.; Wang, H.-Y.; Li, Z.-S.; Zhao, J.; Wang, L.; Chen, Q.-D.; Wang, W.-Q.; Sun, H.-B., Electron Extraction Dynamics in CdSe and CdSe/CdS/ZnS Quantum Dots Adsorbed with Methyl Viologen. *J. Phys. Chem. C* **2014,** *118*, 17240-17246.
43. Harris, R. D.; Bettis Homan, S.; Kodaimati, M.; He, C.; Nepomnyashchii, A. B.; Swenson, N. K.; Lian, S.; Calzada, R.; Weiss, E. A., Electronic Processes within Quantum Dot-Molecule Complexes. *Chem. Rev.* **2016,** *116*, 12865-12919.
44. Yoon, T. P.; Ischay, M. A.; Du, J., Visible Light Photocatalysis as a Greener Approach to Photochemical Synthesis. *Nat. Chem.* **2010,** *2*, 527-532.
45. Prier, C. K.; Rankic, D. A.; MacMillan, D. W., Visible Light Photoredox Catalysis with Transition Metal Complexes: Applications in Organic Synthesis. *Chem. Rev.* **2013,** *113*, 5322-5363.
46. So, D.; Konstantatos, G., Thiol-Free Synthesized Copper Indium Sulfide Nanocrystals as Optoelectronic Quantum Dot Solids. *Chem. Mater.* **2015,** *27*, 8424-8432.
47. Flamee, S.; Cirillo, M.; Abe, S.; De Nolf, K.; Gomes, R.; Aubert, T.; Hens, Z., Fast, High Yield, and High Solid Loading Synthesis of Metal Selenide Nanocrystals. *Chem. Mater.* **2013,** *25*, 2476-2483.

48. Jensen, S. C.; Bettis Homan, S.; Weiss, E. A., Photocatalytic Conversion of Nitrobenzene to Aniline through Sequential Proton-Coupled One-Electron Transfers from a Cadmium Sulfide Quantum Dot. *J. Am. Chem. Soc.* **2016,** *138*, 1591-1600.
49. Lian, S.; Kodaimati, M. S.; Dolzhnikov, D. S.; Calzada, R.; Weiss, E. A., Powering a CO_2 Reduction Catalyst with Visible Light through Multiple Sub-Picosecond Electron Transfers from a Quantum Dot. *J. Am. Chem. Soc.* **2017,** *139*, 8931-8938.
50. Mongin, C.; Garakyaraghi, S.; Razgoniaeva, N.; Zamkov, M.; Castellano, F. N., Direct Observation of Triplet Energy Transfer from Semiconductor Nanocrystals. *Science* **2016,** *351*, 369-372.
51. Kuehnel, M. F.; Sahm, C. D.; Neri, G.; Lee, J. R.; Orchard, Katherine L.; Cowan, A. J.; Reisner, E., ZnSe Quantum Dots Modified with a Ni(Cyclam) Catalyst for Efficient Visible-Light Driven CO_2 Reduction in Water. *Chem. Sci.* **2018,** *9*, 2501-2509.
52. Lv, H.; Ruberu, T. P. A.; Fleischauer, V. E.; Brennessel, W. W.; Neidig, M. L.; Eisenberg, R., Catalytic Light-Driven Generation of Hydrogen from Water by Iron Dithiolene Complexes. *J. Am. Chem. Soc.* **2016,** *138*, 11654-11663.
53. Liu, C.; Qiu, F.; Peterson, J. J.; Krauss, T. D., Aqueous Photogeneration of H_2 with CdSe Nanocrystals and Nickel Catalysts: Electron Transfer Dynamics. *J. Phys. Chem. B* **2015,** *119*, 7349-7357.
54. Zhang, Z.; Rogers, C. R.; Weiss, E. A., Energy Transfer from CdS QDs to a Photogenerated Pd Complex Enhances the Rate and Selectivity of a Pd-Photocatalyzed Heck Reaction. *J. Am. Chem. Soc.* **2020,** *142*, 495-501.
55. Caputo, J. A.; Frenette, L. C.; Zhao, N.; Sowers, K. L.; Krauss, T. D.; Weix, D. J., General and Efficient C–C Bond Forming Photoredox Catalysis with Semiconductor Quantum Dots. *J. Am. Chem. Soc.* **2017**, *139*, 4250-4253.
56. McClelland, K. P.; Weiss, E. A., Selective Photocatalytic Oxidation of Benzyl Alcohol to Benzaldehyde or C–C Coupled Products by Visible-Light-Absorbing Quantum Dots. *ACS Appl. Energy Mater.* **2019,** *2*, 92-96.
57. Jiang, Y.; Wang, C.; Rogers, C. R.; Kodaimati, M. S.; Weiss, E. A., Regio- and Diastereoselective Intermolecular [2+2] Cycloadditions Photocatalysed by Quantum Dots. *Nat. Chem.* **2019,** *11*, 1034-1040.
58. Lian, S.; Kodaimati, M. S.; Weiss, E. A., Photocatalytically Active Superstructures of Quantum Dots and Iron Porphyrins for Reduction of CO_2 to CO in Water. *ACS Nano* **2018,** *12*, 568-575.
59. Kodaimati, M. S.; Lian, S.; Schatz, G. C.; Weiss, E. A., Energy Transfer-Enhanced Photocatalytic Reduction of Protons within Quantum Dot Light-Harvesting-Catalyst Assemblies. *Proc. Natl. Acad. Sci. U.S.A.* **2018,** *115*, 8290-8295.
60. Chen, Y.; Rosenzweig, Z., Luminescent CdS Quantum Dots as Selective Ion Probes. *Anal. Chem.* **2002,** *74*, 5132-5138.
61. Kim, S.-W.; Kim, S.; Tracy, J. B.; Jasanoff, A.; Bawendi, M. G., Phosphine Oxide Polymer for Water-Soluble Nanoparticles. *J. Am. Chem. Soc.* **2005,** *127*, 4556-4557.
62. Michalet, X.; Pinaud, F. F.; Bentolila, L. A.; Tsay, J. M.; Doose, S.; Li, J. J.; Sundaresan, G.; Wu, A. M.; Gambhir, S. S.; Weiss, S., Quantum Dots for Live Cells, in Vivo Imaging, and Diagnostics. *Science* **2005,** *307*, 538-544.

63. Fan, H.; Leve, E. W.; Scullin, C.; Gabaldon, J.; Tallant, D.; Bunge, S.; Boyle, T.; Wilson, M. C.; Brinker, C. J., Surfactant-Assisted Synthesis of Water-Soluble and Biocompatible Semiconductor Quantum Dot Micelles. *Nano Lett.* **2005,** *5*, 645-648.
64. Susumu, K.; Uyeda, H. T.; Medintz, I. L.; Pons, T.; Delehanty, J. B.; Mattoussi, H., Enhancing the Stability and Biological Functionalities of Quantum Dots Via Compact Multifunctional Ligands. *J. Am. Chem. Soc.* **2007,** *129*, 13987-13996.
65. Fenter, P.; Eberhardt, A.; Liang, K.; Eisenberger, P., Epitaxy and Chainlength Dependent Strain in Self-Assembled Monolayers. *J. Chem. Phys.* **1997,** *106*, 1600-1608.
66. Zenasni, O.; Jamison, A. C.; Lee, T. R., The Impact of Fluorination on the Structure and Properties of Self-Assembled Monolayer Films. *Soft Matter* **2013,** *9*, 6356-6370.
67. Green, M., The Nature of Quantum Dot Capping Ligands. *J. Mater. Chem.* **2010,** *20*, 5797-5809.
68. Ning, Z.; Voznyy, O.; Pan, J.; Hoogland, S.; Adinolfi, V.; Xu, J.; Li, M.; Kirmani, A. R.; Sun, J.-P.; Minor, J., *et al.*, Air-Stable N-Type Colloidal Quantum Dot Solids. *Nat. Mater.* **2014,** *13*, 822-828.
69. Kiani, A.; Alpuche-Aviles, M. A.; Eggers, P. K.; Jones, M.; Gooding, J. J.; Paddon-Row, M. N.; Bard, A. J., Scanning Electrochemical Microscopy. 59. Effect of Defects and Structure on Electron Transfer through Self-Assembled Monolayers. *Langmuir* **2008,** *24*, 2841-2849.
70. Zhou, H.; Wang, H.; Niu, H.; Gestos, A.; Wang, X.; Lin, T., Fluoroalkyl Silane Modified Silicone Rubber/Nanoparticle Composite: A Super Durable, Robust Superhydrophobic Fabric Coating. *Adv. Mater.* **2012,** *24*, 2409-2412.
71. Wang, H.; Fang, J.; Cheng, T.; Ding, J.; Qu, L.; Dai, L.; Wang, X.; Lin, T., One-Step Coating of Fluoro-Containing Silica Nanoparticles for Universal Generation of Surface Superhydrophobicity. *ChemComm* **2008**, 877-879.
72. Brassard, J.-D.; Sarkar, D. K.; Perron, J., Synthesis of Monodisperse Fluorinated Silica Nanoparticles and Their Superhydrophobic Thin Films. *ACS Appl. Mater. Interfaces* **2011,** *3*, 3583-3588.
73. Pengo, P.; Pasquato, L., Gold Nanoparticles Protected by Fluorinated Ligands: Syntheses, Properties and Applications. *J. Fluorine Chem.* **2015,** *177*, 2-10.
74. Kameo, A.; Yoshimura, T.; Esumi, K., Preparation of Noble Metal Nanoparticles in Supercritical Carbon Dioxide. *Colloids Surf. A* **2003,** *215*, 181-189.
75. Cao, Y.; Stavrinadis, A.; Lasanta, T.; So, D.; Konstantatos, G., The Role of Surface Passivation for Efficient and Photostable PbS Quantum Dot Solar Cells. *Nat. Energy* **2016,** *1*, 16035-16040.
76. Boles, M. A.; Ling, D.; Hyeon, T.; Talapin, D. V., The Surface Science of Nanocrystals. *Nat. Mater.* **2016,** *15*, 141-153.
77. Moreels, I.; Lambert, K.; Smeets, D.; De Muynck, D.; Nollet, T.; Martins, J. C.; Vanhaecke, F.; Vantomme, A.; Delerue, C.; Allan, G., *et al.*, Size-Dependent Optical Properties of Colloidal PbS Quantum Dots. *ACS Nano* **2009,** *3*, 3023-3030.
78. Naud, C.; Calas, P.; Blancou, H.; Commeyras, A., Synthesis of Terminally Perfluorinated Long-Chain Alkanethiols, Sulfides and Disulfides from the Corresponding Halides. *J. Fluorine Chem.* **2000,** *104*, 173-183.

79. Ji, X.; Copenhaver, D.; Sichmeller, C.; Peng, X., Ligand Bonding and Dynamics on Colloidal Nanocrystals at Room Temperature: The Case of Alkylamines on CdSe Nanocrystals. *J. Am. Chem. Soc.* **2008,** *130*, 5726-5735.
80. Sologan, M.; Marson, D.; Polizzi, S.; Pengo, P.; Boccardo, S.; Pricl, S.; Posocco, P.; Pasquato, L., Patchy and Janus Nanoparticles by Self-Organization of Mixtures of Fluorinated and Hydrogenated Alkanethiolates on the Surface of a Gold Core. *ACS Nano* **2016,** *10*, 9316-9325.
81. Bidoggia, S.; Milocco, F.; Polizzi, S.; Canton, P.; Saccani, A.; Sanavio, B.; Krol, S.; Stellacci, F.; Pengo, P.; Pasquato, L., Fluorinated and Charged Hydrogenated Alkanethiolates Grafted on Gold: Expanding the Diversity of Mixed-Monolayer Nanoparticles for Biological Applications. *Bioconjugate Chem.* **2017,** *28*, 43-52.
82. Tirotta, I.; Calloni, A.; Pigliacelli, C.; Brambilla, A.; Bussetti, G.; Duò, L.; Metrangolo, P.; Baldelli Bombelli, F., Chemical Characterization of Fluorinated/Hydrogenated Mixed Monolayers Grafted on Gold Nanoparticles. *J. Fluorine Chem.* **2018,** *206*, 99-107.
83. Harris, R. D.; Amin, V. A.; Lau, B.; Weiss, E. A., Role of Interligand Coupling in Determining the Interfacial Electronic Structure of Colloidal CdS Quantum Dots. *ACS Nano* **2016,** *10*, 1395-1403.
84. Knauf, R. R.; Lennox, J. C.; Dempsey, J. L., Quantifying Ligand Exchange Reactions at CdSe Nanocrystal Surfaces. *Chem. Mater.* **2016,** *28*, 4762-4770.
85. Fritzinger, B.; Capek, R. K.; Lambert, K.; Martins, J. C.; Hens, Z., Utilizing Self-Exchange to Address the Binding of Carboxylic Acid Ligands to CdSe Quantum Dots. *J. Am. Chem. Soc.* **2010,** *132*, 10195-10201.
86. Shen, Y.; Gee, M. Y.; Greytak, A. B., Purification Technologies for Colloidal Nanocrystals. *ChemComm* **2017,** *53*, 827-841.
87. Zherebetskyy, D.; Scheele, M.; Zhang, Y.; Bronstein, N.; Thompson, C.; Britt, D.; Salmeron, M.; Alivisatos, P.; Wang, L.-W., Hydroxylation of the Surface of PbS Nanocrystals Passivated with Oleic Acid. *Science* **2014,** *344*, 1380-1384.
88. Hassinen, A.; Moreels, I.; De Nolf, K.; Smet, P. F.; Martins, J. C.; Hens, Z., Short-Chain Alcohols Strip X-Type Ligands and Quench the Luminescence of PbSe and CdSe Quantum Dots, Acetonitrile Does Not. *J. Am. Chem. Soc.* **2012,** *134*, 20705-20712.
89. Malicki, M.; Knowles, K. E.; Weiss, E. A., Gating of Hole Transfer from Photoexcited PbS Quantum Dots to Aminoferrocene by the Ligand Shell of the Dots. *ChemComm* **2013,** *49*, 4400-4402.
90. Lee, H. J.; Jamison, A. C.; Lee, T. R., Surface Dipoles: A Growing Body of Evidence Supports Their Impact and Importance. *Acc. Chem. Res.* **2015,** *48*, 3007-3015.
91. Dunitz, J. D., Organic Fluorine: Odd Man Out. *ChemBioChem* **2004,** *5*, 614-621.
92. Colorado, R.; Lee, T. R., Physical Organic Probes of Interfacial Wettability Reveal the Importance of Surface Dipole Effects. *J. Phys. Org. Chem.* **2000,** *13*, 796-807.
93. Hines, M. A.; Scholes, G. D., Colloidal Pbs Nanocrystals with Size-Tunable near-Infrared Emission: Observation of Post-Synthesis Self-Narrowing of the Particle Size Distribution. *Adv. Mater.* **2003,** *15*, 1844-1849.
94. Schneider, C. A.; Rasband, W. S.; Eliceiri, K. W., Nih Image to ImageJ: 25 Years of Image Analysis. *Nat. Methods* **2012,** *9*, 671-675.

95. van Dam, H. J. J.; de Jong, W. A.; Bylaska, E.; Govind, N.; Kowalski, K.; Straatsma, T. P.; Valiev, M., Nwchem: Scalable Parallel Computational Chemistry. *Wiley Interdiscip. Rev. Comput. Mol. Sci* **2011,** *1*, 888-894.
96. York, D. M.; Karplus, M., A Smooth Solvation Potential Based on the Conductor-Like Screening Model. *J. Phys. Chem. A* **1999,** *103*, 11060-11079.
97. Momma, K.; Izumi, F., Vesta 3 for Three-Dimensional Visualization of Crystal, Volumetric and Morphology Data. *J. Appl. Crystallogr.* **2011,** *44*, 1272-1276.
98. Fowkes, F. M.; Riddle, F. L.; Pastore, W. E.; Weber, A. A., Interfacial Interactions between Self-Associated Polar Liquids and Squalane Used to Test Equations for Solid Liquid Interfacial Interactions. *Colloids Surf.* **1990,** *43*, 367-387.
99. Mairanovsky, V. G., Electro-Deprotection—Electrochemical Removal of Protecting Groups. *Angew. Chem. Int. Ed.* **1976,** *15*, 281-292.
100. Moussa, Z.; Romo, D., Mild Deprotection of Primary N-(P-Toluenesulfonyl) Amides with SmI_2 -Following Trifluoroacetylation. *Synlett* **2006**, 3294-3298.
101. Wuts, P. G. M.; Greene, T. W., Protection for Phenols and Catechols. *Greene's Protective Groups in Organic Synthesis*, 2006; 367-430.
102. Maia, H. L. S.; Medeiros, M. J.; Montenegro, M. I.; Court, D.; Pletcher, D., Deprotection by Electrolysis: Part I. The Application of Homogeneous Redox Catalysis to the Study of the Reduction of Tosyl Esters and Amides. *J. Electroanal. Chem.* **1984,** *164*, 347-361.
103. Ratushnyy, M.; Kamenova, M.; Gevorgyan, V., A Mild Light-Induced Cleavage of the S–O Bond of Aryl Sulfonate Esters Enables Efficient Sulfonylation of Vinylarenes. *Chem. Sci.* **2018,** *9*, 7193-7197.
104. Kageyama, Y.; Ohshima, R.; Sakurama, K.; Fujiwara, Y.; Tanimoto, Y.; Yamada, Y.; Aoki, S., Photochemical Cleavage Reactions of 8-Quinolinyl Sulfonates in Aqueous Solution. *Chem. Pharm. Bull.* **2009,** *57*, 1257-1266.
105. Falvey, D. E.; Sundararajan, C., Photoremovable Protecting Groups Based on Electron Transfer Chemistry. *Photochem. Photobiol. Sci.* **2004,** *3*, 831-838.
106. Hamada, T.; Nishida, A.; Yonemitsu, O., Selective Removal of Electron-Accepting p-Toluene- and Naphthalenesulfonyl Protecting Groups for Amino Function Via Photoinduced Donor Acceptor Ion Pairs with Electron-Donating Aromatics. *J. Am. Chem. Soc.* **1986,** *108*, 140-145.
107. Klán, P.; Šolomek, T.; Bochet, C. G.; Blanc, A.; Givens, R.; Rubina, M.; Popik, V.; Kostikov, A.; Wirz, J., Photoremovable Protecting Groups in Chemistry and Biology: Reaction Mechanisms and Efficacy. *Chem. Rev.* **2013,** *113*, 119-191.
108. Tucker, J. W.; Narayanam, J. M. R.; Shah, P. S.; Stephenson, C. R. J., Oxidative Photoredox Catalysis: Mild and Selective Deprotection of PMB Ethers Mediated by Visible Light. *ChemComm* **2011,** *47*, 5040-5042.
109. Iqbal, N.; Cho, E. J., Formation of Carbonyl Compounds from Amines through Oxidative C-N Bond Cleavage Using Visible Light Photocatalysis and Applications to N-PMB-Amide Deprotection. *Adv. Synth. Catal.* **2015,** *357*, 2187-2192.
110. Lechner, R.; König, B., Oxidation and Deprotection of Primary Benzylamines by Visible Light Flavin Photocatalysis. *Synthesis* **2010,** *10*, 1712-1718.

111. Liu, Q.; Liu, Z.; Zhou, Y.-L.; Zhang, W.; Yang, L.; Liu, Z.-L.; Yu, W., Photochemical Desulfonylation of N-Tosyl Amides by 2-Phenyl-N,N′--Dimethylbenzimidazoline (PDMBI). *Synlett* **2005,** *16*, 2510-2512.
112. Xuan, J.; Li, B.-J.; Feng, Z.-J.; Sun, G.-D.; Ma, H.-H.; Yuan, Z.-W.; Chen, J.-R.; Lu, L.-Q.; Xiao, W.-J., Desulfonylation of Tosyl Amides through Catalytic Photoredox Cleavage of N-S Bond under Visible-Light Irradiation. *Chem.: Asian J.* **2013,** *8*, 1090-1094.
113. Shaw, M. H.; Twilton, J.; MacMillan, D. W. C., Photoredox Catalysis in Organic Chemistry. *J. Org. Chem.* **2016,** *81*, 6898-6926.
114. Caputo, J. A.; Frenette, L. C.; Zhao, N.; Sowers, K. L.; Krauss, T. D.; Weix, D. J., General and Efficient C–C Bond Forming Photoredox Catalysis with Semiconductor Quantum Dots. *J. Am. Chem. Soc.* **2017,** *139*, 4250-4253.
115. Zhu, X.; Lin, Y.; Sun, Y.; Beard, M. C.; Yan, Y., Lead-Halide Perovskites for Photocatalytic α-Alkylation of Aldehydes. *J. Am. Chem. Soc.* **2019,** *141*, 733-738.
116. Li, L.; Pandey, A.; Werder, D. J.; Khanal, B. P.; Pietryga, J. M.; Klimov, V. I., Efficient Synthesis of Highly Luminescent Copper Indium Sulfide-Based Core/Shell Nanocrystals with Surprisingly Long-Lived Emission. *J. Am. Chem. Soc.* **2011,** *133*, 1176-1179.
117. Kolny-Olesiak, J.; Weller, H., Synthesis and Application of Colloidal $CuInS_2$ Semiconductor Nanocrystals. *ACS Appl. Mater. Interfaces* **2013,** *5*, 12221-12237.
118. Lei, X.; Jalla, A.; Abou Shama, M. A.; Stafford, J. M.; Cao, B., Chromatography-Free and Eco-Friendly Synthesis of Aryl Tosylates and Mesylates. *Synthesis* **2015,** *47*, 2578-2585.
119. Liu, C. L., James; Moslin, Ryan M.; Weinstein, David S.; Tokarski, John S. Imidazopyridazine Compounds Useful as Modulators of IL-12, IL-23 and/or IFN Alpha Responses. U.S. Patent 20180325899, June 18, 2015.
120. Sultane, P. R.; Mete, T. B.; Bhat, R. G., Chemoselective N-Deacetylation under Mild Conditions. *Org. Biomol. Chem.* **2014,** *12*, 261-264.
121. Joseph, J. T.; Sajith, A. M.; Ningegowda, R. C.; Nagaraj, A.; Rangappa, K. S.; Shashikanth, S., Aryl/Heteroaryl Pentafluorobenzenesulfonates (Aropfbs): New Electrophilic Coupling Partners for Room Temperature Suzuki–Miyaura Cross-Coupling Reactions. *Tetrahedron Lett.* **2015,** *56*, 5106-5111.
122. Lee, M.; Hong, J.; Lee, B.; Ku, K.; Lee, S.; Park, C. B.; Kang, K., Multi-Electron Redox Phenazine for Ready-to-Charge Organic Batteries. *Green Chem.* **2017,** *19*, 2980-2985.
123. King, K. A.; Spellane, P. J.; Watts, R. J., Excited-State Properties of a Triply Ortho-Metalated Iridium(III) Complex. *J. Am. Chem. Soc.* **1985,** *107*, 1431-1432.
124. Merrifield, R. B., Solid Phase Peptide Synthesis. I. The Synthesis of a Tetrapeptide. *J. Am. Chem. Soc.* **1963,** *85*, 2149-2154.
125. McClelland, K. P.; Clemons, T. D.; Stupp, S. I.; Weiss, E. A., Semiconductor Quantum Dots Are Efficient and Recyclable Photocatalysts for Aqueous PET-RAFT Polymerization. *ACS Macro Lett.* **2020,** *9*, 7-13.
126. Kim, C.-k.; Ghosh, P.; Rotello, V. M., Multimodal Drug Delivery Using Gold Nanoparticles. *Nanoscale* **2009,** *1*, 61-67.
127. DeLaive, P. J.; Foreman, T. K.; Giannotti, C.; Whitten, D. G., Photoinduced Electron Transfer Reactions of Transition-Metal Complexes with Amines. Mechanistic Studies of Alternate Pathways to Back Electron Transfer. *J. Am. Chem. Soc.* **1980,** *102*, 5627-5631.

128. Lee, C.; Field, L., Sulfinic Acids and Related Compounds 23. Preparation of Sulfinic Acids by the Reaction of Sulfonyl Halides with Thiols. *Synthesis* **1990,** *1990*, 391-397.
129. Kuna, J. J.; Voïtchovsky, K.; Singh, C.; Jiang, H.; Mwenifumbo, S.; Ghorai, P. K.; Stevens, M. M.; Glotzer, S. C.; Stellacci, F., The Effect of Nanometre-Scale Structure on Interfacial Energy. *Nat. Mater.* **2009,** *8*, 837-842.
130. Verma, A.; Uzun, O.; Hu, Y.; Hu, Y.; Han, H.-S.; Watson, N.; Chen, S.; Irvine, D. J.; Stellacci, F., Surface-Structure-Regulated Cell-Membrane Penetration by Monolayer-Protected Nanoparticles. *Nat. Mater.* **2008,** *7*, 588-595.
131. Hung, A.; Mwenifumbo, S.; Mager, M.; Kuna, J. J.; Stellacci, F.; Yarovsky, I.; Stevens, M. M., Ordering Surfaces on the Nanoscale: Implications for Protein Adsorption. *J. Am. Chem. Soc.* **2011,** *133*, 1438-1450.
132. Shah, P. S.; Holmes, J. D.; Doty, R. C.; Johnston, K. P.; Korgel, B. A., Steric Stabilization of Nanocrystals in Supercritical CO_2 Using Fluorinated Ligands. *J. Am. Chem. Soc.* **2000,** *122*, 4245-4246.
133. Raveendran, P.; Wallen, S. L., Exploring CO_2-Philicity: Effects of Stepwise Fluorination. *J. Phys. Chem. B* **2003,** *107*, 1473-1477.
134. Dalvi, V. H.; Srinivasan, V.; Rossky, P. J., Understanding the Effectiveness of Fluorocarbon Ligands in Dispersing Nanoparticles in Supercritical Carbon Dioxide. *J. Phys. Chem. C* **2010,** *114*, 15553-15561.
135. Jin, S.; Tagliazucchi, M.; Son, H.-J.; Harris, R. D.; Aruda, K. O.; Weinberg, D. J.; Nepomnyashchii, A. B.; Farha, O. K.; Hupp, J. T.; Weiss, E. A., Enhancement of the Yield of Photoinduced Charge Separation in Zinc Porphyrin–Quantum Dot Complexes by a Bis(dithiocarbamate) Linkage. *J. Phys. Chem. C* **2015,** *119*, 5195-5202.
136. Dong, J.-L.; Yu, L.-S.-H.; Xie, J.-W., A Simple and Versatile Method for the Formation of Acetals/Ketals Using Trace Conventional Acids. *ACS Omega* **2018,** *3*, 4974-4985.